Characterization of a home-built Low Temperature Scanning Probe Microscopy System

Inauguraldissertation

zur
Erlangung der Würde eines Doktors der Philosophie
vorgelegt der
Philosophisch-Naturwissenschaftlichen Fakultät
der Universität Basel

von

THAI Thanh Quang
aus Littau (LU), Schweiz

UNI
BASEL

Dübendorf, 2011

Genehmigt von der Philosophisch-Naturwissenschaftlichen Fakultät auf Antrag von:

Prof. Dr. H. J. Hug
Prof. Dr. E. Meyer

Basel, den 21. Juni 2011

Prof. Dr. M. Spiess, Dekan

**This work is dedicated to my parents, for their love,
endurance and sacrifices. To the rest of my family, for those who
survived but scattered all over the globe - many I encountered and
some others I will meet one day.**

**Ich widme diese Arbeit meinen Eltern für ihre Liebe, Ausdauer und erbrachten
Opfer. Die Widmung geht auch an meine restliche Familie, denjenigen die
überlebten und nun auf dem ganzen Globus verteilt sind - vielen bin ich begegnet
und weitere werde ich eines Tages kennenlernen.**

**Công việc này là dành riêng cho cha mẹ tôi, cho tình thương của họ, sức chịu đựng
và hy sinh. Để phần còn lại của gia đình tôi, cho những người sống sót nhưng nằm
rải rác trên toàn thế giới - nhiều người tôi gặp phải và một số những người khác
tôi sẽ đáp ứng được một ngày.**

Preface

The continuing advancement of technology is the driving force behind science and fundamental research. It does not stop with the invention of a device such as the wireless transmitter by Nikola Tesla [1] or the discovery of x-rays in the case of Roentgen [2]. Imagine a world without Marconi who did the first public radio broadcast [3]. The advancement of scientific instruments provides the foundation for new discoveries and amazing inventions. New phenomena may be explored, unlocked, and put to good use.

Usually, the scope of a PhD thesis revolves around a particular sample material, where different characterization tools and techniques can be applied to uncover a spectrum of data that defines its properties. The topic of this thesis however, is the characterization of a home-built *low temperature scanning probe microscopy* (LT-SPM) system, where the object of interest is the system itself. The outcome of the experiments are predetermined by the first blueprint, detailed design, construction and implementation of the system. Sample materials such as reconstructed Silicon (111)7x7 and *highly oriented pyrolytic graphite* (HOPG) were used to calibrate the LT-SPM, identify and solve all system related problems. All major experiments were performed with the LT-SPM prototype, whereas preliminary results were obtained with the *multi dimensional scanning probe microscopy* (MD-SPM) system. This work is outlined in the following way:

Chapter 1 gives a short historical review of nanoscience and *scanning probe microscopy* (SPM) technology with some applications. It compares various force sensors with each other, justifies the necessity of low temperature experimentation and briefs on how the LT-SPM system can meet the required conditions to achieve simultaneous nc-AFM/STM operations.

Chapter 2 conveys the basics of SPM, starting from the tunneling effect in STM and continuing with the concepts of force detection, interaction forces, dissipation, frequency shift in *non-contact atomic force microscopy*

(nc-AFM) and small oscillation amplitude operations.

Chapter 3 introduces the design and assembly of the LT-SPM and reveals the technical details of the system. The *ultra high vacuum* (UHV) chambers and their peripheral devices are described. With further explanations and illustrations of the actual microscope, the reader may get a glimpse into the complexity of the apparatus.

Chapter 4 explains the layout of the control electronics with a conceptional view of the hard- and software architecture. Along with the description of the FM detector, the noise characterization of the overall electronics is discussed.

Chapter 5 describes technical specifications of the *focusing Fabry Perot interferometer* (fFPi), where challenges such as temperature behavior and thermal noise limit are appointed. The calibration of the fFPi is essential and serves as a reference point for the issues discussed in chapter 8.

Chapter 6 reveals series of measurements on Si(111)7x7 and provides information regarding imaging performance of the system. Among these performance tests are atomically resolved scans at three different operating temperatures in *scanning tunneling microscopy* (STM) mode. In nc-AFM mode, imaging was performed with the cantilever driven at the fundamental and 2nd oscillation mode.

Chapter 7 presents the results of laser-induced effects on cantilevers and discusses the current knowledge. Furthermore, it analyzes the relation between cantilever cooling and the distorted amplitude readings of the fFPi, which may lead to misinterpretations of dissipation measurements.

Chapter 8 summarizes the findings in this work and gives the status of the LT-SFM. Instrumental improvements are indicated and perspectives for further works are outlined.

Keywords: low temperature home-built simultaneous STM/ nc-AFM, tip-sample gap stability, PLL and self-excitation, *highly oriented pyrolytic graphite* (HOPG), reconstructed Si(111)7x7, herringbone superstructure, focussing Fabry-Perot interferometer, cantilever cooling, radiation pressure and photothermal effects.

Contents

Part I

Prologue

Chapter 1

Introduction

Scanning probe instruments still have a major impact in nanoscience and technology, because they provide a link between the macroscopic world and the atomic scale. The key to a reliable performance of experiments at the nanometer scale is the instrumentation, that allows probe positioning ranging from micrometers to angstroms with sub atomic precisions.

Scanning probe microscopy (SPM) instruments have the unique capability to image single atoms in real space, resolve surface defects and observe sub surface features. Equipped with a conducting tip, a *scanning tunneling microscope* (STM) can be used to investigate conducting samples, semiconductors and atomically thin insulating films on conducting substrates [4, 5, 6]. Furthermore, sub atomic positioning is a requirement for *scanning tunneling spectroscopy* (STS), which probes the electronic structure on a sample surface at specific atomic sites [7, 8, 9].

Site specific vibrational spectroscopy offers basic understanding of the vibrational modes of atoms and molecules as well as their vibrational energies. Chemical identification of adsorbed molecules can be performed with this technique as suggested by Binnig et al [8]. Wilson Ho's group accomplished this goal as they distinguished two isotopes with vibrational microscopy images of inelastic tunneling channels [10]. Phenomena such as the quantum mechanical interference patterns on a Cu(111) surface probed with STM by Crommie et al gives us a glimpse at what is still to be discovered [11].

However, in STM not only electronic states are relevant, but forces also play an important role, which cause giant corrugations on graphite and other layered materials [12]. The most striking experiment involving forces is the manipulation of atoms and molecules, which was first demonstrated by Eigler and Schweizer, who moved single atoms by STM [13].

In order to investigate insulators at the atomic scale with spatial resolution comparable to STM and to directly measure interatomic forces, the *atomic* *force microscope* (AFM) was invented in 1986 [14]. The AFM provides the ability to study and image on conducting, semiconducting surfaces as well as on bulk insulators and biological materials. The AFM was first used with the tip in contact with the sample. Atomic resolution was obtained on different substrates [12, 15], but research groups realized soon that these "atomic resolution" images generally showed atomic scale periodicity [16, 17, 18]. Atomic scale features such as single adatoms, missing atoms or atomically sharp steps were not observed.

The first successful "true atomic resolution" efforts were obtained by Ohnesorge and Binnig, who used the AFM in polar aqueous environments to reduce the long range attractive Van der Waals force. This is to minimize the repulsive force between the tip apex and the surface to allow single atom tip-sample interactions [19]. In 1995, independent from each other, Kitamura et al [20] and Gissibl [21] reported the first "true atomic resolution" AFM images that finally featured single atoms and atomic defects on Silicon (111)7x7 in *ultra high vacuum* (UHV). They measured the resonance frequency shift caused by the interatomic forces acting between the tip apex and the surface, a technique that has become known as *non-contact AFM* (nc-AFM). The first site-specific interatomic forces on Silicon (111)7x7 were measured at low temperatures by Lantz et al [22, 23].

True atomic resolution AFM has been simplified with the use of tuning forks as force sensors, because a deflection sensor and its alignment to the cantilever is no longer needed. Further, the macroscopic size of the tuning fork easily allows the attachment of a metallic tip. Thus, every STM can be modified to an AFM. However, when compared with micro-fabricated cantilevers, these sensors are stiff[1] and have a relatively low quality factor, which limits their sensitivity for small forces, e.g. mapping magnetic forces in *magnetic force microscopy* (MFM). Atomic resolution imaging is possible with excellent signal to noise ratio because interatomic force gradients are relatively large ($> 1\,\mathrm{N/m}$) and decay within a few angstroms, matching typically used tuning fork oscillation amplitudes [24]. The high spring constant of tuning fork sensors is advantageous for small amplitude operations. This is because the high stiffness prevents the tip snapping into the surface and the energy stored in the oscillation is large compared to the typical energy loss per oscillation cycle cause by inelastic tip-sample forces ($\approx$ 0.1eV) [25]. Nevertheless, small amplitude operation is possible with small mass sensor such as micro-fabricated cantilevers, provided that certain stability conditions are met. One specific integration is the use of higher cantilever oscillation modes with conventional cantilevers having a

---

[1] k≈2000 N/m

standard stiffness of 40 N/m [26] (see section 6.4.2). Alternatives are the use of cantilevers with very high spring constants in the order of 500 N/m and higher. Another approach is to drive the cantilever off-resonance and map the force-induced changes in the oscillation amplitude and phase [27].

In this thesis, a new type of SFM system operating in UHV and at *liquid Helium* (LHe) temperature was developed. This offers the advantages that even reactive surfaces remain clean over time periods of several days, permitting long time experiments. Moreover, these experiments gain advantages from the low drift and creep rates obtained at low temperature. Also at low temperature the intrinsic noise of the cantilever is reduced, resulting in a smaller minimum measurable force [28],

$$F_{min} = \sqrt{S_F B} = \sqrt{\frac{4k_B T k B}{\omega_0 Q}} \qquad \left[\frac{\mathrm{N}}{\sqrt{\mathrm{Hz}}}\right] \tag{1.0.1}$$

with $S_F = 4\Gamma k_B T$, where k_B is the Boltzmann constant, T the temperature, B the measurement bandwidth, k the cantilever force constant, $f_0 = \omega_0/2\pi$ is the cantilever resonance frequency and the intrinsic quality factor Q of the cantilever. The latter is related to Γ as

$$\Gamma = \frac{k}{\omega_0 Q} \qquad \left[\frac{\mathrm{kg}}{\mathrm{s}}\right] \tag{1.0.2}$$

and to the velocity dependent dissipation term in the harmonic oscillation equation

$$m\frac{d^2x}{dt^2} + \Gamma\frac{dx}{dt} + kx = F_{signal}(t) + F_{noise}(t) \tag{1.0.3}$$

From the equation 1.0.1, the minimum measurable force derivative becomes (force gradient),

$$\frac{dF_{min}}{dz} = \frac{1}{A}\sqrt{\frac{4k_B T k B}{\omega_0 Q}} \tag{1.0.4}$$

where A is the oscillation amplitude of the cantilever. In addition, the minimum detectable tip-sample force induces an energy loss per oscillation cycle $\Delta\Gamma_{min}$ of:

$$\Delta\Gamma_{min} = \frac{F_{min}}{\omega_0 A} \qquad \left[\frac{\mathrm{kg}}{\mathrm{s}}\right] \tag{1.0.5}$$

Note that equation 1.0.4 states that the minimum measurable force gradients improve with larger oscillation amplitude A. This does not necessarily lead to a better signal to noise ratio, because the cantilever tip does not remain in the force field of the sample if the oscillation amplitude is larger than the decay length of the force.

Table 1.1 compares the values for the minimum measurable force F_{min}, force gradient ΔF_{min}, frequency shift Δf, energy stored in the oscillating cantilever $\Delta\Gamma_{min}$ and thermal noise amplitude $A_{thermal}$ for different temperatures and different types of cantilevers. Cantilevers highlighted by letters in the *italics* format are extrapolations based on values obtained experimentally under different conditions[2].

The values k, f_0 and Q highlighted by the **bold lined box** are the mechanical properties of the cantilevers. With the operation temperature T given in the next column, F_{min} can be calculated from equation 1.0.1. A temperature (4.2K or 300K) was selected for all cantilevers dependent on the temperature used in the actual experiments[3]. The amplitude A is used to calculate the $\frac{\partial F_{min}}{\partial z}$, Δf_{min} and Γ_{min}. A is selected to represent the oscillation amplitude typically used in experiments with such cantilevers. From this table the following conclusions can be drawn:

1. The best force sensitivity is obtained (1, 2 from table 1.1) for ultrasoft, high quality factor, ultrathin single crystalline silicon cantilevers. Such cantilevers are however too soft for conventional AFM imaging. They are typically used in a vertical arrangement [29] to detect ultrasmall forces down to the attonewton range and study different tip-sample induced dissipation mechanisms [28].

2. Soft cantilevers, typically used for MFM (3 from table 1.1), provide a reasonably good force sensitivity that is about two orders of magnitude lower than that of conventional cantilevers. An improved force sensitivity can be obtained with ultrasmall cantilevers (4, 5 from table 1.1).

3. Tuning forks, especially when used in the $Q-plus$ setup [30], have a high stiffness k, a relatively low resonance frequency f_0 and low quality factor Q (6, 7 from table 1.1). This limits the sensitivity for small forces. Compared to a cantilever used for MFM, the force sensitivity of tuning forks is about one order of magnitude smaller. But because of the low oscillating amplitude commonly used for tuning forks, they provide sufficient $\frac{\partial F_{min}}{\partial z}$ sensitivity to measure atomic forces. Furthermore, the energy stored in the tuning fork oscillating at 0.1nm amplitude is much larger than the typical energy loss per oscillating cycle induced by atomic scale tip-sample interactions.

---

[2] Temperatures, before a hypothetical heat treatment to increase Q

[3] Cantilevers description in the first column

4. Hard cantilevers with a spring constant of 30-500 N/m are typically used in nc-AFM with 5nm amplitude (8, 9, 10, 11 from table 1.1). Their force sensitivity F_{min} is up to two orders of magnitude better than that of tuning forks. But these cantilevers must be operated at amplitudes of a few nanometers so that sufficient energy is stored in their oscillation. The excellent force sensitivity however has to be compared to the smaller signal generated, because the amplitude is considerably larger than the interatomic force decay length. Taking into account the smaller signal, the signal to noise ratio of tuning forks becomes comparable.

5. Micro-fabricated cantilevers were successfully used in higher oscillating modes (12, 13 from table 1.1). The effective stiffness is comparable to tuning forks, but has the advantage that the quality factor Q remains high. The very high resonance frequency f_0 compared to f_0 of tuning forks, leads to excellent force sensitivity. Higher energy stored in each oscillating cycle means that measurements with smaller cantilever oscillating amplitude are possible.

According to table 1.1, cantilevers with 20-2000 N/m are ideal for this purpose. However, at 4.2K a cantilever with stiffness of 100 N/m has a thermal noise of

$$A = \sqrt{\frac{2k_BT}{k}} = \sqrt{\frac{2 \times 1.38 \times 10^{-23}(\mathrm{J/K}) \times 4.2K}{100\mathrm{N/m}}} = 1.08 \times 10^{-12}\,\mathrm{m}$$

From the thermodynamical limits for the sensitivities (see equation 1.0.1) the noise can only be reduced if all other noise sources such as that of the deflection detector, tip-sample gap and electronics are sufficiently small. For the deflection detector, this implies that its noise in a typical measurement bandwidth of $B = 1000Hz$ should be less than,

$$\frac{A}{10\sqrt{B}} = \frac{1.08 \times 10^{-12}\mathrm{m}}{10\sqrt{1000\mathrm{Hz}}} = 10.1\left[\frac{\mathrm{fm}}{\sqrt{\mathrm{Hz}}}\right]$$

Fukuma et al have shown that the deflection sensitivity and bandwidth of beam deflection systems are comparable to interferometric detection schemes [31]. Furthermore, beam deflection systems are also suitable for small amplitude operations under ambient conditions [32]. However, its implementation to low temperature environments still remains unpractical due to space restriction and adjustment accessibility.

The approach with this *low temperature scanning probe microscopy* (LT-SPM) system is the implementation of a *focussing Fabry Perot interferometer* (fFPi) that includes the following features:

- **Noise requirements for a deflection detector:** Small amplitude operations and stiff cantilevers require sensors with a high deflection sensitivity. With the fFPi in this LT-SPM system, a deflection sensitivity of $\leq 4\text{fm}/\sqrt{\text{Hz}}$ at 1MHz can be obtained (see chapter 5).
- **Bandwidth:** Wide detection bandwidth (DC-10MHz) enables the operation of higher flexural oscillation modes as well as the torsional modes of the cantilever. The bandwidth is expandable to several GHz with appropriate photodetector.
- **Small spot and positioning:** A laser spot size of 3μm enables the use of ultra small cantilevers with the dimensions 1/10 of conventional cantilevers. Moreover, mapping the backside of a cantilever provides an accurate spot positioning behind the cantilever's tip, which allows exact amplitude measurements. Torsional mode operations can be achieved by moving the laser spot slightly off center.
- **Photothermal excitation:** Excitation of the cantilever with piezo actuators introduces undesirable mechanical vibrations near the cantilever resonance frequency. To ensure that only the cantilever itself oscillates, optical excitation was first demonstrated by Umeda et al [33]. Future upgrades of the LT-SPM system will enable the photothermal excitation of cantilevers with one optical lens system that accommodates two lasers. One laser excites the cantilever and the other is used for the detection (see section 5.3).
- **Multidirectionality:** Simultaneous flexural and torsional force detection enables quantitative studies of frictions and thus, atom manipulations by AFM. This multidirectional force detection cannot be achieved with tuning forks, whereas a beam deflection system simultaneously records vertical and lateral forces. The fFPi allows the multidirectional force detection at low temperatures, where the forces in different spatial directions can be simultaneously measured and separated in the frequency space.
- **Simultaneous nc-AFM/STM:** Simultaneous imaging with a *low temperature scanning tunneling microscope/ atomic force microscope* (LT-STM/AFM) can be performed with a conductive cantilever. The combination of both types of microscopes provides more information

> than an STM or AFM alone. Atomically precise force and energy related information inaccessible in regular STM imaging, offers a detailed picture of tip-sample interactions during tunneling. Therefore, force and energy dissipation data may be obtained, which are critical for accurate analysis of atomic and molecular scale manipulations, diffusion studies and investigations of bond formation. In addition, recording tunnel currents while imaging with an AFM provides invaluable complimentary data to force mapping. Bias dependent simultaneous nc-AFM/STM, and site specific work function maps may exhibit a clearer picture of the forces and their origin.

The aim of this PhD thesis is the development, implementation and characterization of a new low temperature scanning probe microscope with an ultra sensitive and high bandwidth fFPi deflection sensor, suitable for nc-AFM operations with small, simultaneous flexural and torsional cantilever oscillation modes. Furthermore, expected upgrades will allow simultaneous nc-AFM/STM operations.

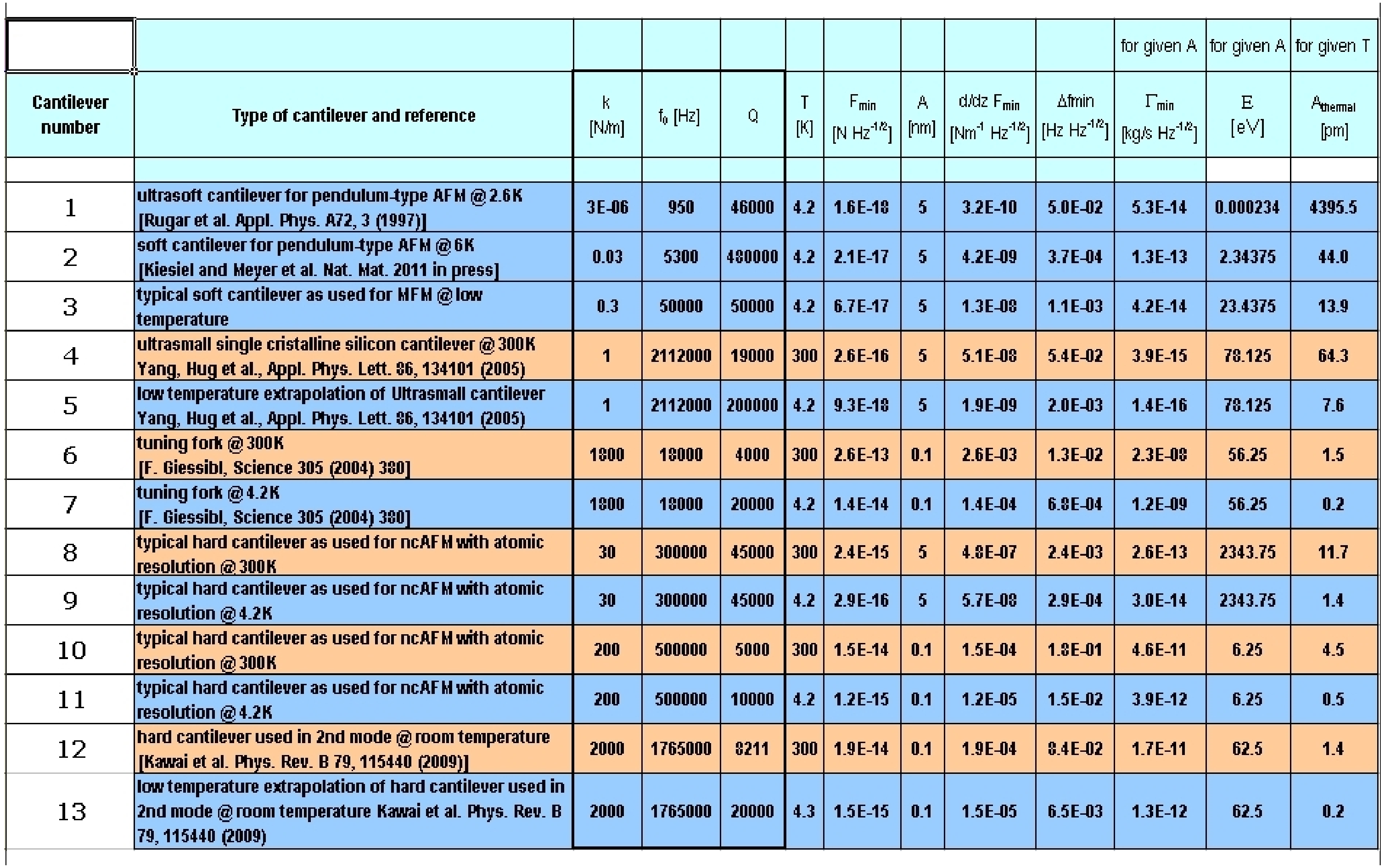

										for given A	for given A	for given T
Cantilever number	**Type of cantilever and reference**	k [N/m]	f_0 [Hz]	Q	T [K]	F_{min} [N Hz$^{-1/2}$]	A [nm]	d/dz F_{min} [Nm^{-1} Hz$^{-1/2}$]	Δfmin [Hz Hz$^{-1/2}$]	Γ_{min} [kg/s Hz$^{-1/2}$]	E [eV]	$A_{thermal}$ [pm]
1	**ultrasoft cantilever for pendulum-type AFM @ 2.6K [Rugar et al. Appl. Phys. A72, 3 (1997)]**	**3E-06**	**950**	**46000**	**4.2**	**1.6E-18**	**5**	**3.2E-10**	**5.0E-02**	**5.3E-14**	**0.000234**	**4395.5**
2	**soft cantilever for pendulum-type AFM @ 6K [Kiesiel and Meyer et al. Nat. Mat. 2011 in press]**	**0.03**	**5300**	**480000**	**4.2**	**2.1E-17**	**5**	**4.2E-09**	**3.7E-04**	**1.3E-13**	**2.34375**	**44.0**
3	**typical soft cantilever as used for MFM @ low temperature**	**0.3**	**50000**	**50000**	**4.2**	**6.7E-17**	**5**	**1.3E-08**	**1.1E-03**	**4.2E-14**	**23.4375**	**13.9**
4	**ultrasmall single cristalline silicon cantilever @ 300K Yang, Hug et al., Appl. Phys. Lett. 86, 134101 (2005)**	**1**	**2112000**	**19000**	**300**	**2.6E-16**	**5**	**5.1E-08**	**5.4E-02**	**3.9E-15**	**78.125**	**64.3**
5	**low temperature extrapolation of Ultrasmall cantilever Yang, Hug et al., Appl. Phys. Lett. 86, 134101 (2005)**	**1**	**2112000**	**200000**	**4.2**	**9.3E-18**	**5**	**1.9E-09**	**2.0E-03**	**1.4E-16**	**78.125**	**7.6**
6	**tuning fork @ 300K [F. Giessibl, Science 305 (2004) 380]**	**1800**	**18000**	**4000**	**300**	**2.6E-13**	**0.1**	**2.6E-03**	**1.3E-02**	**2.3E-08**	**56.25**	**1.5**
7	**tuning fork @ 4.2K [F. Giessibl, Science 305 (2004) 380]**	**1800**	**18000**	**20000**	**4.2**	**1.4E-14**	**0.1**	**1.4E-04**	**6.8E-04**	**1.2E-09**	**56.25**	**0.2**
8	**typical hard cantilever as used for ncAFM with atomic resolution @ 300K**	**30**	**300000**	**45000**	**300**	**2.4E-15**	**5**	**4.8E-07**	**2.4E-03**	**2.6E-13**	**2343.75**	**11.7**
9	**typical hard cantilever as used for ncAFM with atomic resolution @ 4.2K**	**30**	**300000**	**45000**	**4.2**	**2.9E-16**	**5**	**5.7E-08**	**2.9E-04**	**3.0E-14**	**2343.75**	**1.4**
10	**typical hard cantilever as used for ncAFM with atomic resolution @ 300K**	**200**	**500000**	**5000**	**300**	**1.5E-14**	**0.1**	**1.5E-04**	**1.8E-01**	**4.6E-11**	**6.25**	**4.5**
11	**typical hard cantilever as used for ncAFM with atomic resolution @ 4.2K**	**200**	**500000**	**10000**	**4.2**	**1.2E-15**	**0.1**	**1.2E-05**	**1.5E-02**	**3.9E-12**	**6.25**	**0.5**
12	**hard cantilever used in 2nd mode @ room temperature [Kawai et al. Phys. Rev. B 79, 115440 (2009)]**	**2000**	**1765000**	**8211**	**300**	**1.9E-14**	**0.1**	**1.9E-04**	**8.4E-02**	**1.7E-11**	**62.5**	**1.4**
13	**low temperature extrapolation of hard cantilever used in 2nd mode @ room temperature Kawai et al. Phys. Rev. B 79, 115440 (2009)**	**2000**	**1765000**	**20000**	**4.3**	**1.5E-15**	**0.1**	**1.5E-05**	**6.5E-03**	**1.3E-12**	**62.5**	**0.2**

Table 1.1: Different cantilever types and sensitivities are listed with the corresponding reference.

Chapter 2

Introduction of Scanning Probe Microscopy

The vast expansion in nanoscience research did not take off until the early 1980's, with the invention and development of the *scanning tunneling microscope* (STM)[1] [34]. Imaging atoms had been possible since the 1950's with the *field ion microscope* (FIM), when Erwin Wilhelm Müller published images of atomic structures of a tungsten tip [35, 36, 37]. The big leap forward for the science community was not the visualization, but rather the capability of STM to interact with the individual atom on the surface. STM also enables imaging on flat and conducting surfaces, as well as on semiconductors. The tunneling of electrons between a metallic tip and a conducting sample provides an image that represents the local electronic structure of surface atoms. Furthermore, a force exists between the surface and the apex atom of the probing tip that could be detected [12]. This effect gave rise to a new development in scanning probe microscopy. Gerd Binnig, Calvin Quate, and Christopher Gerber published their first *atomic force microscope* (AFM) results in 1986 [14].

2.1 Scanning Tunneling Microscopy

The scanning tunneling microscope is one type of the scanning probe microscope family. The STM permits a real-space investigation of atomically resolved metal, semiconducting surfaces and on thin insulators. For that reason, the study of single atoms and molecules has become feasible. In figure 2.1, the principle of scanning tunneling microscopy is schematically illustrated. Usually, a sharpened end of a metallic wire is used as a STM

---

[1] This work led to the Nobel Prize in Physics 1986

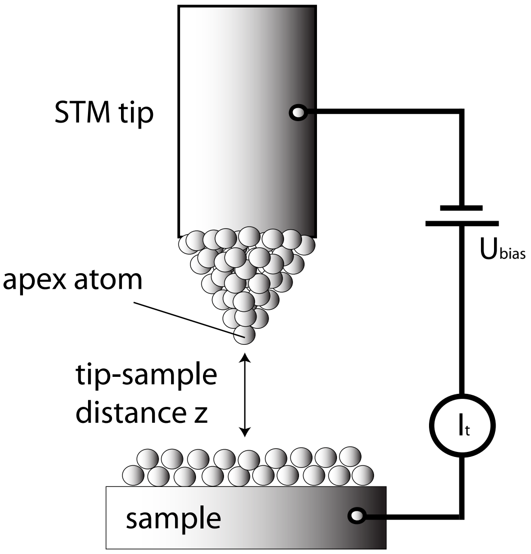

Figure 2.1: A simplified schematics of a scanning tunneling microscope, where the bias voltage U_{bias} with tunnel current I_t is applied between the STM tip and the sample.

tip. Materials such as platinum-iridium, platinum or tungsten are preferred. The tip can be etched mechanically or chemically. It is then mounted on a XYZ scanner, which enables positioning with subatomic precision. For this kind of positioning, piezo actuators are required that show reproducible displacement in the picometer range.

The imaging principle is based on the quantum mechanical tunneling effect that enables electrons to cross a barrier, a gap between the tip and the sample surface. The tip-sample distance for currents between 10^{-9} to 10^{-12}A is smaller than 1nm [25]. The tunneling effect is attributed to the wave nature of the electrons [3, 38, 39, 40]. This property leads to a finite probability for electrons to cross a potential barrier, that is higher than their kinetic energy. If this happens, the tunneling current I_t is exponentially dependent on the tip-sample distance z [41]. A short discourse shall demonstrate this exponential dependence of the tunneling current.

The mathematical first order perturbation treatment of tunneling for a three dimensional barrier starts with the simplified assumption that it is rectangular. The tunneling current I_t between two separate and flat electrodes can be analyzed for a wave function overlap in the following way,

$$I_t(U_{bias}) = \frac{2\pi e}{\hbar} \sum_{\alpha,\beta} \mid M_{\alpha\beta} \mid^2 \delta(E_\alpha - (E_\beta + eV)) \times$$

$$\Big[f(E_\alpha, T)[1 - f(E_\beta, T)] - f(E_\beta, T)[1 - f(E_\alpha, T)] \Big] \tag{2.1.1}$$

where U_{bias} is the applied voltage between the two electrodes. Equation 2.1.1 evaluates the summation of all Eigen-functions Ψ_α and Ψ_β of tip and sample with Eigen-energies E_α and E_β, which corresponds to the Fermi levels $E_{F,tip}$ and $E_{F,sample}$ [41]. The Fermi-Dirac function $f(E,T)$ is the probability at a given temperature T of an occupied electronic state with energy E. Furthermore, the δ function explains the elastic tunneling process. A sketch of the electrodes and the tunneling gap with the bias voltage U_{bias} is illustrated in figure 2.2. Bardeen's tunneling matrix $M_{\alpha\beta}$ evaluates the wave functions

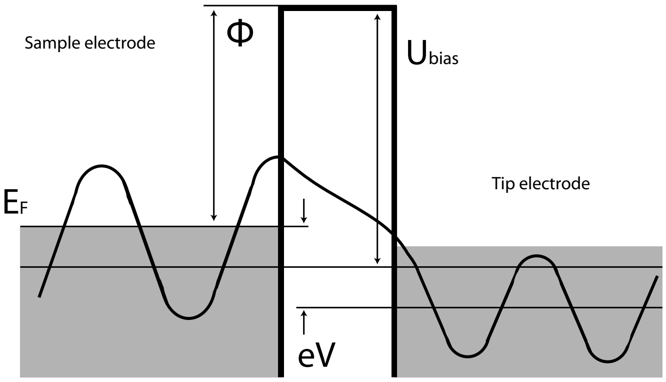

Figure 2.2: This one dimensional energy diagram shows the sample - and the tip electrode. The work function Φ of a metal surface is the smallest amount of energy required to remove an electron from the bulk to the barrier height (vacuum level). When a bias voltage U_{bias} is applied, a tunneling current occurs between tip and sample (Reproduced from [42]).

overlap of Ψ_α and Ψ_β in the tip-sample gap. This is governed by,

$$M_{\alpha\beta} = \frac{-\hbar^2}{2m} \int (\Psi_\alpha^* \Delta \Psi_\beta - \Psi_\beta \Delta \Psi_\alpha^*) dS \tag{2.1.2}$$

where the integration goes over a surface that exists within the gap region [43].

By reducing the conditions to a spherical tip with only s-type wave functions and limited to small voltages and low temperatures, Tersoff and Hamann simplified and calculated the tunneling current in STM [44]. This breaks equation 2.1.1 down to

$$I_t(U_{bias}) = \frac{2\pi e}{\hbar} U_{bias} \sum_{\alpha,\beta} \mid M_{\alpha\beta} \mid^2 \delta(E_\alpha - E_F) \times \delta(E_\beta - E_F) \tag{2.1.3}$$

If the wave functions are applied to the sample and a perfect tip with a curvature radius R at a certain position $\vec{r}_0$, then equation 2.1.3 reduces to

$$I_t(U_{bias}) \propto U_{bias} \rho_t(E_F) e^{2\kappa R} \sum_{\alpha} \mid \Psi_\alpha(\vec{r}_0) \mid^2 \delta(E_\alpha - E_F) \tag{2.1.4}$$

where $\kappa = \sqrt{2m\phi_{eff}/\hbar}$ is the inverse decay length for the wave functions, $\rho_t(E)$ the density of states of the tip and ϕ_{eff} the effective local potential barrier height. As a consequence, the tunneling current I_t corresponds to the *local density of states* (LDOS) of the sample $\rho_s(\vec{r}, E)$ at the position ρ_0 for a constant voltage U_{bias}.

$$I_t \propto \rho_s(\vec{r}_0, E_F) \quad \text{with} \quad \rho_s(\vec{r}_0, E_F) \equiv \sum_{\alpha} \mid \psi_\alpha(\vec{r}_0) \mid^2 \delta(E_\alpha - E) \tag{2.1.5}$$

When scanning with a small voltage at constant current, the contrast in STM images can be understood by equation 2.1.5 as a constant LDOS contour of the sample at E_F. The wave functions decay exponentially in the direction z, which goes vertical with respect to the sample surface. This gives $\mid \Psi_\mu(r_0) \mid^2 = e^{2\kappa(z+R)}$ and can be substituted into equation 2.1.4 and is simplified as

$$I_t = I_0 e^{-2\kappa z} \tag{2.1.6}$$

This is the description of the I_t exponential dependence on the tip-sample z separation, where I_0 is a function of the bias voltage U_{bias}.

2.2 Scanning Force Microscopy

The development of the *scanning force microscope* (SFM) Binnig and Quate brought another contribution to the SPM family [14]. The SFM, otherwise known as the *atomic force microscope* (AFM), can be used to study electrical conductors, semiconductors as well as insulators. Similar to the STM, the SFM uses a sharp tip to probe the sample surface. Instead of a distance dependent tunnel current, the SFM measures the deflection of a microscopic beam that is fixed at one end. A sharp tip is attached to the free end of the beam, where it probes the tip-sample forces. A detector measures the deflection of this beam as its tip scans over the sample, mapping the topography of the surface.

2.2.1 Force Sensor

The key element of a scanning force microscope is the cantilever, which is usually between 100 and 300 μm long and tens of μm wide. Nowadays, they are commercially available in many dimensions. This mechanical lever is not very different from a pickup head of a vintage gramophone. The pickup head of a gramophone is equipped with a needle, that scans the tracks on the surface of a music record disc [45]. In a very similar way, a scanning force microscope requires a sharp tip that interacts with a force at the surface of a sample.

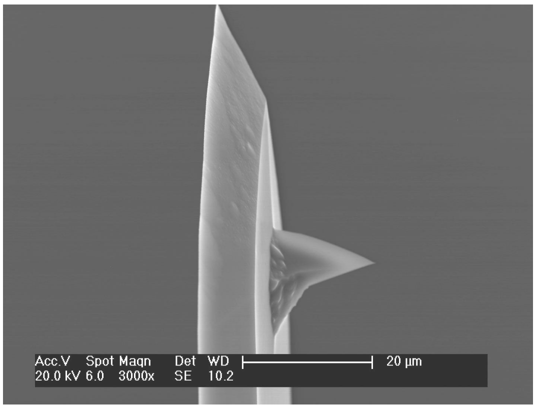

Figure 2.3: A scanning electron microscopy (SEM) of a silicon cantilever with the integrated tip (image taken by Magdalena Parlinska, Empa Dübendorf).

Figure 2.3 shows a *scanning electron microscopy* (SEM) image of a commercial silicon cantilever (Nanonsensors[2], PPP-RT-FMR) and its tip. The tip is integrated at the free end of a flexible beam, whose geometrical and material properties are engineered to obtain high force sensitivity, a suitable stiffness and resonance frequency. The function of the cantilever is to translate the force acting on the tip into a deflection that subsequently can be monitored by various means.

2.2.2 Cantilever Spring Constant

The cantilever is characterized by its resonance frequency *f*, quality factor Q and its spring constant k. A collection of methods are available to measure the spring constant of cantilevers, each with their flaws and advantages [46, 47, 48, 49]. In our case, the fundamental spring constant k of a rectangular cantilever was determined by its geometry [50]. Solving the equation of a clamped vibrational beam, the spring constant k and the resonance frequency of the cantilever f can be obtained [42] [51]. The spring constant is governed by,

$$k = \frac{EWt^3}{4L^3} \tag{2.2.1}$$

where E is defined as the Young's modulus of the cantilever material, W is the width, t is the thickness and L is the length of the cantilever. The resonance frequency f of the rectangular cantilever can also be concluded from the equation of a clamped vibrational beam as:

$$f = \frac{t(1.875)^2}{2\pi L^2}\sqrt{\frac{E}{\rho}} \tag{2.2.2}$$

ρ is defined as the mass density of the cantilever material[3].

By using *scanning electron microscopy* (SEM), the width and length were determined . Figure 2.4 shows the SEM image of a silicon cantilever with the support chip. In addition, if the resonance frequency is known, the thickness t can be extracted from equation 2.2.2. The Q-factor depends greatly on the intrinsic damping mechanisms in the cantilever and its environment (see section 2.2.6). Working in vacuum, the Q factor of cantilevers can reach a few hundred thousand, while in air this value drops to a few hundred [25]. A better way to calibrate the force constant of a cantilever experimentally was suggested by Sader et al. There, the difficulty of the cantilever thickness determination is eliminated [47].

---

[2] www.nanosensors.com

[3] For silicon, $\rho = 2330\ kg/m^3$ and $E = 1.69 \text{ x } 10^{11}\ N/m^2$.

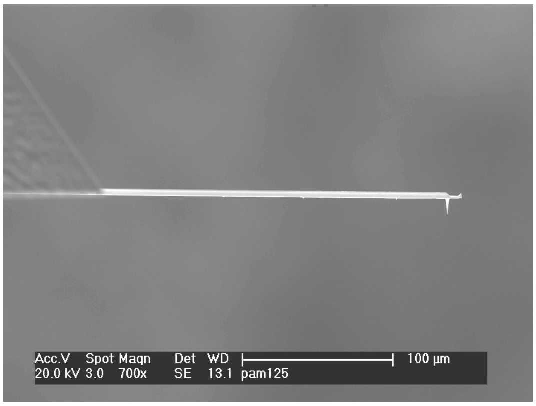

Figure 2.4: A SEM image of a cantilever and its support structure on the left hand side (image taken by Magdalena Parlinska, Empa Dübendorf). The nominal parameters of this type of cantilever from Nanosensors are: k=2.8N/m, f_0=75kHz, L=225μm, W=28μm, T=3μm.

2.2.3 Interaction Forces

In AFM, the interaction forces between tip and sample can be distinguished between long range forces and short range forces. In dynamic force microscopy, the cantilever and the tip contribute differently to the total force being measured. The long range electrostatic forces act on the cantilever as one single macroscopic object, whereas the long range Van der Waals forces have an impact between the tip's end and the sample surface. In comparison, short range chemical forces only perturb a few atoms in the vicinity of the tip apex. *Non-contact AFM* (nc-AFM) imaging with true atomic resolution requires forces that interact within the local area of the surface atoms [30]. Therefore, short range forces must be separated from the total measured interaction force by a systematic method, introduced by Guggisberg et al [53]. Figure 6.16 shows the individual forces contributing to the total force.

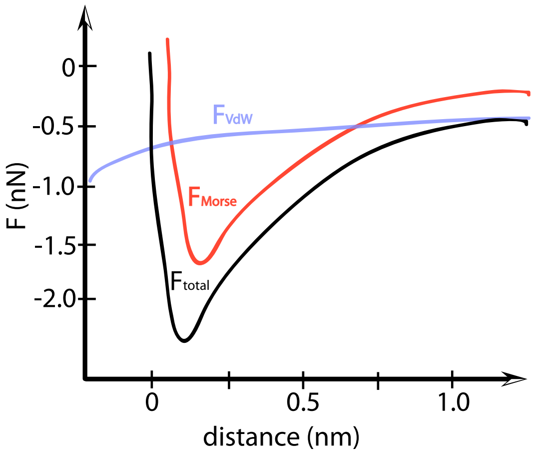

Figure 2.5: The total force curve (black) contains of long range Van der Waals forces (light blue) and short range Morse forces (light red). The total force gets more attractive when the distance decreases towards zero. However, beyond the turnaround point it becomes repulsive across a short distance (reproduced from [52]).

Electrostatic forces

In general, a contact potential difference arises through the electrostatic forces acting between tips and samples, resulting in localized charges. By applying a bias voltage, they can only be partially compensated because of the uneven tip shape [54]. If we consider the tip and sample to be the electrodes of a capacitor, then C represents the distance dependent capacitance which is governed by the electrostatic force,

$$F_{electrostatic} = \frac{\partial C}{\partial z}(U_{bias} - U_{\Delta cp})^2 \tag{2.2.3}$$

where U_{bias} is the tip-sample bias voltage and $U_{\Delta cp}$ is the contact potential difference triggered by the different tip-sample work functions [25]. Without compensation of the long range electrostatic forces, height measurements in nc-AFM can be affected, particulary with heterogeneous materials [55].

Van der Waals forces

The weak attractive Van der Waals forces are intermolecular forces which contain dipole to dipole and dispersion forces [56]. According to Israelachvili's work [57], the general expression of the Van der Waals potential between a sphere with radius r and a flat surface separated from each other by the distance d is expressed as follows.

$$U_{VanderWaals} = -(\frac{rH}{6d}) \tag{2.2.4}$$

H is called the Hamaker constant and depends on the material being used [58].

Chemical forces

Short range chemical forces are either attractive or repulsive, depending on the tip-sample separation. When the distance between the apex atom of the tip and the sample surface decreases to the atomic scale, repulsive short range chemical forces arise from valence electrons of closed shells which overlap. This can be explained by Pauli's exclusion principle [59]. However, if the interacting atoms do not have closed shells, covalent bonds can occur and give rise to attractive chemical forces that bind tip and surface atoms to one another. The total interaction potential between a pair of molecules or atoms can be modeled by the Lennard Jones potential, which includes two terms that describe the attractive and repulsive potentials. It is also known as the "6-12" potential and is given below.

$$U_{LennardJones} = -E_{bond}(2\frac{\sigma^6}{z^6} - \frac{\sigma^{12}}{z^{12}}) \tag{2.2.5}$$

The equilibrium distance is represented by σ and E_{bond} is the bond energy [57].

2.2.4 Dissipation

Energy dissipation can be divided into several different processes. But the two relevant processes are emphasized here. Energy dissipation induced by tip-sample interactions is still not well understood. Theoretical works have been presented in several articles, explaining the complexity of the energy loss due to these interactions [60, 61, 62]. On the other hand, experimental determination of energy dissipation induced by tip-sample interactions in nc-AFM can be summarized in the works of Denk et al and others [63, 64, 65].

Intrinsic Dissipation

A cantilever with a resonance frequency f_0 oscillating far away from the surface, experiences internal friction within its beam structure. Moreover, acoustic vibrations traveling along the cantilever into the support chip and therefore contribute to the lost energy per oscillation cycle. This is known as the intrinsic dissipation of energy in a cantilever, which cannot be hindered. This intrinsic energy loss of each oscillation cycle for an high quality factor cantilever can be written as,

$$E_0(A) = \frac{\pi k A^2}{Q_0} \tag{2.2.6}$$

where A is the tip oscillation amplitude, k stands for the spring constant and Q_0 is the intrinsic quality factor. Q_0 depends on the cantilever's geometry and its material, the geometry of the support structure. Q_0 is also affected by reflective coatings [66].

Apparent Dissipation

In nc-AFM measurement configurations where a constant oscillation amplitude of the cantilever is maintained, a driving voltage A_{drive} excites the cantilever with a piezo actuator. Because of tip-sample interactions, energy dissipation can occur. This energy loss per oscillation cycle is described with the intrinsic quality factor Q_0 and the quality factor Q of the cantilever while interacting with the surface [66].

$$E_{ts} = (\frac{Q_0}{Q})E_0 \tag{2.2.7}$$

During tip-sample interactions, the harmonic oscillation of the cantilever can be distorted. This leads to a partial energy transfer to other oscillation overtones. To compensate for this energy loss, the excitation voltage A_{drive} increases accordingly. This measured voltage variation is known as the damping signal and does not represent the energy dissipation induced by tip-sample interactions. The damping signal is also called apparent damping or apparent dissipation. Apparent dissipation also appears when the phase shift between the eigenfrequency of the cantilever f_0 and the excitation signal f_{drive} cannot be maintained constant at 90° anymore. The driving voltage A_{drive} increases to keep a constant oscillation amplitude. The damping signal can be misinterpreted as the actual energy dissipation, in cases where the phase is not monitored.

2.2.5 Frequency Shift and Forces

The resonance frequency of the cantilever changes upon tip-sample approach and therefore gives us a way to detect interaction forces between atoms. *Frequency modulation atomic force microscopy* (FM-AFM) makes use of this simple relation, allowing the frequency shift to be determined for a given force. The work done by Sader and Jarvis [67] puts this relation in an expression for the force in terms of the frequency shift,

$$F(z) = 2k \int_{z}^{\infty} (1 + \frac{A^1/2}{8\sqrt{\pi(t-z)}})\Omega(t) - \frac{A^3/2}{\sqrt{2(t-z)}} \frac{d\Omega(t)}{dt} dt \qquad (2.2.8)$$

where $\Omega\ (z) = \Delta\omega\ (z)\ /\ \omega_0$. F is the tip-sample interaction force, k is the spring constant of the cantilever, A is the oscillation amplitude, and z is the distance at closest tip-sample separation. $\Delta\omega$ is defined as the frequency shift and ω_0 is the eigenfrequency. The equation 2.2.8 is valid in the case where the cantilever oscillation amplitude is kept constant. Independent of the tip-sample distance, this equation exhibits global validity to any force law and applies to small and large amplitudes or any arbitrary oscillation amplitudes. Figure 2.6 depicts the frequency to distance curve with a compensated contact potential.

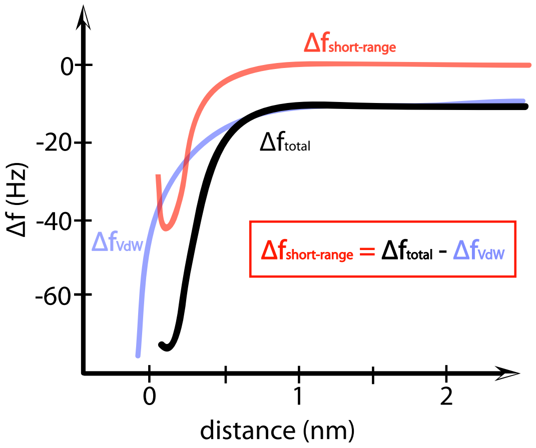

Figure 2.6: This frequency shift to distance curve shows the contributions from the long-range Van der Waals forces and the short-range chemical forces. $\Delta f_{chemical}$ results from the subtraction of the Δf_{VdW} curve from the Δf_{total} (reproduced from [68]).

2.2.6 Force Detection

In scanning force microscopy, the free end of the beam gets deflected by the interacting tip-sample forces. There are a several methods available, which can be applied to detect the deflection of the cantilever. Listed below are a few deflection measurement techniques that are used in many different applications.

- In the original force microscope of Binnig et al, the cantilever deflection was detected by means of a *tunneling current* from the cantilever to an STM tip positioned at the rear side of the cantilever [14]. This very sensitive setup is complicated by the additional force between the STM tip and the cantilever.
- The change in the *capacitance* between cantilever and an electrode can be used to detect its deflection [69]. Using micro-fabricated capacitive sensors, this method is able to perform very fast measurements. Disadvantages with this kind of sensors are the undesirable force between cantilever and electrode and its susceptibility to electrical noise sources [70].
- Other groups successfully demonstrated the use of *piezoresistive* cantilevers that is basically a self sensing device [71, 72, 73]. Despite the advantages of this detection method (simple and compact), the poor resolution has not been improved since it was first demonstrated by Güthner et al [74]. Quartz tuning forks show similar features but can be operated with oscillation amplitudes well matched to the decay length of atomic interaction forces, allowing high signal to noise ratio in atomic resolution imaging [75]. Quartz tuning forks are cheap piezoelectric sensors with high frequency and high spring constant. High resolution images in dynamic mode have been attained with quartz tuning forks [76, 66, 77].

Other methods for the detection of the cantilever's motion were introduced. Optical techniques proved to be a suitable alternative to the STM tip for monitoring the deflection of cantilevers [78]. Although, the optical sensors exert a negligible force on the cantilever, photon-induced forces are the basis for cantilever cooling experiments described in chapter 7.

- Laser *beam deflection* is commonly used because it is relatively simple to implement [79]. The laser light reflects on the backside of the cantilever to a four-quadrant photodiode, where the bending in the vertical direction can be detected. Furthermore, simultaneous detection of the flexural and torsional motion of the lever can be tracked by this position sensitive photo detector [80].

- The cantilever is used as one mirror of a laser *interferometer* to detect its own motion [81]. With this method, the deflection can be calibrated by the wavelength of the laser. In addition, interferometric detection is often used in tight and compact designs such as in low temperature systems, where space is confined. The sensitivity of this optical detection method is only limited by the thermal noise of the cantilever. Interferometric methods offer superior position sensitivity. For this reason, we and some other research groups have implemented interferometers (see chapter 5) in our low temperature systems.

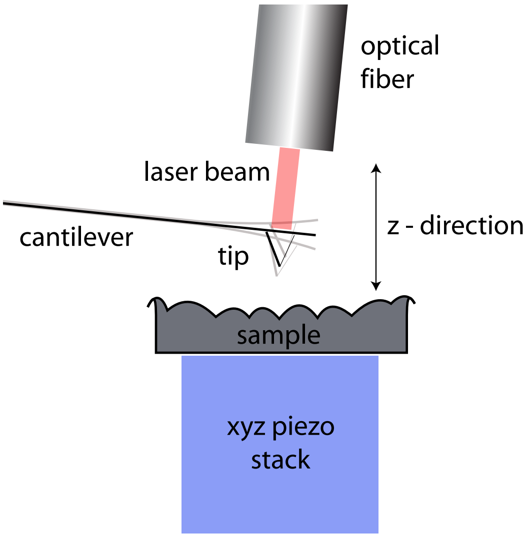

Figure 2.7: The bending of the cantilever due to the tip-sample interaction is measured by an optical interferometer.

Figure 2.7 illustrates such a detection scheme with an implemented optical fiber interferometer. Depending on the application and design, the cantilever moves relative to a fixed sample stage or vice versa.

2.2.7 Modes of Operation

There are different modes of operation that are available for different applications. Depending on the sample to be investigated, contact mode or tapping mode may be favored. However, in this line of work the concentration will be particulary on the non-contact mode of operation. Advantages and disadvantages of these modes are discussed in literature [82, 24, 77].

Non-Contact Mode

In nc-AFM, dynamic AFM operation modes are usually employed. The dynamic properties of the cantilever are measured, which include the resonance frequency, phase, oscillation amplitude and the excitation amplitude. True atomic resolution images comparable to STM imaging can then be obtained. Dynamic operations can be grouped into off-, near- and on resonance modes. Figure 2.8 illustrates the different non-contact modes at various frequencies.

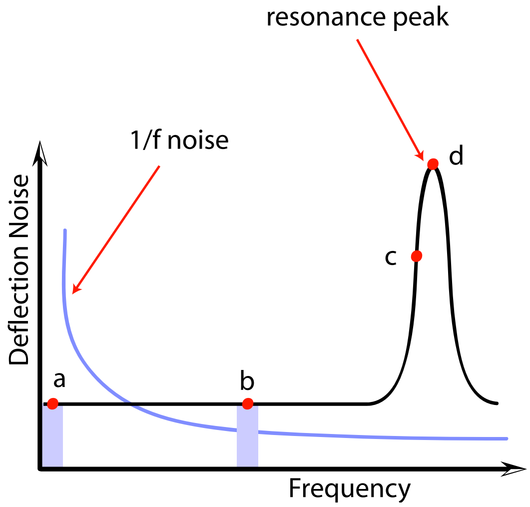

Figure 2.8: An overview of non-contact operation modes: (a) DC-operation mode has a typical detection bandwidth of 0 to 1kHz. (b) Off-resonance mode has a small bandwidth of 1kHz but the detection frequency $f_0 \approx$ 30kHz. (c) Near resonance and (d) on resonance modes.

- The first two modes (**a** and **b**) excite the cantilever at a frequency far away from the resonance of the cantilever. The oscillatory variation of the tip-sample distance induces a corresponding oscillation of the tip-sample force and changes the oscillation amplitude of the cantilever [78]. In principle such an off-resonance mode is a quasi-static mapping of the cantilever deflection avoiding the 1/f noise at low detection frequencies and therefore, suffers from low signal to noise ratio.

- Alternatively, the cantilever oscillation can be driven near resonance (**c**) or on resonance (**d**). At near resonance, the cantilever is driven with a fixed frequency. The tip-sample interaction forces then lead to a shift of the cantilever's resonance frequency and to a corresponding change of the oscillation amplitude and phase. This operation mode is often referred to as the AM-mode [27].

- The on-resonance mode (**d**) uses a self-excitation circuitry or *phase locked loop* (PLL) to drive the cantilever on or very near its resonance. If the cantilever is driven by a PLL circuitry, the drive frequency is adjusted to keep the phase between the drive and the cantilever oscillation signal constant at 90°. If the PLL keeps the phase perfectly constant and the drive frequency was initially set to match the free resonance of the cantilever, the frequency shift can be accurately tracked (see figure 2.9). In the self-excitation scheme the signal from the oscillating cantilever is phase shifted and fed back to the oscillation amplitude. The phase is tuned to obtain the lowest excitation amplitude, but then is fixed at that value. In both schemes, the oscillation amplitude of the cantilever is kept constant by appropriately adjusting the drive amplitude. A more detailed explanation of the PLL and the *self-excitation* (SE) schemes can be found in section 4.2.

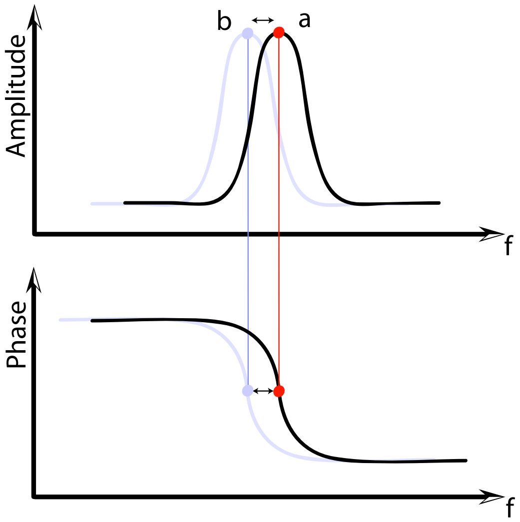

Figure 2.9: PLL-excitation scheme: when the cantilever is driven at a fixed frequency, the phase is adjusted and kept constant at 90°.

2.2.8 Small Oscillation Amplitude

Theoretical works of Perez et al have suggested that atomic imaging contrast may occur from short range interaction forces due to covalent chemical bonding [83]. Long range interaction forces act in the background, which depend on the electrostatic potential and the shape of the tip. An sharp tip with a high aspect ratio can minimize the Van der Waals long range force contribution, whereas the electrostatic potential can be compensated. To enhance the signal to noise ratio and the detection sensitivity of short range forces, a small cantilever oscillation amplitude that is equivalent to the short range interaction decay length (≈0.2nm.) is necessary [84, 85]. Two stability criteria must be achieved. The first stability criterion requires the cantilever stiffness to be larger than the force derivative of the tip-sample force:

$$k > \frac{\partial F_{ts}}{\partial z} \tag{2.2.9}$$

Second, attractive forces increases the probability of "tip to sample" jumps, when the closest tip-sample separation in an oscillation cycle is equivalent to the interatomic distance [86]. The energy stored in a cantilever E_{Cl} is,

$$E_{Cl} = \frac{1}{2}kA^2 \tag{2.2.10}$$

where k is the spring constant and A the amplitude. Following that, the intrinsic energy loss per cycle is governed by,

$$E_0 = 2\pi\frac{E_{Cl}}{Q} = \frac{\pi k A^2}{Q} \tag{2.2.11}$$

which is maintained by the drive amplitude:

$$A_{drive} = \frac{A_0}{Q} \tag{2.2.12}$$

Here Q represents the quality factor, A_{drive} the driving amplitude and A_0 the freely oscillating amplitude. Furthermore, there are two solutions that offer stable small amplitude operation while satisfying the mentioned conditions [26, 87]:

- Stiff cantilevers with spring constant higher than 500N/m are commercially available.
- The effective stiffness of the second resonance mode of commercially available cantilevers is ≈40 times larger than the fundamental mode (see below) [88].

The effective second mode stiffness of a given cantilever can be estimated by the equivalent point mass model as proposed by the work of Melcher et al [88]. Then, a rough estimation can be made for a rectangular cantilever clamped at one end and free at the other end:

$$\frac{k_{2nd}}{k_{1st}} \approx \left(\frac{f_{2nd}}{f_{1st}}\right)^2 \approx 40 \tag{2.2.13}$$

The ratio of 6.24 between the fundamental frequency f_{1st} and the second mode frequency f_{2nd} is used to approximate the effective stiffness of the second cantilever oscillation mode.

Part II

Instrumentation

Chapter 3

The home-built SPM

3.1 Technical Considerations

There are some technical challenges regarding the instrumentation of the SPM that must be considered, before a successful construction of such a complex system should be started. A thought-through design and planning of the system is one thing. The actual construction work and then the subsequent characterization of the prototype is a different issue. However, the planning phase critically determines the outcome of the system. Below are some major requirements highlighted.

- Even though, Fukuma et al have shown that optical beam deflection systems can be used to detect subnanometer cantilever oscillation amplitudes in liquid conditions [32], it cannot be employed in a UHV LT-SPM system, because of space constraint. Furthermore, these detection sensors are not designed to be operated at liquid helium environments. Optical interferometric detection have proven to fit this purpose, but exhibit photon-induced effects on the cantilever. See chapter 7.
- The *scan range* in the Z direction should be large enough to allow a safe approach. Steps of piezo motors can be below 50nm, so a Z range between 100nm and 1μm is possible. The scan range in the lateral directions should be adapted so that the imaging of atoms becomes possible. At low temperatures the piezo effect of typical piezo ceramics is reduced by a factor of 5 to 8. A lateral scan range of 0.5 to 1 micron at 77K or 4K is a good "figure of merit". The operation at low temperature enhances the piezo stability and creep compensation can be omitted [89].

- The microscope and the *piezo scanner* must have high resonance frequencies to allow a fast Z feedback which enables fast scanning. In addition, a high resonance frequency makes the microscope tip-sample gap less sensitive to external vibrations.

- *Coarse positioning* is the ability to move the sample relative to the tip in the XYZ directions. For this purpose, 5 piezo stack motors made of 4 shear piezo plates are used for each direction.

- Good choice of *materials* must be considered, because they operate in vacuum and in cryogenic environments. Thermal drifts usually moves the sample away from the scanning area. Therefore, a symmetrical construction of the microscope and materials with similar thermal expansion coefficients minimize the strains between different parts of the microscope [90, 91]. Moreover, materials with good thermal conductivity provide homogenous thermal distribution and stable cryogenic operation condition. All of the above result in the reduction of the thermal drift.

- *Wiring* requires some demanding work because there are more than 50 wires attached to the microscope and along the cryostat in vacuum. Several aspects such as vacuum compatibility, the choice of good and low thermal conductivity of wires must be considered. In addition to the latter, thermal anchoring of the wires is required to avoid heat loss via the wires. Furthermore, some of the lines have to handle high frequencies and higher voltage operations. Signal lines must be adequately shielded from internal stray capacitances and external electromagnetic fields.

- The operation of the SPM in *ultra high vacuum* brings along some benefits. Condensation onto tip and sample is prevented during the cool down from room temperature. Water vapor can be decreased during bake out, when the vacuum chambers are pumped for a few days at 120°. Additionally, because of the reduced number of molecules in the vacuum chambers, the Q-factor of the cantilever can reach higher values than in ambient conditions [92, 22]. Vacuum operations however require samples and tips to be exchangeable in-situ. The microscope must feature vacuum exchangeable sample and tip holders. Transfer and manipulation tools must be installed in the UHV chambers.

- *External vibrations* is a known issue in SPM. Among the common sources of external mechanical noise such as floor and acoustical vibrations, the bubbling of the cryogenic liquids generates additional noise, especially liquid nitrogen. Low frequency vibrations coming from the buildings are difficult to eliminate. Thus, situating the system in the basement should be favored. Additional options with passive floating air legs or active piezo-electric dampers are helpful. A more specific discussion of vibration isolation of the microscope can be viewed in section 3.4.1.

3.2 Ultra High Vacuum System

Most of the measurements presented in this work are from experiments performed on the home built LT-SPM. The design of the Empa system is based on the concepts of the low temperature SFM system at the Department of Physics, University of Basel [89], that is still in operation. There are a numerous add-on's and new developments, which eases the handling of sample and probe transfer and manipulation. This also applies to maintenance works during which the instrument is taken apart. Special attention was paid to the *modularity* of the microscope that allows the exchange of each module. This simplifies the development and repair of the system. In figure 3.1 there is an image of the overall system from the side and from the top.

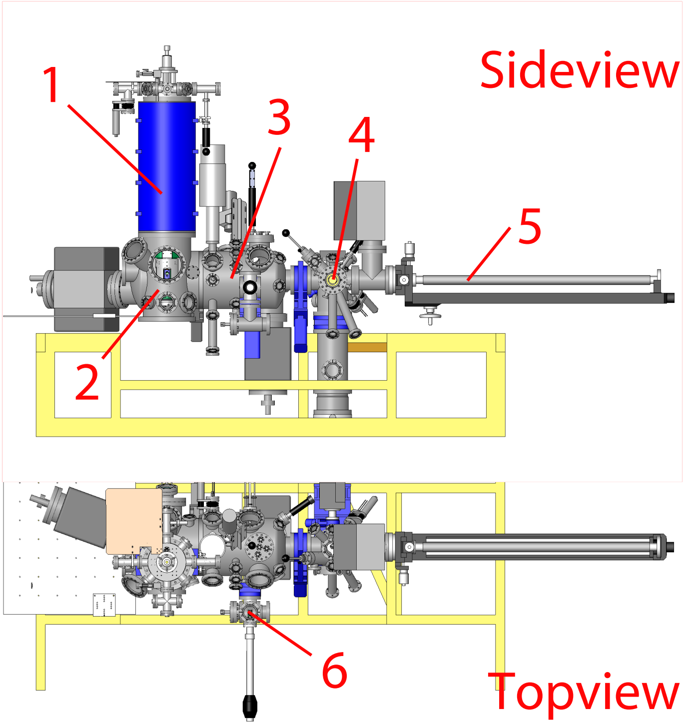

Figure 3.1: The overall system layout and peripheral devices. (1) Cryostat (2) AFM chamber (3) Preparation chamber (4) FIM chamber (5) Cryo-manipulator (6) Fast entry load lock chamber.

3.2.1 Chambers

The vacuum chambers were manufactured by CreaTec GmbH according to our design specifications[1]. Several flanges were considered for possible future upgrades and modifications. Examples are the attachments of a *low energy electron diffraction* (LEED) or a magnet system through the bottom flange. The UHV system consists of three chambers, which are separated by manually operated gate valves that can withstand a differential pressure up to 1 bar in either direction[2]. An additional valve separates the *field ion microscope* (FIM) chamber from the main turbo molecular pump[3]. The AFM- and Preparation chambers are also equipped with each a 240 l/s ion pump and an integrated titan sublimation pump. All three chambers also have each a hot cathode ion pressure gauge from Granville Phillips, which are calibrated for nitrogen gas.

A load lock chamber allows a rapid transfer of samples and cantilevers from air to UHV and vice versa. This entry air lock is pumped through a small turbo molecular pump[4].

AFM Chamber

The microscope is located in the AFM chamber, where it is attached underneath a bath cryostat. A StarCell (VacIon Plus 300) Varian ion pump with an integrated *titan sublimation pump* (TSP) deals with the remaining atmospheric molecules. The combination of both types of pumps is most effective, since the TSP gets rid of hydrogen and nitrogen, and the ion pump takes care of non-getterable gases such as methane and argon. A carousel is mounted in the chamber so that five sample- and/or cantilever holders can be parked for later retrieval. The wobble stick, which is nothing else than a short manipulator with retractable hexagonal screw driver, is built in the chamber for the transfer of samples and cantilevers between the cryo-manipulator (section 3.2.2) and the microscope.

Preparation Chamber

This chamber is designed for various preparatory works such as cantilever tip sputtering, silicon sample preparations and in situ coating of the cantilever back end with gold. All preparation works are done on the cryo-manipulator that holds two positions for samples and cantilevers. Similar to the AFM

---

[1] www.createc.de

[2] However, the maximal differential pressure should not exceed 30mbar while opening

[3] Pumping speed: 520 l/s

[4] Pumping speed: 70 l/s

chamber, this one includes a carousel with five parking positions and a wobble stick (small manipulator).

FIM Chamber

The main purpose of this chamber is to enable *field ion microscope* (FIM) measurements of tip-shaped samples. In our case, the FIM will be used to characterize tunneling tips and tips on cantilevers. The FIM shows the hemispherical surface of a tip on a fluorescent screen. Since there is no other way to know for certain what is at the probing tip, the FIM provides the possibility to directly displaying the atoms of a given cantilever tip before and after a scanning experiment. Visualization of tungsten atoms at a field emitter's tip apex, was first demonstrated by Erwin W. Müller [35].
Next to its primary function, the FIM chamber also serves as a junction, where the cryo-manipulator is attached. The main turbo molecular pump is connected to this chamber and separated by a gate valve.

3.2.2 Cryo-manipulator

The cryo-manipulator serves as the main transport system and holds two receiver positions for sample and cantilever holders. The first receiver position

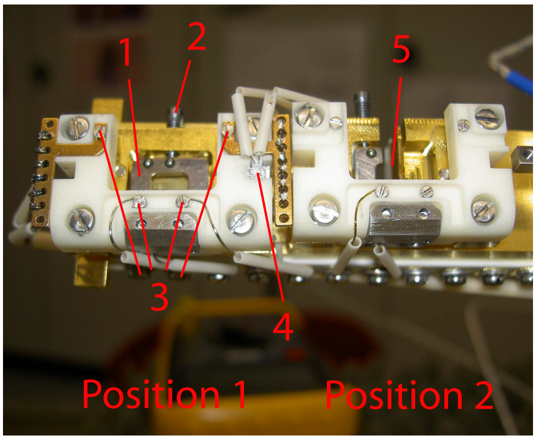

Figure 3.2: The manipulator head with (1) clamping spring lever (2) clamping screw (3) stainless steel contact screws (4) PT100 temperature sensor (5) narrow slit for in-situ coating of the cantilever's backside.

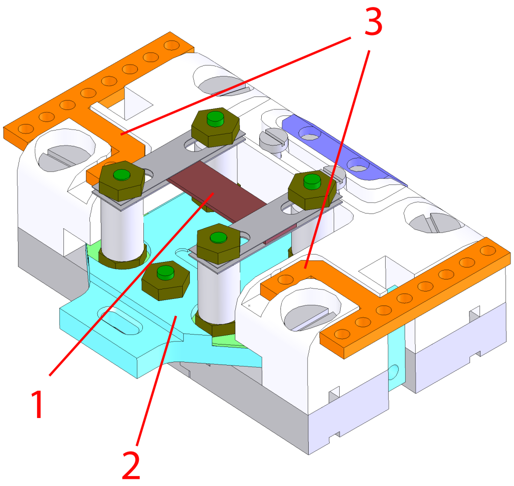

Figure 3.3: Close up of the parking "Position 1" and its details. 1) sample 2) sapphire sample plate 3) CuBe direct current contact strips.

allows silicon samples to be heated with direct current. With two contacts, an electrical current up to 10A can be passed across the sample. This is used for silicon sample preparations (see section 6.2). Moreover, the first position is thermally insulated from the cryostat head by a sapphire plate. Temperatures of up to 800°C can be reached with a built-in resistive heater with a minimized heat load to the sensitive parts of the cryostat head. At low temperatures the sapphire plate still allows efficient cooling to about 15K. To date this heater was used to outgas the sample plate and get rid of water vapor. The second position on the manipulator is designed for coating the cantilever's backside with gold, so that the reflection of the laser light is enhanced. It can also be used to park or transport samples and cantilevers between the chambers. In addition, the wiring of the second position can take voltages up to 10kV for FIM operations. Another resistive heater is integrated in the bulk of the manipulator head. This one is able to heat both parking positions up to 200°C.

There is a wobble stick in each of the two main (Preparation, AFM) chambers. The transfer of samples or cantilevers between the load lock fast entry chamber and the manipulator two parking positions, is straightforward. With the wobble stick in the AFM chamber, the in-situ exchange of samples and cantilevers is easily done and reduces the turn around times. The transfer of a sample from the AFM with the cryo-manipulator to the fast entry load lock chamber typically takes 10 minutes.

3.2.3 Cryostat

The bath cryostat fulfills the function of cooling the microscope to cryogenic temperatures. This custom designed cryostat consists of two storage tanks, which are separated by vacuum. The volume of the inner tank holds 8 liters of liquid helium (LHe). The 18 liters liquid nitrogen (LN2) outer tank serves as a radiation shield for the inner tank. Thus, LHe refilling is required every 5th day. This allows long time operations of the system. After 2 days however, the LN2 tank runs empty[5]. This restricts the measurements time to about 50 hours, when the sample temperature rises and induces thermal drift.

If the LHe level is higher than that of the outer tank, exposing it to the ambient temperature, it boils off quicker than usual. This again shortens the measurements time even further. Thus, the relatively small outer tank has to be replenished every 24 hours to maintain its level not lower than 50% and always higher than that of LHe. In addition, the bubbling of the LN2 cannot be avoided. If this affects the measurement environment, solidifying LN2 by pumping[6] is a feasible solution.

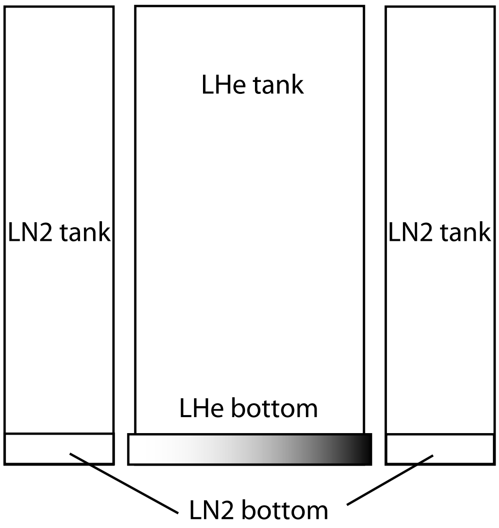

Figure 3.4: The bath cryostat is divided into 2 tanks. The inner tank holds 8 liters of LHe and the outer tank holds a volume of 18 liters of LN2.

Each of the cryogenic tanks possess a bottom part with a thickness of 15mm, the outer ring and the inner disc. In figure 3.4, the cryostat tanks with

---

[5] Note: this issue is resolved in the new cryostat used in the next generation MD-SPM system.

[6] The melting point of liquid nitrogen is at 63.3 Kelvin.

their bottom parts are illustrated. They are fitted with drill pits so that the cryogenic shields can be fixed with screws, once the microscope is mounted and adjusted. The cryostat bottom parts are made of gold-plated *oxygen free high thermal conductivity* (OFHC) copper for best heat transfer.

A meander-like tube serves to guide the optical fiber along the cryostat, while avoiding possible direct light radiation coming from the outside. Small considerations like this one are most crucial to the overall thermal insulation. The next section shows what measures were taken to ensure stable cryogenic performance of the microscope.

3.2.4 Tail and Shutters

At the bottom of the cryostat, a tail of two polished, cryogenic shields is mounted that encloses the microscope's inside. In figure 3.5 The inner, gold plated copper shield is fabricated from a single OFHC copper piece. This so called He shield maintains a constant LHe temperature, once the inner tank of the cryostat is filled. Similarly to the latter, the outer shield is machined from a single block of aluminium and is attached to bottom of the LN2 tank. Both shields have not only the purpose to reflect thermal radiations from the environment, but also to shield the microscope from external electromagnetic radiations.

To allow the transfer of sample or tip holders between the AFM and the cryo-manipulator, linear feed-through activates a pulley system that pulls down the microscope into a locked position. The shutters are opened by a second pulley system. Three windows in the shields enable users to view tip & sample during these manipulations and during the coarse approaches. In the locked position, a gold-plated copper cone which is part of the microscope, makes physical contact with a conical counterpart of the inner shield. This allows a rapid cooling of the microscope.

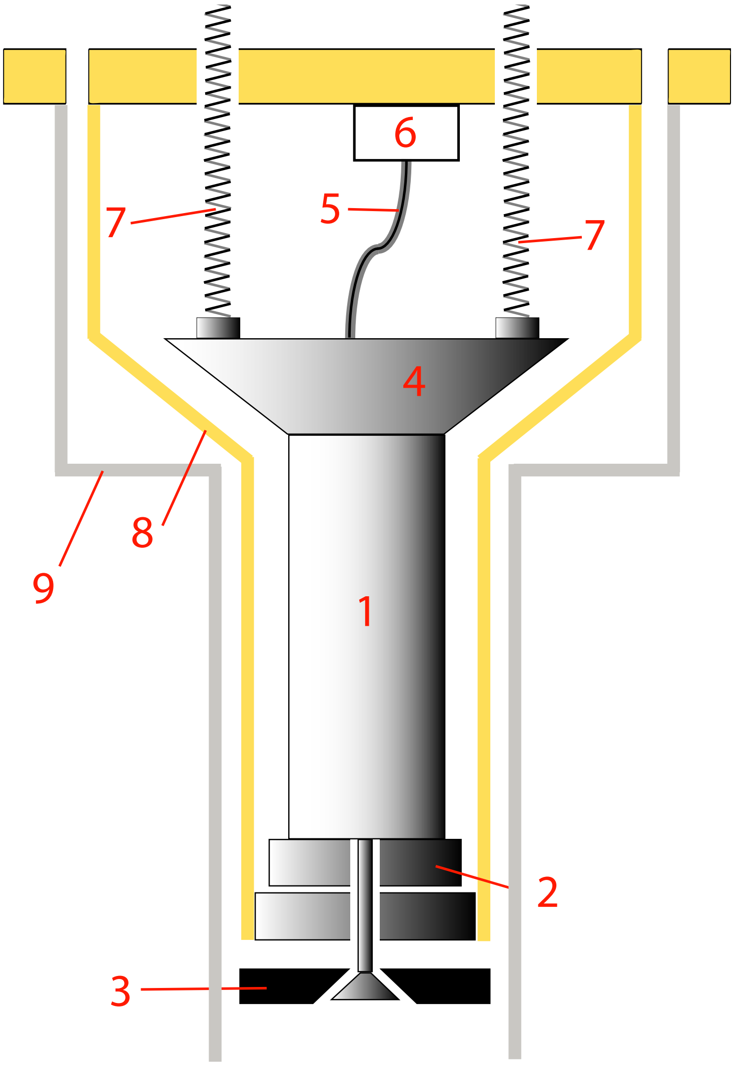

Figure 3.5: The tail with the microscope seen from its cross-sectional view. (1) The SFM hangs freely, (2) the eddy current damping. (3) The pull down components for the SFM docking mechanism. (4) The cone is fit so that it makes large area contact to the LHe shield. (5) Wires and cables. (6) Thermal grounding for the cables. (7) Suspension springs. (8) LHe - and (9) LN2 shield.

3.3 Microscope

The atomic force microscope is attached to the top of the LHe tank with three suspension springs for vibrational damping. These springs have a diameter of 1mm and are fit in a 2mm tube along the LHe tank. They are electrically and thermally isolated from the tank. With a voltmeter, accidental contacts between the microscope and the LHe shield can be verified, while the latter reduces the heat load to the microscope. A final sample temperature of 4.5K could be reached because all electrical wires going to the microscope are thermally anchored to the bottom of the LHe tank. A low quality factor (≈6) of the microscope suspension system is obtained with an eddy current damping system attached to the microscope base. Figure 3.6 illustrates this setup. The microscope consists of 4 main units (see figure 3.7. (1) A sample XYZ positioning unit carries (1a) the sample scanner and (1b) the sample holder receiver that can be loaded with (1c) the sample . (2) A optics XYZ positioning unit allows to position (2a) the Fabry-Perot optical sensor relative to (3) the cantilever-holder receiver that can be loaded with the cantilever-holder (3a). The positioners of the sample (1) and the optics (2) cam move

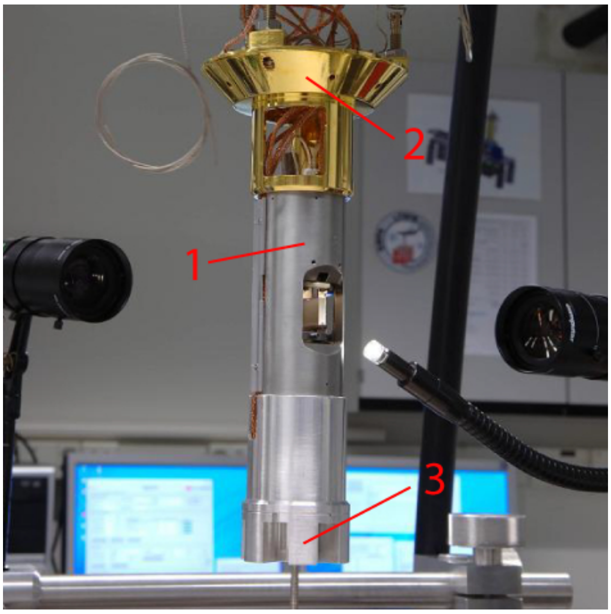

Figure 3.6: The microsope (1) attached to the gold-plate copper cone (2) at the top and to the eddy current damping aluminum fins (3) at the bottom. The windows in the microscope body (1) match to corresponding windows in the cryostat tail so that a tip and sample exchange is possible.

along the z-direction inside the microscope's main body (4). Most of the body parts are made out of pure molybdenum to have a good heat conductance combined with a low mechanical quality factor and a high body stiffness.

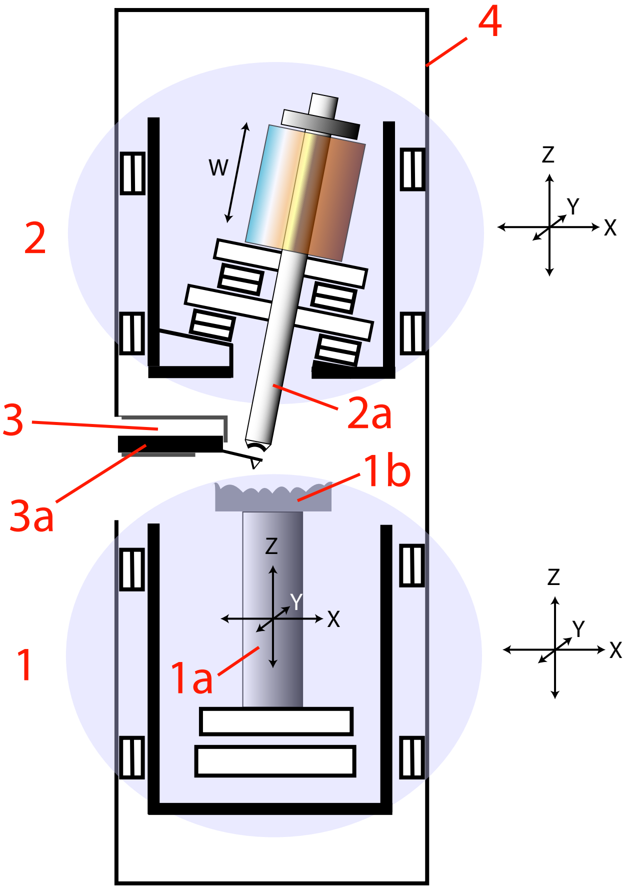

Figure 3.7: This cross sectional illustration shows the details of the microscope, which consists of four main parts. (1) Sample positioner. (2) Optics positioner. (3) Cantilever holder receiver. (4) Main molybdenum body of the AFM.

3.3.1 Optic XYZ Positioning Unit

The optic positioner consists of a molybdenum body, that acts as a backbone, where as many as 60 individual parts are attached to it. There are a total of 3 × 5 piezo stacks, responsible for the XYZ coarse adjustment of the Fabry-Perot optical sensor relative to the spatially fixed cantilever. A Fabry-Perot optical sensor is mounted inside a tubular piezo stack (W-piezo) to adjust the optical cavity formed between the final concave lens and the cantilever. This W-piezo itself is mounted on sapphire plates that enables the movement in the XY. The range of the piezo motors in the XY directions is mechanically restricted to ±0.5mm. For the coarse adjustment of the optical cavity, the whole optics positioning unit moves along Z inside the microscopes main body. A range of approximately 15mm is available to fully retract the optics during cantilever exchanges.

3.3.2 Sample XYZ Positioning Unit

The design of the sample positioning unit is similar to that of the optics positioning unit, but has a ±5mm travel range along XY to move the sample relative to the spatially fixed tip. The travel distance of the Z piezo motors is designed for a 20mm range. This positioning unit includes as many as 80 individual parts. A rough sketch can be seen in figure 3.7. The piezo scanner sits on two sapphire plates and is mounted at the center of the molybdenum main body. On top of the piezo scanner, the sample receiver is attached. This receiver has the same functionality as the cantilever receiver explained in section 3.3.3.

3.3.3 Cantilever Holder, Receiver and Piezo Tube Scanner

STM tips and samples are mounted on sapphire base plates to enable quick and simple exchanges. To maximize the turn around time of such a mechanism, any given tip and sample exchange system should contain the following requirements:

- Allows rapid, in-situ, safe to operate exchange with one manipulator.
- Rigid fixation of the sample or cantilever.
- Reliable multi-pin electrical contacts.
- Good thermal contact.
- Low wear, low particle generation during exchange operations.

Cantilever Holder: The base plate of the cantilever holder is made of sapphire. This base plate with all the cuts and grooves is constructed in such a manner, so that ad hoc modifications can be done. Figures 3.8 and 3.9 demonstrate how complex this piece actually is, despite its simple appearance at first glance. All parts which are mounted on this base plate are made of molybdenum, except for the oscillation piezo. The cantilever itself is glued on a tower, that is slanted 11°. The oscillation piezo is fixed underneath the tower.

Cantilever Holder Receiver: Once the cantilever is inserted into the receiver, a stainless steel screw pushes the CuBe spring lever in the receiver and clamps the sapphire plate from beneath. A groove in the base plate enables the spring lever to hold it in a fixed position (see figure 3.9). Figure 3.10 illustrates the clamping mechanism in detail.

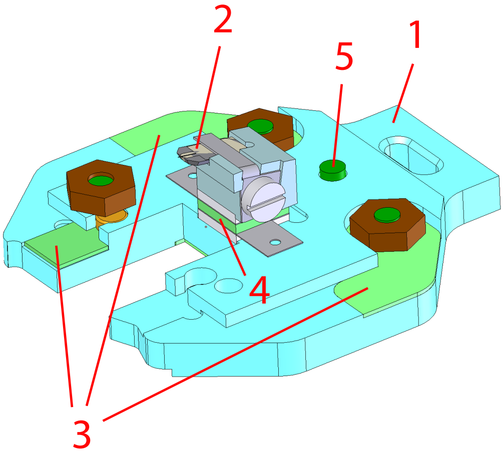

Figure 3.8: The cantilever sapphire plate. (1) opening for wobble stick manipulator (2) cantilever (3) molybdenum contacts (4) oscillation piezo (5) fixation screw.

Piezo Tube Scanner: The piezo scanner is a tube actuator of the type EBL2[7]. With a wall thickness of 1 mm, an outer diameter of 10 mm and a length of 20 mm, it maintains sufficient stability during sample exchanges (see section 3.3.3), when radial forces are exerted.

---

[7] EBL products - www.eblproducts.com

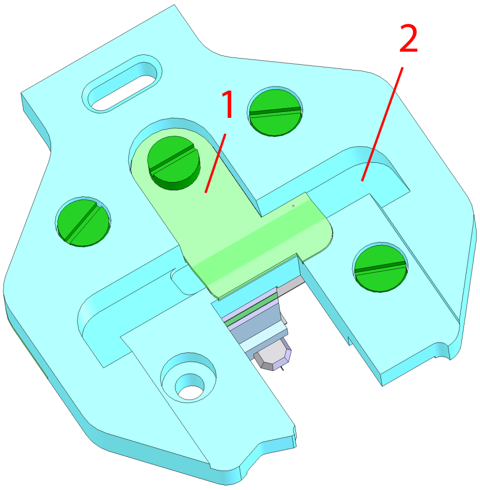

Figure 3.9: Bottom view of the cantilever sapphire plate with (1) molybdenum bottom contact and (2) groove for the clamping spring lever.

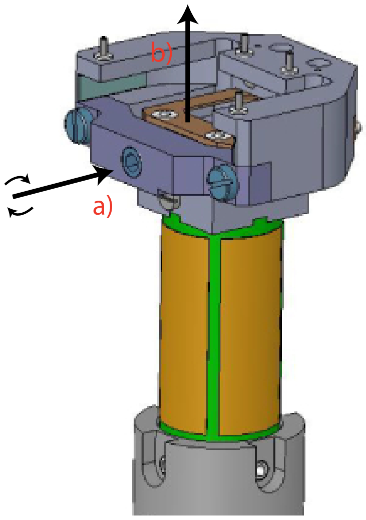

Figure 3.10: The empty sample holder receiver, which is mounted to the top of the piezo tube scanner. The fixation of the sample holder can be activated by (a) the screw that pushes (b) the clamping spring in the vertical direction.

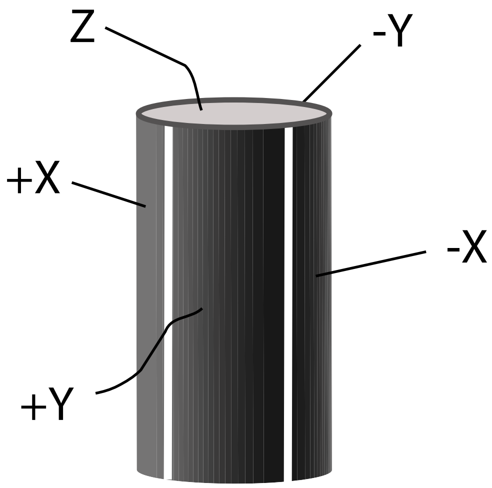

Figure 3.11: This schematic sketch of the piezo tube scanner depicts the XY electrodes. The voltage on the Z electrode is applied with respect to the common ground of the XY channels of the high voltage amplifier.

3.4 Characterization of the Microscope

3.4.1 Vibrational Damping

To keep the tip sample gap stable enough so that atomic resolution can be obtained, several methods were employed in the LT-SPM system. Mechanical noise originating from the building, roughing pumps, turbo molecular pumps and other acoustical noise sources must be isolated from the SFM. There are three distinct vibration isolation systems:

- First of all, building vibrations can be reduced to some extend by installing the laboratory in the basement. The vibrations of the laboratory building at Empa[8] are between 8Hz and 12Hz[9]. More effective are passive or active floating tables. The LT-SPM system sits on four passive floating air legs with a resonance frequency of 1Hz and a quality factor of 2.

- Second, the microscope is attached to the LHe tank with three long and soft springs so that a resonance frequency of 2Hz is obtained. An eddy current damping system reduces the quality factor to 6 at LHe temperatures.

- Third, great care was done to built the microscope as rigid and solid as possible. The purpose is to obtain a higher resonance frequency of the instrument, decouple the tip-sample gap effectively from external vibrations and allow rapid scanning.

If the assumption is made that the mechanical vibration is a damped harmonic oscillator described by the Lorentzian function, then the vibrational amplitude as a function of frequency Ω can be expressed as,

$$A(\Omega) \approx \frac{1}{\sqrt{1 - \frac{2\Omega^2}{\omega_0^2} + \frac{\Omega^4}{\omega_0^4} + \frac{\Omega^2}{Q^2\omega_0^2}}} \tag{3.4.1}$$

where the resonance frequency is termed as ω_0 and Q is the quality factor of the unit. The two vibration isolation stages and the microscope have each a particular frequency response that can be represented by an overall transfer function. The sinusoidal floor displacement is equal to $A_{floor} sin\omega t$ [93, 94].

---

[8] Swiss Federal Institute for Materials Science and Technology

[9] Vibration measurements done at Empa Dübendorf

The individual transfer functions are expressed below as (a), (b, (c) and summarized in figure 3.13, whereas a simplified sketch of the vibrational assembly is shown in figure 3.12.

(a) The transfer function that describes the vibration isolator (floating table and suspension springs) versus the floor is shown in figure 3.13 as α and β.

$$T_1(\Omega) = \frac{A_{floor}}{A_{isolator}}$$

(b) The transfer function that defines the microscope assembly versus the vibration isolator is plotted in figure 3.13 as γ.

$$T_2(\Omega) = \frac{A_{SPM} - A_{isolator}}{A_{isolator}}$$

(c) The overall transfer function is the product of the T_1 and T_2 ($\delta = \alpha\beta\gamma$),

$$T_1(\Omega)T_2(\Omega) = \frac{A_{SPM} - A_{isolator}}{A_{floor}}$$

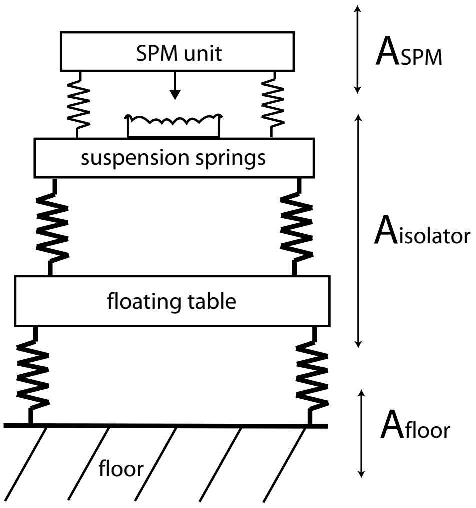

Figure 3.12: A basic schematic of the SPM unit and the double vibration isolation stages, which includes the suspension springs and the floating table. The vertical displacement are labeled for each stage.

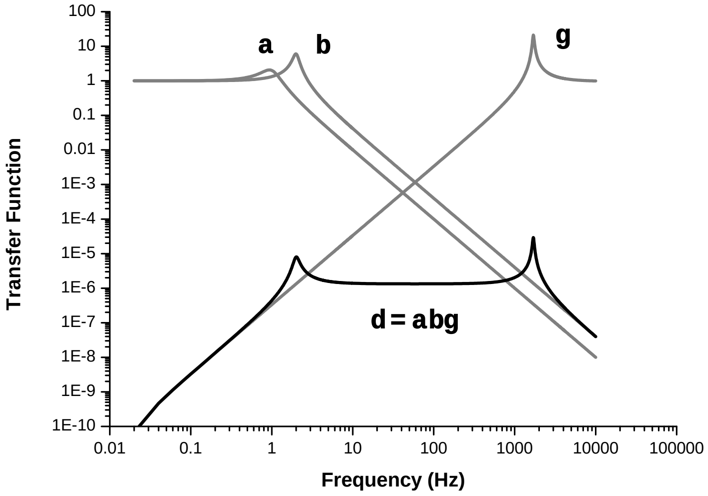

Figure 3.13: Vibration attenuation for the LT-SPM with a two stage isolation system: the distance between the mechanical frequencies of the damping system (α=1Hz, Q1=2 and β=2Hz, Q2=6) and the SPM (γ=1900Hz, Q3=22) should be made as large as possible so that a flat response of the amplitude transfer can be obtained.

The resonance frequencies of the two stage system (floating table and the suspension springs) and that of the SFM itself must be separated as far as possible from each other [93]. The product δ of the individual amplitude transfer functions (α, β, γ), describes a flat response between 40Hz and 1200Hz. If for example, the floor vibration (100Hz) of 1 μm peak-peak is generated, then according to the estimated amplitude transfer graph in figure 3.13, a tip-sample gap vibration of 1pm peak-peak is induced.

3.4.2 Cool-Down of the Microscope

Cooling down the SFM from room temperature to 4.5K is performed in two steps. The advantages of precooling with LN2 from RT to 77K are:

- LN2 is much cheaper[10] and therefore will save LHe.
- LN2 has about 60 times the latent heat of evaporation than that of LHe [95].

---

[10] 1 liter of LN2 costs 0.30 sFr, whereas the price of LHe is 17.- sFr per liter at the time this work was composed.

- 77K the heat capacity of the materials in the microscope is considerably reduced.

The rate of cooling must be conveniently high for practical purposes, but sufficiently slow to avoid thermal-induced stress in the instrument. The first few hours, the cooling slope is steep because of the large temperature gradient. To achieve a rapid cool down, good thermal conductance between the microscope and LHe tank of the cryostat must be ensured. This is obtained by pulling the microscope in its looked position (see figure 3.5) so that the copper cone firmly touches its counterpart of the shield. As depicted in figure 3.14, a rate of 0.9 K/min is reached between 280K and 172K. The loss of cooling power observed at about 140K (marked by left arrow in figure 3.14) could be traced back to a loss of contact between the cone and its counterpart of the shield. This may be caused by differential the thermal expansion of the cooled parts and the pulley system. Under such circumstances, the cool down rate is reduced to 0.04 K/m. The cooling rate increases to 0.5 K/min once the cone is pulled down again, indicated by the arrow on the right hand side. A cool down time of approximately 10 hours with LN2 can be expected, if the assumption is made without the cone contact loss. With the loose cone contact, cooling can take up to 24 hours. To solve this problem, an option to attach a weight to a linear drive feedthrough of the pull down mechanism is under consideration.

The second phase in the cooling procedure is done with LHe. LN2 is removed from the inner tank with pressurized and warm nitrogen gas. A steady flow of helium gas ensures that neither water ice nor nitrogen ice can be formed, when the cryostat bottom is expose to air. Ice is a good insulator and could prevent the microscope from reaching its final temperature in a shortest possible time frame. The thicker the ice layer, the slower the cooling process becomes. Once the temperature of the inner tank is one or two degrees above the melting point of nitrogen, cooling with LHe could begin. Figure 3.15 illustrates the cooling starting from 78K. The measured final temperature of 4.5K is reached after 5 hours.

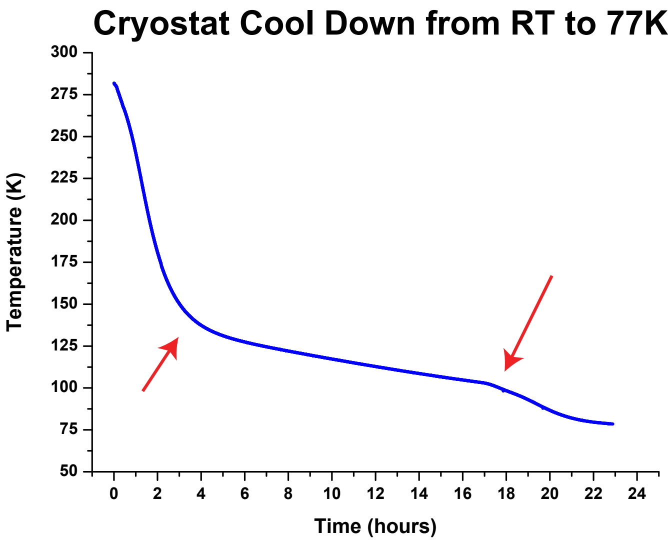

Figure 3.14: The cool down of the microscope from RT to 77K with LN2 takes almost 24 hours.

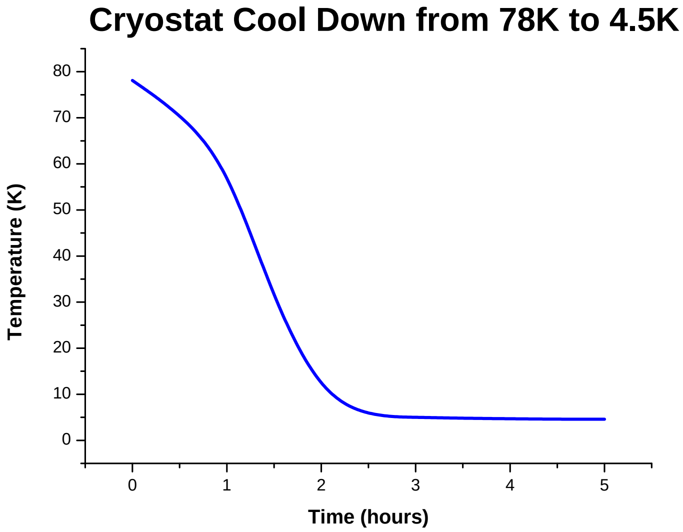

Figure 3.15: The cool down of the microscope from 78K to 4.5K with LHe takes less than 5 hours.

3.4.3 Calibration of the Scanner Piezo

For the scanner piezo calibration, we uses data from atomically resolved images. The calibration of the scanner piezo is performed at 300K, 77K and 4.5K on a Si(111)7x7 surface. The dimensions of a Si(111)7x7 unit cell are known from literature [96, 97]. According to the dimer-adatom-stacking-fault (DAS) model [98], the adatoms and the corner holes are the most prominent features visible in SPM (see figure 3.16). The diagonals of the rhombohedral Si(111)7x7 unit cell are 4.6±0.1 nm (long) and 2.9±0.4 nm (short) [96]. Therefore, the piezo constants for the XY-directions are adjusted to fit these length scales (see figure 3.16).

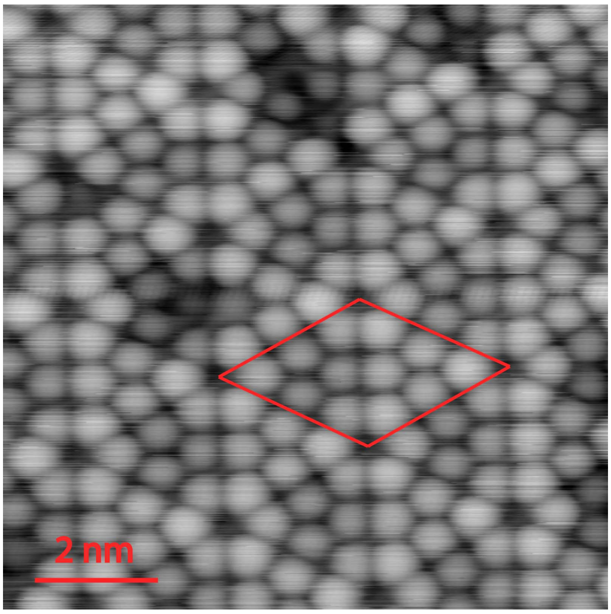

Figure 3.16: This 10x10nm STM image shows the unit cells of a reconstructed Si(111)7x7 at 77K. The diagonals of the unit cell are 4.6nm and 2.9nm long. These values are used to calibrate the scanner piezo in the lateral directions. Additional features such as defects and corner holes are exploited to determine the lateral thermal drift rates at different operating temperatures.

Similarly, an atomic step can be used to calibrate the piezo scanner in the Z-direction. From the atomically resolved image with an atomic step depicted in figure 3.17(a), the step height profile was generated. What appears to be a double step, turned out to be an artifact from a double tip. This textbook image of a double tip shows a narrow and equidistant terrace, which follows exactly the step contour of the actual step. Then, the line profile data was used to adapt the piezo constant, fitting the Z-direction scale. Figure 3.17(b) reveals the calibrated height of an atomic step on the reconstructed surface of Si(111)7x7 to be 310 pm, that is in good agreement with the expected step height of 313pm from literature [99]. Alternatively, the absolute Z calibration can be done with the interferometer. There is a description in section 5.2.3.

Expected travel ranges in XYZ are calculated and listed in table 3.1, where the extension in the axial Z-direction is governed by:

$$\Delta L \approx \frac{d_{31} U L_0}{t} \tag{3.4.2}$$

d_{31} is the piezoelectric strain coefficient of EBL2 in the axial direction, U is the applied voltage, t the wall thickness of the tube and L_0 represents the piezo tube length. The next equation shall give an approximation of the displacements in the lateral XY directions of the piezo tube with segmented electrodes [100, 42].

$$\Delta X \approx \frac{0.9 d_{31} U L_0^2}{t D} \tag{3.4.3}$$

In this case, a voltage is applied to equal and opposite electrodes, where D is the diameter of the piezo tube. The piezoelectric strain coefficient d_{31} for EBL2 in table 3.1 are nominal and are provided by the manufacturer[11].

For comparison, table 3.2 summarizes the calibrated XYZ ranges at three different operating temperatures with the piezo constants in nm/V (0-10V). The discrepancy of a factor four between the expected and calibrated piezo constants can be due to the production tolerances (up to 20%) of the piezo tube scanner and the given piezoelectric strain coefficient d_{31}. The extra load that is attached to the scanner may have a minor impact. From experience, the maximal XYZ travel ranges declined by a factor of two between room and liquid nitrogen temperatures, whereas a factor of five between room and liquid helium temperatures was determined.

---

[11] EBL Products Inc. - www.eblproducts.com

Temperature	d_{31} (Å/V)	Direction	Piezo Constant (nm/V)	Range (±μm)
293K	-1.73	X	62.2	7.972
		Y	62.2	7.972
		Z	17.3	2.214
77K	-0.8	X	28.8	3.686
		Y	28.8	3.686
		Z	8.0	1.024
4.2K	-0.31	X	5.58	0.714
		Y	5.58	0.714
		Z	3.1	0.397

Table 3.1: These values are calculated maximal XYZ travel ranges of the piezo tube scanner at three different temperatures. The piezoelectric strain coefficient d_{31} for EBL 2 is given for convenience [42].

Temperature	Direction	Piezo Constant (nm/V)	Maximal Range (±μm)
RT	X	15.6	1.997
	Y	15.6	1.997
	Z	2.55	0.326
77K	X	7.8	0.998
	Y	7.8	0.998
	Z	*.*	*.***
8K	X	3.12	0.399
	Y	3.12	0.399
	Z	0.51	0.065

Table 3.2: The calibrated XYZ maximal travel ranges of the piezo tube scanner with ±10V input and high voltage amplifier gain of 12.8 and at various temperatures. The Z values at 77K is not available because no step height calibration was performed.

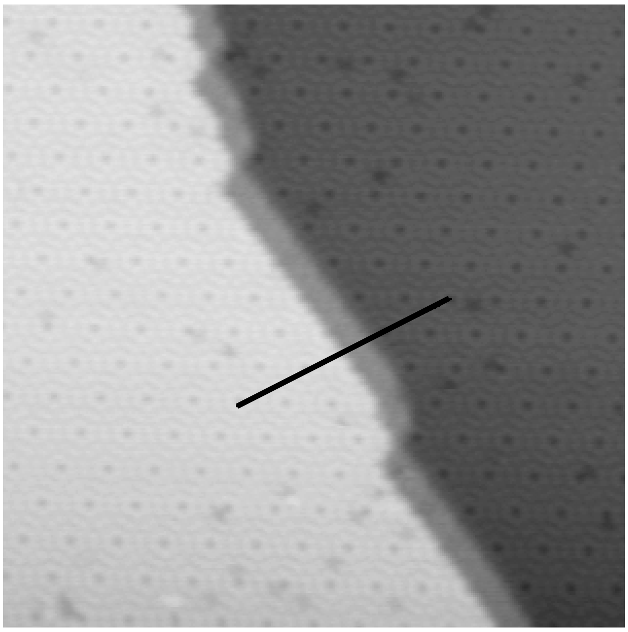

(a) Topographic image with a monoatomic step

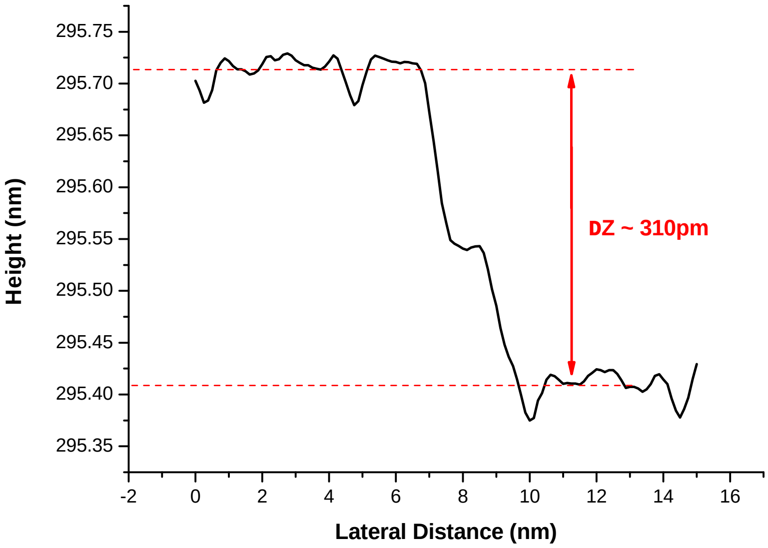

(b) Step height profile of the image

Figure 3.17: Atomic step height: (a) a 50x50nm topographic scan of Si(111)7x7 imaged with a double tip. (b) The line profile shows the calibrated step height.

3.4.4 Thermal Drift

Low temperature SPM and high resolution experiments at the atomic scale require very stable operating conditions over a long period of time. Thus, thermal drift cannot be neglected and must be investigated.

Thermal drift originates from the Brownian motion of atoms of different materials with a thermal gradient, which correlates to their thermal expansion coefficients. Temperature gradients can be avoided by considering the following improvements [66]:

- The symmetric construction of the SFM offers symmetric expansions or contractions of individual parts with respect to one another in the lateral directions. Hence, the actual thermal drift could be kept minimal [90, 91].
- The choice of materials with similar thermal expansion coefficients over a large temperature range additionally reduces drifts.
- The thermal expansion coefficients at LHe temperature are 2-3 orders of magnitude smaller than at room temperature [101]. Consequently, the thermal drift during low temperature operation degreases accordingly.
- Disregarding the settled temperature of the system, thermal drift could be minimized, if the final temperature stays constant. Therefore, optimal thermal stability can be attained by coupling the SFM to a massive cryogenic body.

In table 3.4, the room temperature drift rate was estimated by tracking a predefined reference point on a series of subsequent images over a time period of 53 minutes. The same procedure was repeated to evaluate the drift rates at 77K and 4.5K, which are summarized in table 3.3. These drift rates are extrapolated to nm per hour and show typical values for an optimized low temperature SPM system [102, 89].

Temperatures (K)	Lateral Drift Rate (nm/hr)
300	5
77	0.8
4.5	0.2

Table 3.3: The drift rates in the lateral directions are listed in accordance with the measured sample temperatures.

Room Temperature Images	
No1	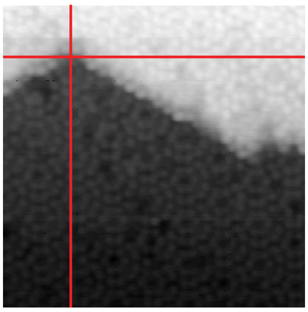
No2	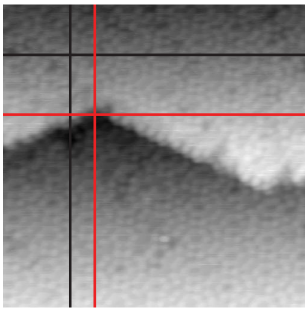
No3	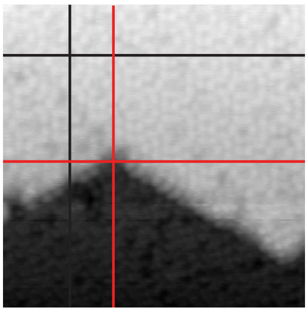
No4	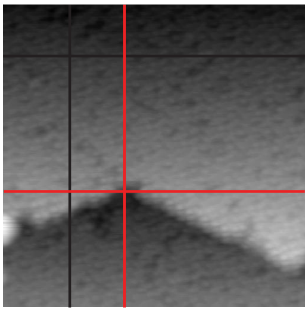

Table 3.4: These raw images were used to determine the drift rate at room temperature. A series of 20x20nm images were taken over a time period of 53 minutes.

Chapter 4

Control Electronics

4.1 Control System

This control system is based on that of the NanoScan[1] *high-resolution magnetic force microscope* hrMFM, which is schematically explained in figure 4.1. The PC handles the user interface, displays the data and also sends stacks of commands to the *real-time controller* (RTC)[2]. The RTC resides in a National Instruments[3] PXI chassis, that also contains a *field programmable gate array* (FPGA) card[4], a *digital inputs/outputs* (DIO) card[5] with digital in/outputs, 8 analog inputs and 8 analog outputs. The DIO card is connected to the piezo motor controller (PMC) unit, which generates signals to drive the piezo positioners. These positioners are required to adjust the sample and optics relative to the spatially fixed cantilever. The DIO card is linked to a high-frequency DAC/ADC[6] box that drives the cantilever oscillation and reads the corresponding signal from the deflection detector. The analog in/outputs are connected to a *break out box* (BOB) and adapt the 0-5V signal of the converters on the FPGA card to a ±10V range and reduces the bandwidth to 5kHz. This BOB drives the *high voltage amplifiers* (HVA) for the scanner piezo and reads the signals from the deflection detector.

---

[1] NanoScan Ltd - www.nanoscan.ch

[2] PXI-8187RT

[3] National Instruments Corporation - www.ni.com

[4] PXI-7831R

[5] PXI-6503

[6] *digital analog converter* (DAC) and *analog digital converter* (ADC)

For this thesis, the NanoScan control system was further developed, partially in collaboration with NanoScan to fulfill the requirements for the LT-SPM, which allows simultaneous nc-AFM/STM operation and dynamic AFM measurement modes with ultrasmall oscillation amplitudes. Figure 4.2 summarizes the current status of the control system hardware[7]. Major improvements were achieved concerning the PLL. The mixing of the deflection signal with the I and Q oscillating signals[8] is now performed on an *analog lock-in* (ALI) card with software controllable offsets, gains and low pass filters. The I and Q signals and the cantilever excitation signal are generated by three fast DAC's, also contained on the lock in card from corresponding digital FPGA output lines. The DAC-ALI card also contains a narrow band self excitation circuitry (see section 4.2.4). In addition, the following minor improvements were made: The external piezo motor controller and the BOB are replaced by NanoScan's embedded PMC2 card and *break out card* (BOC) residing inside the PXI rack. The signal from the interferometer is split into a DC (0-10kHz) and AC (10kHz-10MHz) component.

---

[7] Note that during this thesis different intermediate electronic configurations were used.

[8] A comprehensive review on quadrature FM detection can be found in literature [103, 104].

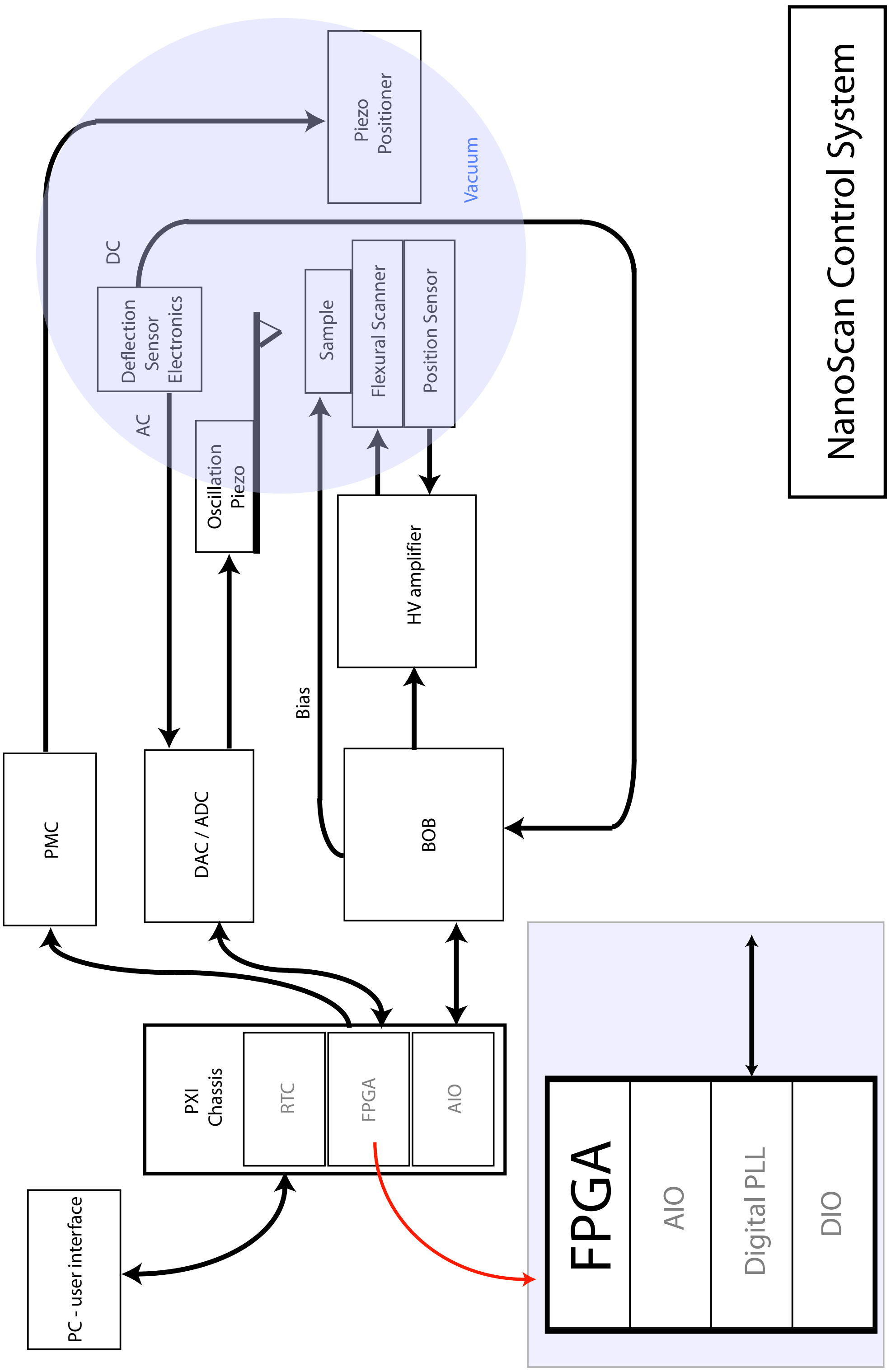

Figure 4.1: The NanoScan control electronics as use in their hrMFM.

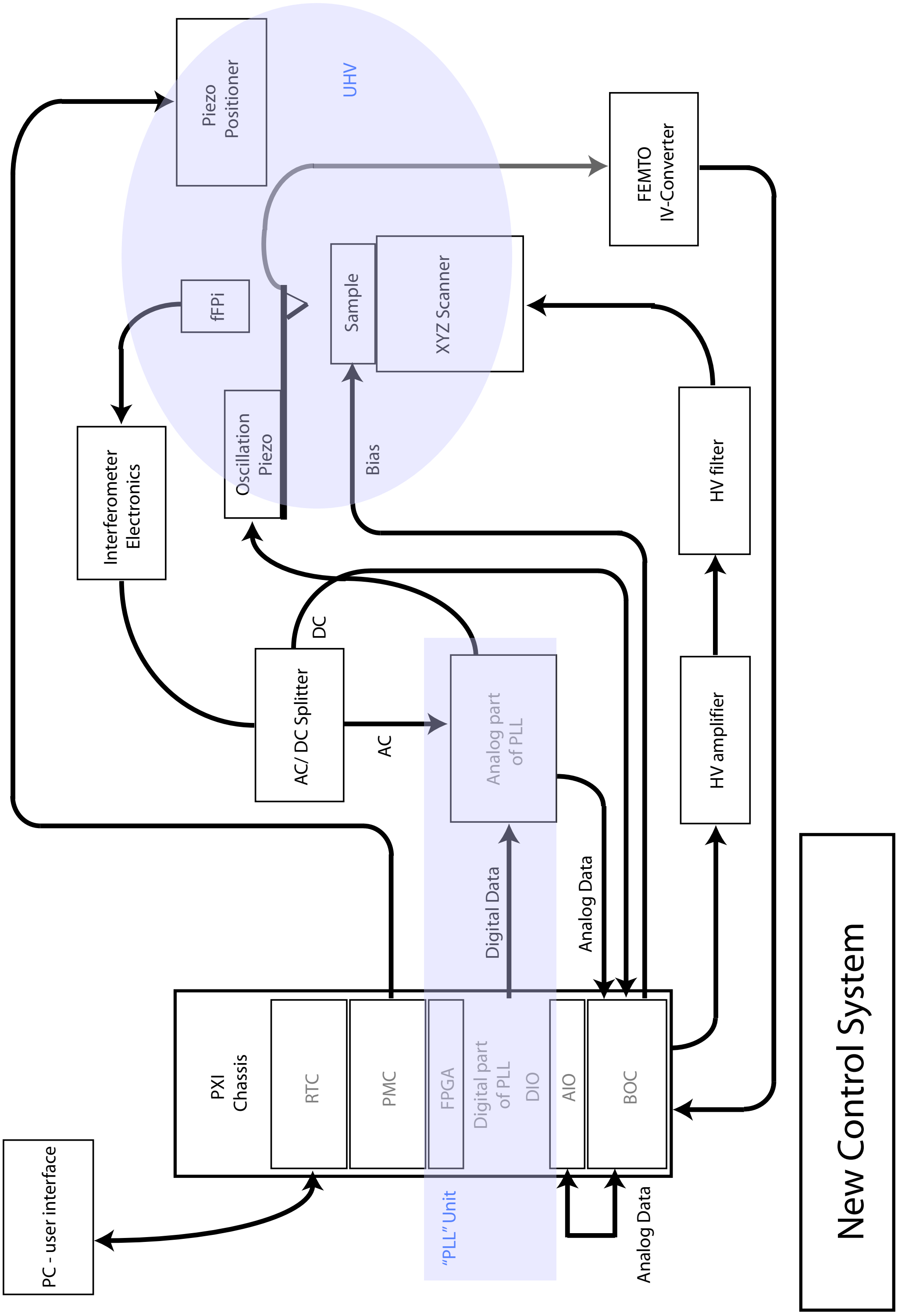

Figure 4.2: The new control electronics as used in this project.

4.2 Cantilever Excitation Schemes

In our system, the frequency shift is always measured with a *phase locked loop* (PLL). For the excitation, two schemes are implemented. The cantilever is either driven by the digitally controlled oscillator (DCO) of the PLL or by the narrow band self excitation circuit. The latter is a new development shown in section 4.2.4.

4.2.1 PLL-excitation

The first scheme uses the PLL to excite the cantilever on its resonance, depicted in figure 4.3. A frequency generator, either a voltage (VCO) or digitally (DCO) controlled oscillator is adjusted to match the free resonance frequency of the cantilever [105]. Then the phase between the drive signal and that from the deflection detector is measured.

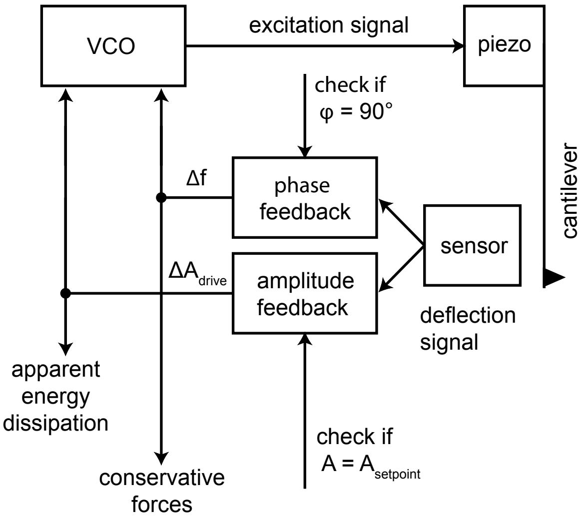

Figure 4.3: Principle of the phase-locked loop (PLL) as used for nc-AFM.

On resonance, this phase is assumed to be 90°. Any deviation from this ideal value of a driven harmonic oscillator arises from additional phase loss in the circuitry. Such additional, electronic-induced phase losses are corrected when the cantilever is still freely oscillating far away from the sample surface, that is without a tip-sample interaction. A tip-sample interaction induced shift of the cantilever resonance frequency changes the phase away from 90°.

A feedback circuit detects and minimizes this phase shift by adjusting the frequency of the cantilever drive signal. In case of a VCO the drive signal frequency is controlled by a voltage. With a DCO, drive signal frequency and amplitude is digitally controlled. In both cases the control signal[9] is a measurement of the frequency shift. In addition, the oscillation amplitude of the cantilever is kept constant by means of another feedback loop that adjusts the drive amplitude. Note that in the improved control electronics developed in this thesis, the phase and amplitude are digitally calculated from the X and Y signal (R and ϕ) output of the analog lock in (ALI) card.

4.2.2 Self-excitation

In the second scheme, the cantilever is driven by the amplified signal that is 90° phase shifted from the cantilever deflection detector (see figure 4.4). The appropriate phase shift depends on the total additional phase loss in the circuitry. However, in a driven harmonic oscillation configuration, the phase shift between the drive and oscillation signal should not deviate too far from 90°. The actual phase shift is typically adjusted to obtain a drive amplitude for the free oscillating cantilever[10]. Once adjusted, it is kept fixed. An am-

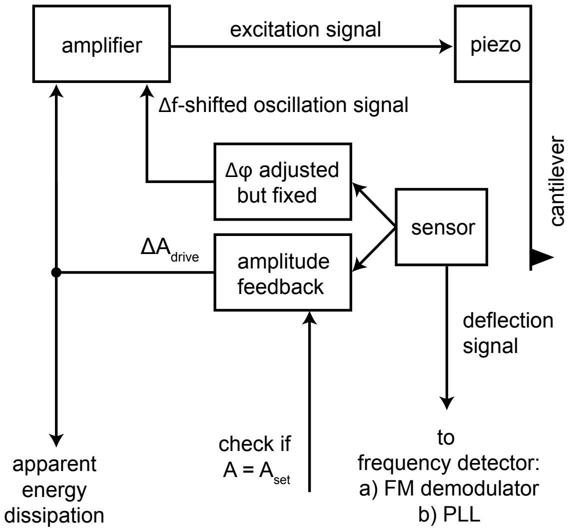

Figure 4.4: The conventional wide-band setup of the self-excitation circuit (SE).

---

[9] A voltage or a digital number

[10] The tip does not interact with the surface.

plitude feedback controls the amplitude of the drive signal. The excitation voltage for the drive amplitude varies to keep the oscillation amplitude constant or as close to the amplitude setpoint value as possible. An increased drive signal in addition to the nominal signal that drives the free cantilever when it is far away from the surface, indicates that an tip-sample interaction induced a change of the cantilever's quality factor. It could also mean that the loss of energy from the oscillating cantilever dissipates into the tip-sample system. This induced change or loss is reflected by the shift of the cantilever's resonance frequency and can be measured with a frequency detector. This can be done either with a frequency demodulator detector[11], or with a PLL. It should be noted that in many systems the frequency shift is measured with a PLL, but the cantilever excitation is achieved with a self-excitation circuit.

4.2.3 Amplitude Control

To feedback control the cantilever oscillation amplitude, the instant oscillation amplitude must be measured. In the present control electronics, there are two implemented techniques available to determine the cantilever oscillation amplitude. The first technique measures the amplitude with the PLL. This requires that the PLL feedback control loop is activated (locked in), tracking the resonance frequency of the cantilever. The magnitude of the amplitude $A = \sqrt{X^2 + Y^2}$ is calculated in the real-time computer, where the X and Y (R and ϕ) are measured in the analog part of the PLL electronics (figure 4.2). X and Y are also called the I (in phase) and Q (out of phase) signals. A profound explanation on the quadrature FM detection theory can be found in literature [103, 104].

The second amplitude measurement technique involves no PLL to track the actual cantilever's resonance. In this particular case, the cantilever oscillation amplitude is measured with an RMS-to-DC converter after the signal has been passed through a narrow band pass filter (see section 4.2.4).

---

[11] Similar to the circuitry in a FM radio

4.2.4 Comparison between PLL and SE

Most groups performing nc-AFM use the more robust self-excitation scheme to drive the cantilever oscillation. The PLL excitation offers a perfect tracking of the resonance frequency, if the phase feedback works at sufficient speed. However, the proper adjustment of the feedback parameters remains a challenge, because the feedback rely on a linear response, whereas the tip-sample interaction response in AFM is highly non-linear. In this respect, the self-excitation scheme is more stable and easier to operate. Advantages and disadvantages of the different operation modes are summarized in table 4.1.

PLL excitation	Self excitation
Difficult to adjust feedback parameters	Straight forward operation
Can unlock, feedback crash leads to tip crash	Stable, cannot unlock, self (re-)start
Can be used to excite fundamental, higher flexural and torsional modes	Usually works on the fundamental resonance only
Tracks the resonance frequency	Phase not perfectly kept at 90°; resonance frequency not properly tracked
Apparent energy dissipation signal occurs only if phase feedback is too slow to track resonance frequency	Apparent energy dissipation signal can occur when the resonance frequency is not properly tracked

Table 4.1: Advantages and drawbacks of the PLL and self-excitation schemes are listed for comparison.

In order to overcome some of the inherent disadvantages of the self-excitation scheme, we implemented a narrow band excitation scheme (figure 4.5). In this setup the measured oscillatory signal is mixed to obtain a intermediate frequency of 455kHz that runs through a narrow band pass ceramic filter. The mixing frequency is generated by a DCO that adds 455kHz to the cantilever frequency. Note that the cantilever frequency can either be fixed to the free resonance frequency of the cantilever or locked to the actual resonance by the PLL. The first is possible if the actual resonance does not deviate more than half of the width of the band pass filter (5kHz) from the free resonance. This is normally fulfilled in nc-AFM. The mixing signal then contains:

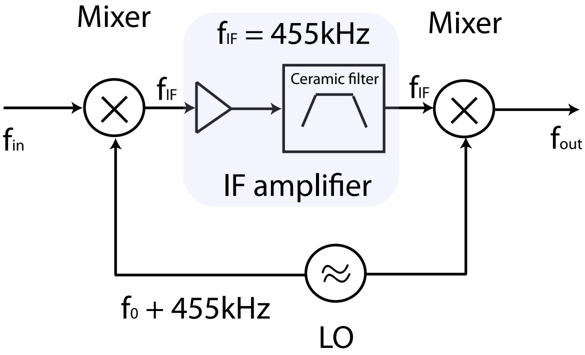

Figure 4.5: The narrow band filter has a bandwidth of 10kHz and allows an exact sharp filtering characteristic of the signal.

$$(f_0 + 455\text{kHz}) \pm f_{in}$$

But only $(f_0 + 455\text{kHz}) - f_{in}$ passes through the bandpass. The second mixer then generates:

$$(f_0 + 455\text{kHz}) - f_{in} \pm (f_0 + 455\text{kHz})$$

and gives two values

1. $f_{out} = f_{in}$
2. $f_{out} = 2f_0 - f_{in} + 910\text{kHz}$

where only the first signal excites the cantilever. The narrow band excitation scheme solely amplifies a frequency band selectable to control the frequency of one specific cantilever oscillation mode. Therefore, excitation on higher modes or torsional modes is now possible in the self-excitation scheme.

4.3 Feedback Control Loops

There are four feedback loop required when performing nc-AFM measurements with a PLL. The following feedback control loops are part of the detection electronics:

- *The interferometer control loop* regulates the Fabry-Perot cavity length by moving the W-piezo, so that the operation point (OP) at the steepest slope (highest sensitivity) of the interference signal is maintained constant.
- *Frequency control loop*: the change of the cantilever resonance frequency is realized with a PLL. This feedback loop changes the frequency and keeps the phase constant[12].
- *Amplitude control loop*: in order to measure the dissipation forces between tip and sample, the amplitude of the cantilever must be regulated to keep it at a constant value.
- *Z scanner control loop*: to keep the tip sample gap constant, a feedback loop is used to control the z position, while scanning across the surface in the lateral directions.

This last control loop mentioned above is the main feedback loop, when operating the instrument in the nc-AFM mode. In this mode, the FM Quadrature Demodulation is used to extract two independent signals (I and Q), which are 90° shifted to one another [103]. The phase and frequency variations during the measurement process must be regulated (see section 4.2.1).

---

[12] As the name suggests, it locks the phase

4.4 Noise Analysis

4.4.1 Noise of STM line

In a typical STM application, the tunneling bias is of the order of 1V and the tunneling current around 1nA. This yields a junction resistance of 1GΩ. Special care must be taken to shield the tunnel current line from noise sources and appropriate grounding must be implemented. The instrument hangs from electrically isolated suspension springs and is grounded to the top of the UHV system to the cryostat. The shield of the input and the ground of the bias are also connected to a common point (figure 4.7). With the variable gain set to 10^9, the output bandwidth of this low noise current amplifier[13] is limited to 1.2kHz. For the noise measurement shown in figure 4.6, the output signal was amplified 100 times with a Tektronix low pass filtered (3kHz) preamplifier. The noise spectra were swept from 20Hz to 1.2kHz with the spectrum analyzer and averaged 10 times. In figure 4.6, the averaged swept spectra are displayed in a semi log graph. The spectral integration reveals a value corresponding to 0.69pA_{rms}.

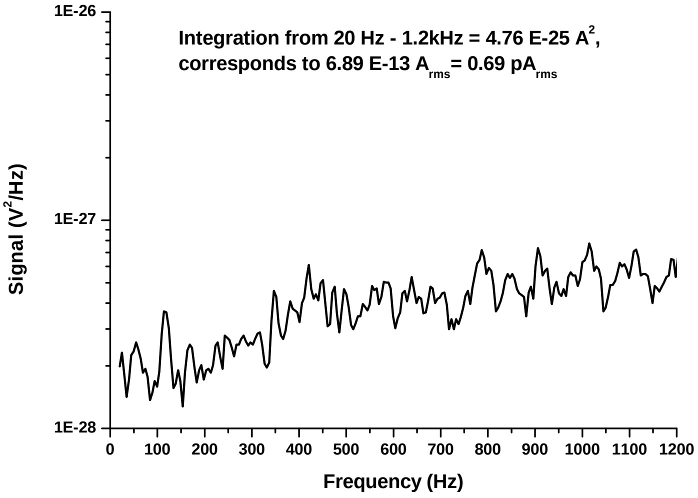

Figure 4.6: This semi log graph shows the spectral noise (V^2/Hz) of the STM line integrated from 20Hz to 1.2kHz.

---

[13] FEMTO DLPCA-200 - www.femto.de

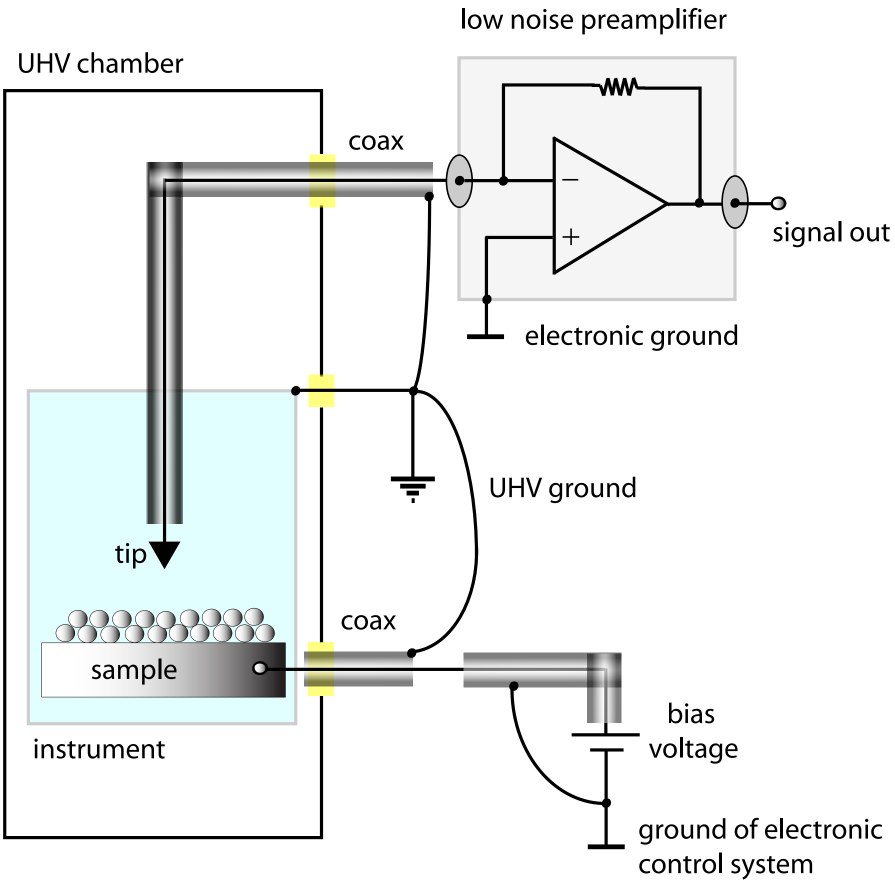

Figure 4.7: Schematic of the low noise preamplifier IV converter with the shielded tunnel and bias lines. The instrument body, the shields of the tunnel and bias lines are joint to a common UHV grounding point. The yellow squares represent floating feedthroughs.

4.4.2 Noise of Scanner Piezo line

The scanner piezo is affected by any electrical noise, originating from each device that is connected to it. This noise determines the tip-sample gap stability. In order to conclude the noise figure in the lateral and the vertical directions, noise data at three different devices were recorded. In figure 4.8, the electronic block diagram shows the three positions labeled as A, B and C, where all data were taken with a differential preamplifier[14] and a spectrum analyzer[15].

The analog signal for the scanner piezo is controlled by the PXI unit. The signal is connected to the BOB, where it is low-pass filtered at 5kHz. The first noise data was acquired at the output of the BOB labeled with A. At the output of the high voltage amplifier (labeled with B), the second series of measurements were done. To minimize noise introduced by the high voltage amplifier itself, a high voltage filter was added to the circuit. At this position C, the last sequence of noise data was collected. The noise figures in $V_{peak-peak}$[16] are listed in table 4.2.

Position	X	Y	Z	Max Signal	Bandwidth
A	$110\mu V_{pp}$	$115\mu V_{pp}$	$120\mu V_{pp}$	±10V	5kHz
B	1.85mV_{pp}	1.85mV_{pp}	2.25mV_{pp}	±128V	X, Y: 100Hz, Z: 1kHz
C	1.80mV_{pp}	1.80mV_{pp}	2.20mV_{pp}	±128V	X, Y: 1kHz, Z: 10kHz

Table 4.2: The noise values of the piezo scanner XYZ directions are shown in the order of their acquisition position (A,B and C) as indicated in figure 4.8.

---

[14] Tektronix AM502

[15] Hewlett-Packard 3588

[16] $V_{peak-peak} = 2 \times V_{rms} \times \sqrt{2}$

To get a sense of the vertical fluctuations of the scanner piezo produced by the electrical noise of the filtering and amplifying devices, the Z-noise value at position C (table 4.2) was multiplied with the piezo constant for three temperatures. Table 4.3 shows the noise values of the vertical fluctuation (Z direction) calculated from table 4.2 in picometer peak to peak.

Temperature	Piezo Constant	Electronic Noise	Z-Noise
293K	$5.1nm/V$	$2.2\text{m}V_{pp}$	$11.2pm_{pp}$
77K	$*.*nm/V$	$2.2\text{m}V_{pp}$	$*.*pm_{pp}$
4.5K	$1.0nm/V$	$2.2\text{m}V_{pp}$	$2.2pm_{pp}$

Table 4.3: First column: sample temperature in Kelvin. Second column: piezo constants (nm/V) from table 3.2. Third column: electronic noise of Z-direction from table 4.2. Fourth column: vertical (Z) noise in picometer (peak-peak) calculated from the electronic noise value in column three.

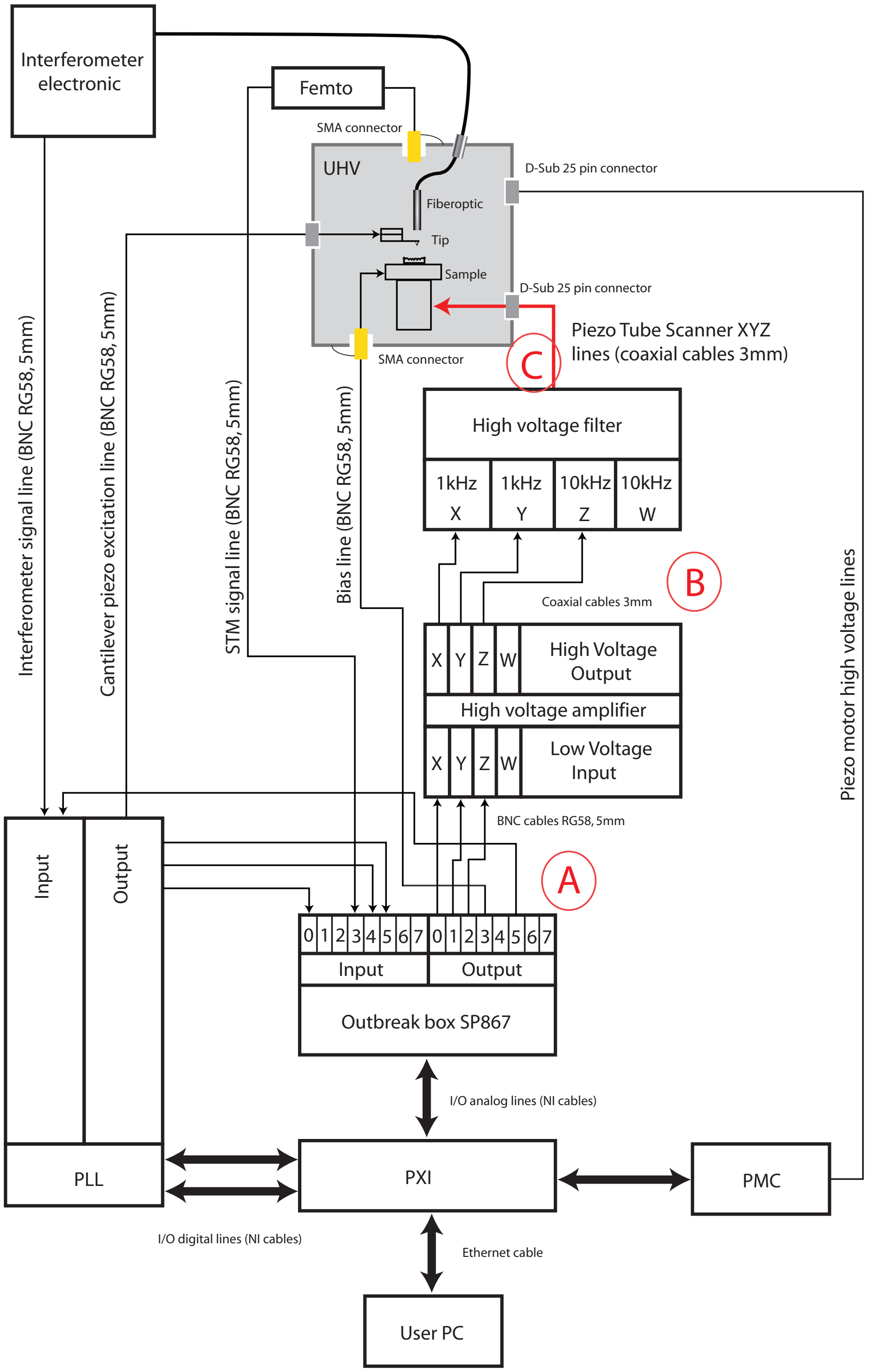

Figure 4.8: General block diagram of the control electronics.

Chapter 5

Fabry-Pérot Interferometer

In the original AFM setup, a tunneling probe was used to measure the cantilever deflection [14]. Since then, alternative deflection detection schemes were developed [25], including optical techniques [81, 78, 106]. Nowadays, most AFM configurations use optical deflection sensors, such as beam deflection sensors or interferometers. Rugar et al presented a fiber optical interferometer that is particularly suited for low temperature instruments, because only the end of a single mode fiber is adjusted with respect to the cantilever in the cryogenic system [107]. All optical and electronic components are located outside the cryogenic environment.

In table 1.1, the thermal amplitudes of conventional cantilevers range between 0.2pm and 14pm. With a bandwidth of 1kHz, the deflection sensitivity needs to be better than 6.3fm/$\sqrt{Hz}$ and 442fm/$\sqrt{Hz}$ respectively.

For ultrasmall cantilevers (width $\approx 4\mu$m) or for the detection of the torsional modes of a conventional cantilever (half width $\approx 15\mu$m), a spot size of $<4\mu$m is required [108].

Ruger et al have reported a detection sensitivity of 55fm/$\sqrt{Hz}$ [107], thus missing the more stringent sensitivity requirement of 6.3fm/$\sqrt{Hz}$ by almost a factor of ten. The sensitivity of an interferometer can be enhanced by implementing a cavity leading to multiple reflections. This can be achieved by coating the fiber end and the cantilever backside to enhance their reflectivity. However, the beam leaving the core of the single mode fiber will spread such that only reflected light falling into the acceptance angle of the fiber contribute to the signal. The distance between the fiber end and the cantilever must be minimized ($<10\mu$m) so that sufficient signal can be obtained [107, 109, 89, 27]. Also the angle between the cantilever and the flat fiber end must be held as parallel as possible. This requires a five dimensional adjustment, that is the XYZ position of the cantilever relative to the fiber and the pitch/roll adjustment. A complicated instrument has been constructed by Oral et al to meet these requirements [27]. The 40fm/$\sqrt{Hz}$ detection sensitivity obtained was only slightly better than that of Rugar et al [107]. Future projects may require cantilevers that are a few μm long. Therefore, optical fibers with a standard width of 125 μm[1] cannot be positioned on top of those small cantilevers because of the support chip. This means that the close cantilever-to-fiber separation will ultimately limit the minimum size of the cantilever.

5.1 Focussing Fabry-Perot Interferometer

In this system, we use a fFPi in UHV and at low temperature as described by Hoogenboom et al [110]. Figure 5.1 shows a schematics of the interferometer. The beamsplitter, the laserdiode with its integrated optical insulator, the reference and the signal photo diode are all integrated in a module custom made by OECA[2]. All optical elements are mounted with non-perpendicular angles relative to the beam path to reduces internal back-reflections. This is to avoid an parasitic interference signal additional to that measured by the optics-cantilever cavity. In spite of these precautions, such an additional interference signal between a beam reflected at the optics and an internally reflected beam occurs. This interference depends on the optical length of the interfermeter-to-optics fiber and is sensitive to fiber vibrations and temperature changes. In order to surpress this parasitic interferences, the laser diode current can be modulated with 20MHz to shorten the coherence length [111, 112].

The optics and the cantilever are depicted in figure 5.2. The three lenses image the 5μm core of the single mode fiber to a 3μm spot on the cantilever. The image distance has been made identical to the 0.9mm radius of curvature of the 90° reflecting lens surface, so that multiple reflections is enabled.

In the work of Hoogenboom et al, the tolerance of the interferometer to angular misalignment was tested [110]. The appearance of the $\lambda/4$ peak and the reduced signal intensity of the $\lambda/2$ peaks was attributed to the limited acceptance angle of the fiber core for the beam reflected light (see figure 5.3). Furthermore, we have tested the performance of our interferometer in UHV at room temperature, 77K and 4.5K. The interference signals at these temperatures are depicted in table 5.1. At low temperatures, a $\lambda/4$ peak appears and intensity is lost in the $\lambda/2$ peaks. Further, a distinct asymmetry of the peaks is notable. The first observations can not be attributed to a temperature-induced change of the cantilever angle, because it would have to be $> 10°$

---

[1] The core diameter is about 5 μm.

[2] www.oeca.de

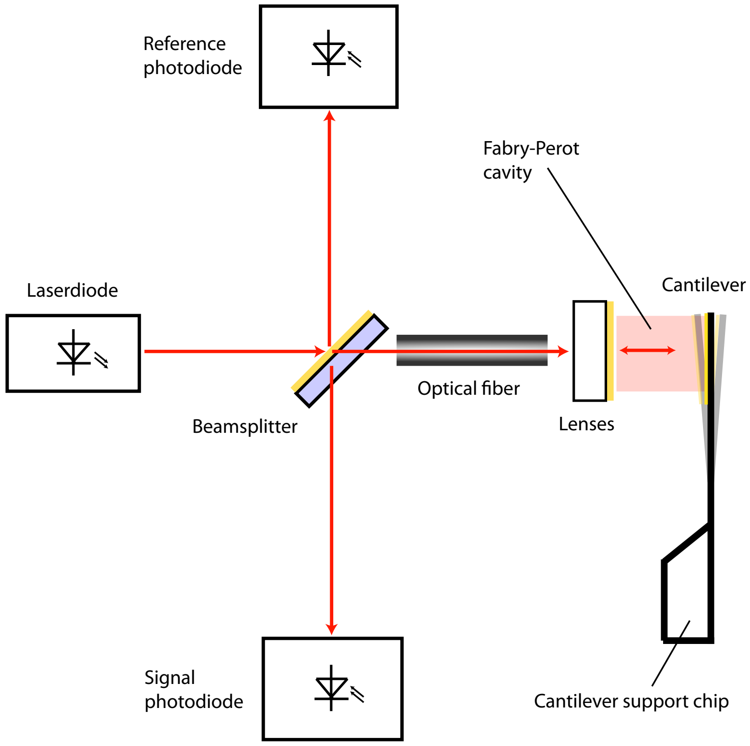

Figure 5.1: The conceptual model of a FPi.

to explain the $\lambda/4$ peak. Instead we suggest that a temperature-induced misalignment of the lenses may cause the effect (see section 5.2.1).
The second observation (peak asymmetry) is attributed to thermal-induced effect that break the time-reversal symmetry of the interference pattern measurement shown in chapter 7.
In spite of these difficulties a thermal spectrum taken on a 45kHz (40N/m) cantilever demonstrates the excellent sensitivity of our fFPi (see section 5.2.2). A value of 4fm/$\sqrt{\text{Hz}}$ was obtained above 200kHz. This is below the 6fm/$\sqrt{\text{Hz}}$ required for a 2000N/m cantilever at 4.5K (see table 1.1).
Better noise limits can be obtained if the optical power would be improved beyond P_{in}=90μW used in our case.

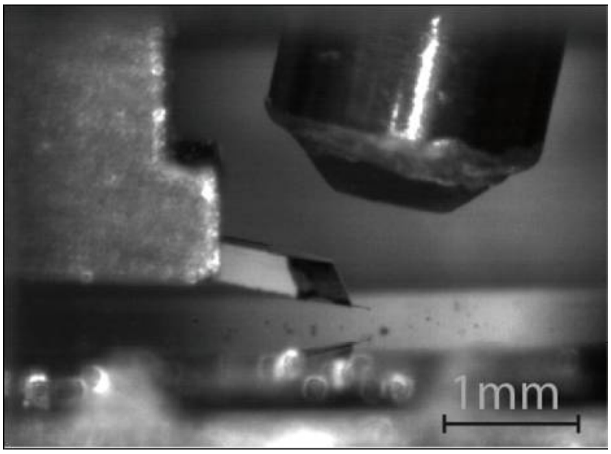

Figure 5.2: The large optics-cantilever distance enables straightforward laser adjustment within ten minutes. The cantilever tip and its reflection on the sample surface are visible. The interference pattern is generated by moving the optics up and down in a sinusoidal manner.

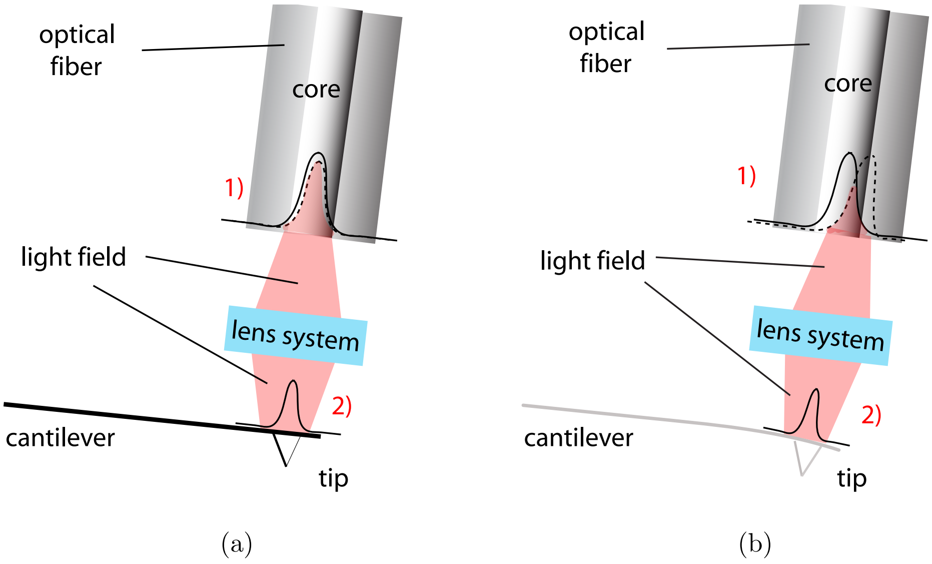

Figure 5.3: (1) The light intensity is represented by the solid Gaussian curve, whereas the dashed curve is the reflected light going back into the fiber core. (2) The light intensity reflected at the cantilever's backside. (a) The angular alignment of the lens system is perpendicular to the optical axis (0°). (b) If the angular alignment of the lens system is larger than 11° then the light field is distorted and a smaller fraction of the reflected light enters the fiber core.

5.2 Interferometer Characterization

The lens system in this Fabry Perot interferometer has a fixed focal length of 0.9mm. This eases the "optics to cantilever" alignment to a great extend and can be done within minutes, with the noise level measured to be $\approx 4\mathrm{fm}\sqrt{Hz}$. With a laser spot size of 3 μm, simultaneous monitoring of vertical/ lateral forces and flexural/ torsional modes of conventional cantilevers can be performed. For low temperature operations, the instrument is built according to a symmetric and compact design so that misalignment of the interferometer can be prevented because of thermal contraction during temperature variations [113, 89, 66].

5.2.1 Temperature Behavior

The lens system consists of 3 lenses. This confocal lens configuration has a fixed focal length and collects the reflected light coming from the cantilever's gold coated backside (see figure 5.4). Table 5.1 shows the interference pattern at 3 different operating temperatures. At first glance, the spectral length $\lambda/2$ can be recognized as the length between the minima. At a closer look, a smaller, distorted minimum peak can be sighted at $\lambda/4$. This intermediate peak is also observable at the lower temperatures, and even more pronounced. Due to the temperature changes, the lenses contract and drift off their relative positional configuration with respect to the fiber. Therefore, a derailed lens arrangement at lower temperatures may lead to a tilt of the optical axis and change the ideal acceptance angle into an object of more complex geometrical shape (see figure 5.5). According to Hoogenboom's observations [110], mirror angles larger than the acceptance angle may contribute to interference patterns with destructive interference peaks occurring every $\lambda/4$. Fortunately, the interference pattern looks identical at every operation temperature after every cool-down and heat-up cycle. Cryogenic operation alters the intensity of the $\lambda/4$ peak, which leads to a changed interference pattern and thus to different interferometer sensitivities.

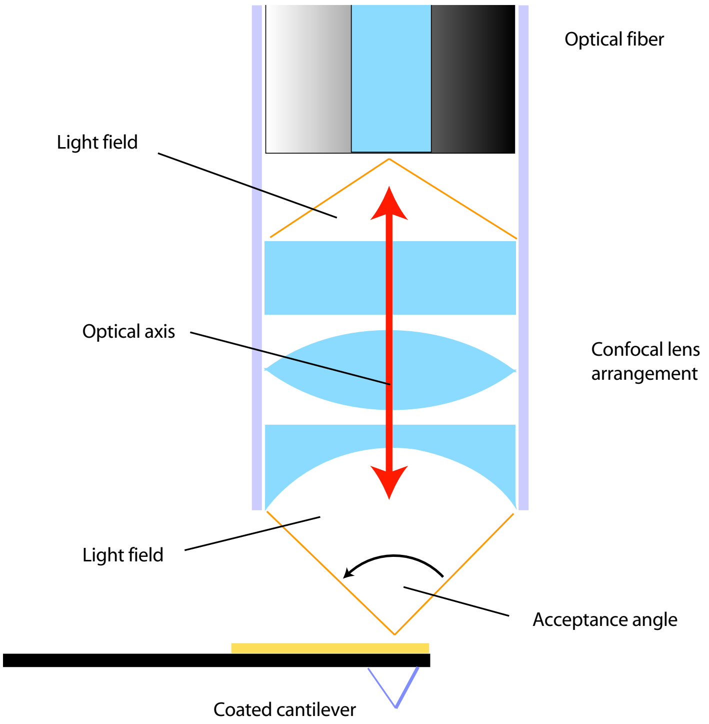

Figure 5.4: At room temperature the confocal lens arrangement of the lens package is well aligned, where the lens system is perpendicular to the optical axis. This results to a defined acceptance angle and a fixed focal length. This graph is not to scale.

Temperatures	Interference Patterns
RT	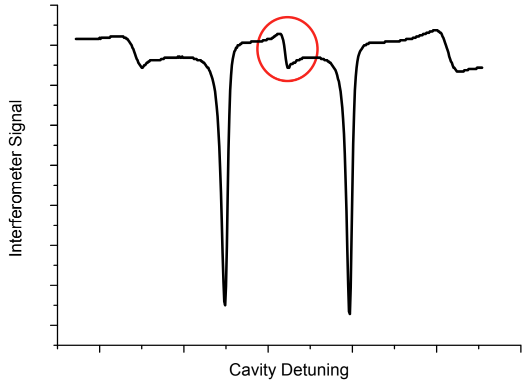
77K	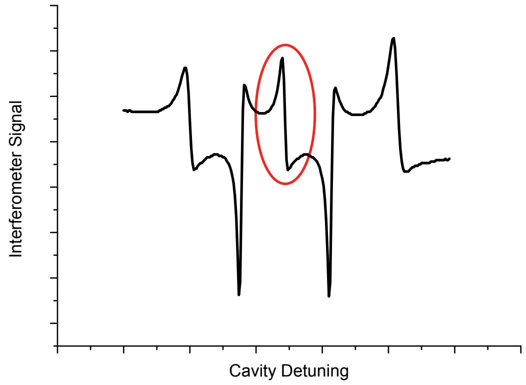
4K	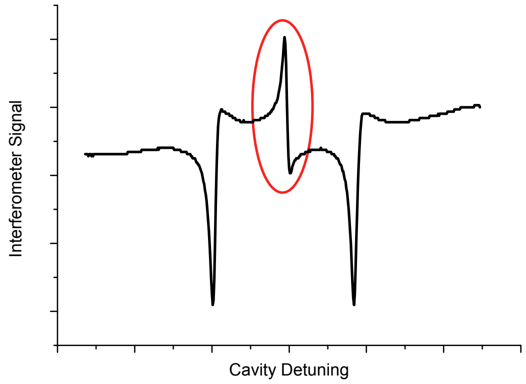

Table 5.1: These graphs show the variation of the $\lambda/4$ peak at three different operation temperatures. This intermediate interference peak gets more pronounced at lower temperatures.

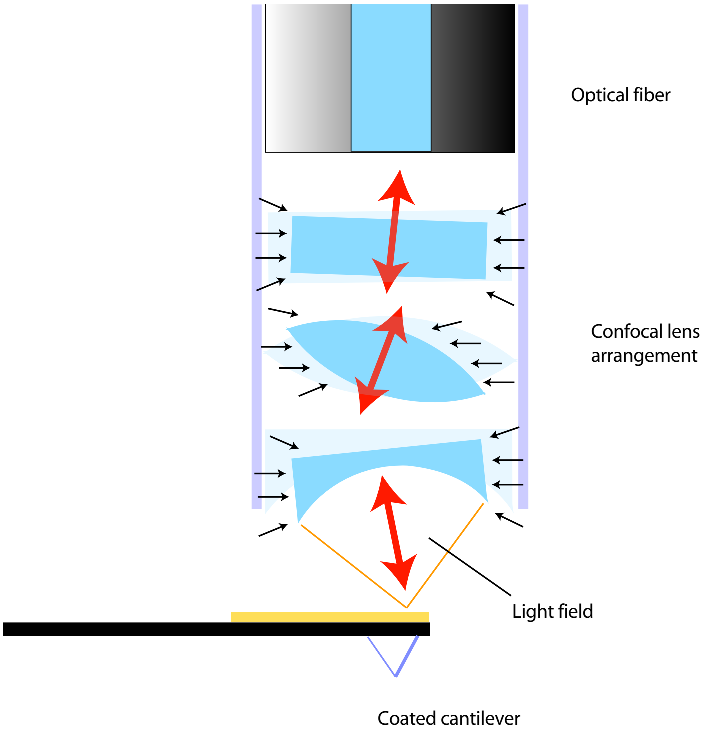

Figure 5.5: At lower temperatures the lens arrangement gets more complex because of the different thermal contractions of the individual parts in the lens system. The acceptance angle changes and contributes to the generation of the additional $\lambda/4$ interference peaks. This graph is not to scale and shows an exaggerated view of the explained situation.

5.2.2 Thermal Noise Limit

A commercial cantilever[3] was used to acquire the thermal noise spectrum shown in figure 5.6. The laser power was set to 790μW, with the calibration adjusted to the stable operation point (OP) which gives the highest sensitivity (see section 5.2.3 for FPi calibration). Besides the cantilever's fundamental resonance at 280kHz, electronic noise peaks at 60kHz and 100kHz can be spotted at first glance. The shot noise limit is estimated to be $\sim$1fm/$\sqrt{Hz}$ at 1MHz with a laser power of $\sim$1mW [110]. However, the thermal noise limit of the cantilever in this system was determined to be 4fm/$\sqrt{Hz}$ at 1MHz. Depending on the configuration of the interferometer, the limitation could be dominated by the thermally driven displacement noise of reflective surfaces, for example mirror substrates [114, 115]. In our case, the thermal noise of the cantilever is the limiting factor. To overcome this cantilever noise level, better interface materials between the reflective coatings and the cantilever's backside should be employed (see chapter 7). Another possibility is to make the cantilever smaller.

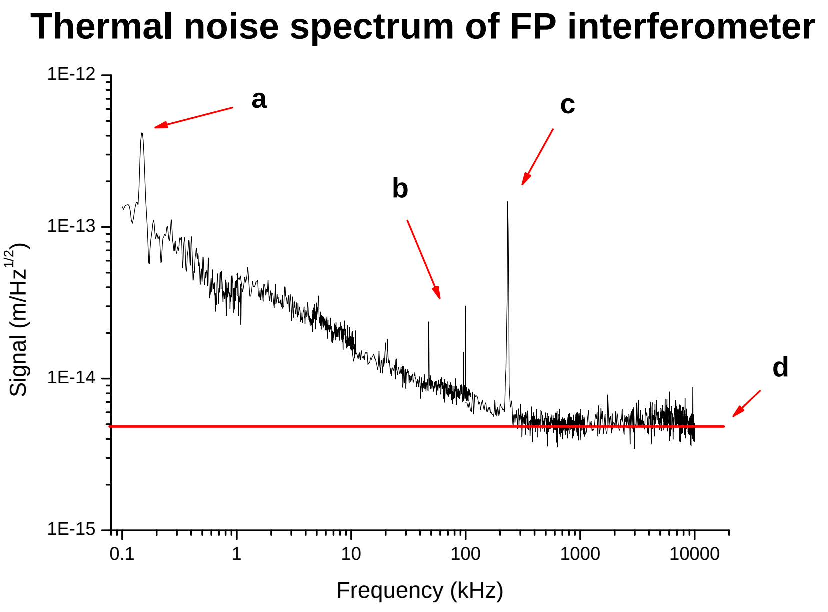

Figure 5.6: The thermal noise spectrum if the FPi shows (a) the 50 Hz noise peak, (b) electronic noise peaks from switching power supplies and (c) the fundamental resonance frequency of the cantilever. (d) The noise level of the FPi at 1 MHz is 4fm$\sqrt{\text{Hz}}$.

---

[3] Silicon lever, 40N/m, f_0=280kHz, backside gold coated at the free end

5.2.3 Calibration

In theory, the calibration of an optical fiber interferometer is straight forward, because the free spectral range[4] is known to be $\lambda/2$. In figure 5.7, a transmission spectrum of a fiber interferometer is shown with two interference peaks. The operation point (OP) is optimally chosen on either side of an interference peak, where the slope is steepest. A steep slope means a large signal for small changes in the cavity length. However, the dynamics behind the cantilever motion affected by the laser-induced forces are complicated. The dynamics include the change in the cantilever's fundamental resonance frequency and the asymmetric distortion of the interference pattern, both caused by the photon pressure and photothermal effects. More details on this asymmetric distortion of the resonance peak can be found in section 7.5.1.

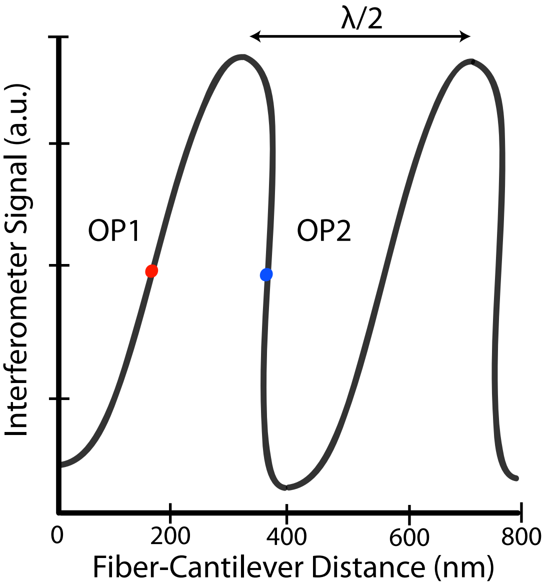

Figure 5.7: Illustration of interference fringes of a normal optical interferometer. The asymmetry of the interferogram is exaggerated to demonstrate the photon-induced effect on the dynamics of the cantilever. Operation point OP1 and OP2 are ideally set at the steepest slope.

If during calibration OP1 is chosen, the cantilever's motion gets unstable and starts to oscillate in an uncontrollable fashion [116, 117, 118, 119]. It is

---

[4] The free spectral range is the distance in wavelength (or frequency) between two consecutive intensity maxima (or minima) of an optical interferometer.

sometimes referred to unstable oscillation or "heating" of the cantilever. On the other hand, strong "cooling" effects can be observed on OP2. Heating and cooling are common but misleading terms, because no actual heating nor cooling of the cantilever occurs. For clarity, let us refer these effects as *amplifying* (OP1) and *damping* (OP2). The reader may be directed to chapter 7, where these laser-induced thermo-mechanical effects are explained in greater details.

In practice, the calibration of the focusing Fabry Perot interferometer is somewhat challenging. As seen in figure 5.8, the interference peaks are sharp and tall, which equates to a steeper slope (V/nm). The black curve is the W-piezo signal that moves the optics in a 5Hz sinusoidal manner so that the interference pattern (red curve) is generated. The W-piezo feedback control loop maintains the operation points at a constant slope. For the calibration procedure, the peaks within the linear region of the W-piezo signal should be used. For example, from figure 5.8 the sensitivity[5] of the W-piezo at LN2 temperature is calculated.

$$W_{sensitivity} = \frac{392nm}{2.24V - (-3.85V)} = 64.37nm/V \tag{5.2.1}$$

The nonlinear regions around the turning points of the W-piezo driving signal are avoided. Ideally, a triangular signal is preferred to drive the optics because it is linear until the turning point. However, the abrupt changes of the W-piezo direction may introduce other unforeseen problems such as mechanical modes, generated by the harmonics of the triangular signal. Efforts to damp these resonant modes are demonstrated by the works of Aphale et al [120]

The absolute calibration of the piezo scanner in the Z-direction can be performed in the same way. This is done without a cantilever. The optics is adjusted to the focal distance of 0.9mm on top of a centered, gold coated sample with a defined tilt angle of 11°. This way a maximal signal to noise ratio can be obtained. However, this Z calibration method does not account for the nonlinearity at the extremities of the piezo scanner range.

---

[5] The inverse of the slope (volts per nanometer)

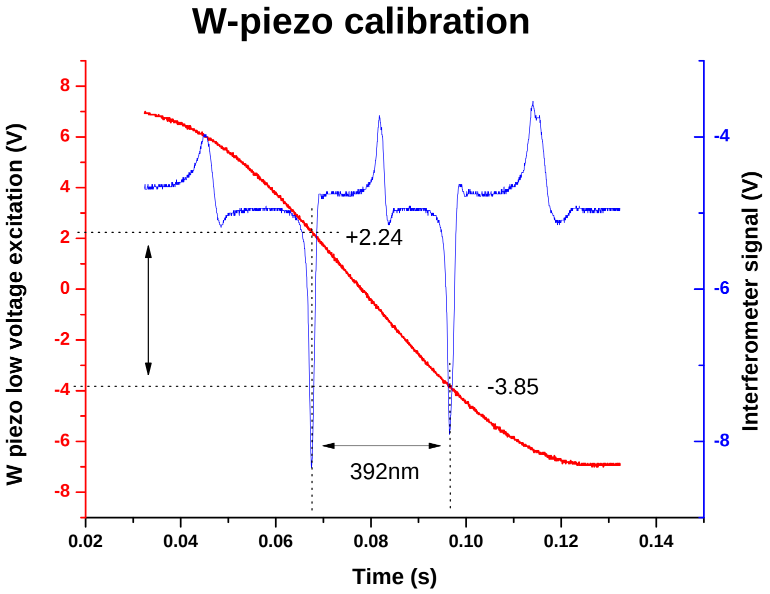

Figure 5.8: W-piezo calibration: the red curve represents the driving voltage that moves the W-piezo in a sinusoidal up-down motion. This again generates the interference signal, which is illustrated as the blue curve.

5.3 Cantilever Photothermal Actuation

An important development performed within this thesis was the implementation of a five lens system to reduce the chromatic abberations of the currently installed three lens configuration (see figure 5.9). While the three lens system is optimized for the 785nm wavelength (laser spot of 3μm), it inherently focusses a 635nm laser to a 75μm wide spot (see figure 5.10(c)). This new optical five lens system is corrected for chromatic abberation, which accommodates two lasers with different wavelengths as illustrated in figure 5.10(d). This allows both lasers to be focussed to the same spot. The second laser will be used for photothermal excitation of the cantilever. Optical excitation[6] was first demonstrated by Umeda et al [33], where a Nickel foil cantilever was excited with an intensity modulated laser. A separate beam deflection setup then detects the cantilever's deflection. Similar results have been achieved by Fukuma et al [31] and Stahl et al [121].
The new five lens system simplifies cantilever actuation at very high frequencies and also the construction of the cantilever holder (see section 3.3.3).

---

[6] Here, actuation and excitation is used interchangeably.

Therefore, piezo actuators are no longer needed as they introduce undesirable mechanical vibrations near the cantilever resonance frequency [105]. Moreover, high temperature thermal annealing of the cantilever can be performed to remove the surface oxide layer and improve the quality factor of force sensors [108].

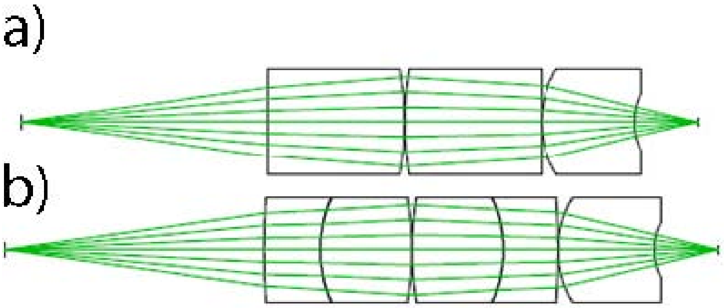

Figure 5.9: Lenses in the optical system. (a) Original three lens system. (b) New five lens system with corrected chromatic abberation for two different wavelengths.

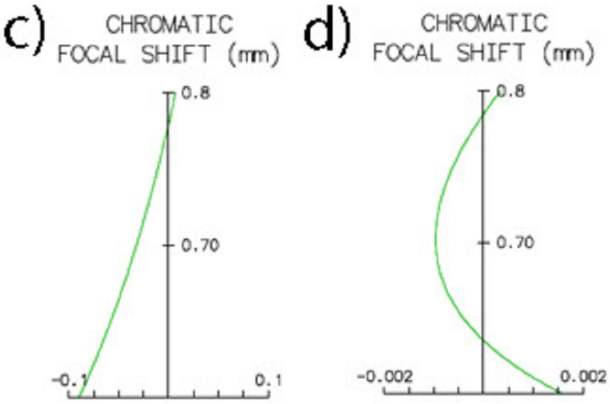

Figure 5.10: Graphs illustrate wavelength in μm (Y-axis) versus chromatic abberation shift in mm (X-axis). (a) Left graph shows the chromatic abberation for the currently used three lens system, optimized for a single wavelength (785nm). (b) Right graph shows the chromatic abberation for the five lens system, corrected for two wavelengths (785nm and 635nm), where the spot sizes of both lasers remain $<4\mu$m.

Part III

System Characterization

Chapter 6

Imaging with STM and nc-AFM

6.1 Introduction

Scanning tunneling microscopy images acquired in the constant current or constant height mode routinely provide atomically resolved images of surfaces. These images often represent the surface topography. Atomic positions are in fact a contour of constant *local density of states* (LDOS). Any peaks in LDOS may, or may not coincide with an atoms nuclei. Therefore, this may or may not reflect the actual position of an atom. Striking evidence of the latter occurs when STM peaks are not atoms but the quantum interference patterns observed on metal surfaces at low temperature, and the bias dependent images on semiconductor surfaces [13]. STM offers significantly different images and information, than an AFM typically provides.

In addition to this, site specific electronic data may be obtained using an STM. Spectroscopy such as I(V) or I(z) curves, *current imaging tunneling spectroscopy* (CITS), and work function maps are some examples only obtainable with an STM. Notable applications of such measurements, include analysis of state lifetimes and vibrational spectroscopy measurements [10].

Tunneling processes are additionally utilized to manipulate atoms, molecules and even vacancies, on surfaces [122, 123, 124]. This transforms the STM from a passive measurement tool into a unique, atomic-scale laboratory for building and measuring with atomic accuracy. STM's and to a lesser extent AFM's, remain unique tools to see and shape the environment in which they operate.

Multi-parameter imaging using a simultaneous *low temperature atomic force*

microscope/ scanning tunneling microscope (LT-AFM/STM) provides direct access to far more information than an STM or AFM alone. In particular, atomically precise force and energy related information inaccessible in regular STM imaging, provides a detailed picture of tip-surface interactions during tunneling. This means, force and energy dissipation data may be obtained, which are critical for accurate analysis of atomic and molecular scale manipulations, diffusion studies, bond formation investigations, or when species identification is difficult. This more detailed and complete picture of the STM image formation process is not only revealing and desirable. It is in fact, an absolute requirement for any serious analysis of tunneling processes.
Finally, recording tunnel currents present during atomic force imaging also provides invaluable complimentary data to force mapping. Bias dependent simultaneous nc-AFM/STM, and site specific work function maps, can for example help providing a clearer picture of a force signals origins and/or their nature.

In this chapter, the performance of the nc-AFM/STM is examined. First, STM topography, spectroscopy curves, topographic noise and tunnel noise spectra are presented and evaluated. In the following section, nc-AFM data acquired at liquid helium temperature are shown. These tests reveal and provide:

- a characterization of the instrument as a stand-alone STM,
- a calibration of the SPM system (described in parts in section 3.4.3),
- a characterization of the instrument as a stand-alone AFM,
- and finally, if the overall functions are suitable for future simultaneous nc AFM/STM experiments.

The STM system was tested in air prior to vacuum operations. The instrument is in a good condition with images showing atomic corrugations. In that case, it is assumed that the tunneling current feedback system, the XYZ scanner and the bias voltage perform as anticipated. However, with a working STM there is no information about the tip condition, the performance of the feedback electronics nor the efficacy of the vibration isolation. Ideally, the performance of the feedback electronics in the constant current mode should be tested with inert samples that have pronounced structural features. For these performance tests, three calibration samples, two types of STM tips, and two types of cantilevers were employed. The last section shows the present status of the instrument and the current development, where STM images with a conductive cantilever were taken.

Calibration Samples

Three samples were used during the system characterization in the STM and nc-AFM mode. First, results on the semi metallic *highly oriented pyrolytic graphite* (HOPG) are shown. Secondly, measurements on the semiconducting Silicon (111)7x7 surface are presented. Last, preliminary assessments were done on Au(111). All three samples were used in the LT-SPM and MD-SPM system to show that the improvements met the original problems.

The carbon atoms of HOPG are arranged in a honeycomb formation. HOPG provides researches in the SPM community with a smooth surface as substrates, calibration standard at the atomic scale and can be purchased off the shelf. As a semi metal, HOPG shows no reconstruction problems, has trivial electronic structure and allows others to replicate results with little effort [125].
The reconstructed Silicon(111)7x7 surface is used, simply because it is well studied. In SPM, it has been the standard sample for characterizations of structural and electronic properties at the sub-nanometer scale. It has the advantage of displaying significant band structure non-linearity around E_F, and therefore, is useful for analyzing spectroscopic performance.
In comparison to semiconductors, STM experiments of metal surfaces do not show a strong bias voltage dependence. For metals, the bias voltage is usually in the millivolt range. That is because of the overlap between the conduction and the valence band at the Fermi level. The Au(111) surface reconstruction provides a good base for molecular adsorption. The so-called "herringbone" pattern is created by a periodic bending of the parallel corrugation lines by ±120° every 25nm [126]. These long range superstructures are easily spotted and therefore can be used for preliminary performance tests.

6.2 Sample, Tips and Cantilevers

6.2.1 Sample Preparations

HOPG

HOPG consists of multi-layered structures which are parts of stacked planes. These structures have strong covalent forces within the lateral planes, whereas the planes are weakly bonded by Van der Waals forces. This explains the cleaving characteristics of HOPG [127]. The standard procedure is done with a piece of adhesive tape that is pressed against the flat surface. When peeling it off, the tape strips a thin layer of HOPG with it.

Silicon

The preparation of Si(111)7x7 reconstruction takes cautious steps. Silicon samples and molybdenum/ sapphire sample holders must be handled with ceramic or molybdenum tweezers[1] only, because nickel contamination occurs due to the contact with stainless steel tools.
Once transferred into vacuum, the sample must be outgassed by a direct current heating setup. The pressure should be kept below 1×10^{-9} mbar during the ramp up to 850°C, which is below the oxide removal temperature. After the sample and the holder have been degassed, the sample is flashed from 850°C to 1250°C, maintained for 10 seconds and returned to 850°C. This cycle is repeated 5 - 10 times. During the 10 seconds at the flashing temperature, remaining carbon is driven into the bulk [128]. The sum of the short ramp up and ramp down time should be no longer than 5 seconds. During these flashes, the pressure is not allowed to exceed 1×10^{-9} mbar. Otherwise, the surface looks rough and cloudy. [129].
The slow cool down to room temperature determines the quality of the surface reconstruction. It could be started immediately after the flashing or delayed. The cool down period to room temperature usually takes 30min (2 s/°C). If delayed, this post-anneal period at 850°C or lower is important for long range 7x7 domain order development [128]. Some groups have reported various tricks and techniques to control the terrace growth by step bunching [130, 131]. But annealing temperatures reported in literature may have reading errors up to ±50°C, depending on the pyrometer settings. The single wavelength pyrometer used in our sample preparations was cross checked with other vacuum system under similar conditions. The emissivity ϵ was set to a value of 0.67.

Gold

A reconstructed Au(111) surface can be obtained in UHV by multiple cycles of sputtering and annealing. This procedure is typically done for polished metal surfaces [91]. Besides the noble gases, gold is inert and posses the

---

[1] Tantalum and Teflon tools are also acceptable

lowest reactivity among the known elements [56]. Therefore, STM atomic resolution analysis can be performed in UHV as well as under ambient conditions.

6.2.2 Probe Preparations

STM Tips

Atomically resolved STM images can be obtained with manually cut [132] or controlled crashed tips [133]. By preference, STM tips can be fabricated from tungsten or platinum-iridium wires by grinding [134], field emission and evaporation [135], ion milling [136, 137], or electrochemical polishing/ etching [138, 139].
All these methods basically aim to prepare metal tips with a high aspect ratio. However, most of the tips fabricated with these methods are rather shredded-shaped or have multiple apexes. Because the apex nearest to the sample surface is responsible for tunneling, the resolution of STM images is affected by the geometry of the tip [44, 140, 141, 142]. Atomically sharp tips can be prepared by FIM [143, 144]. However, electrochemical etching is a feasible and reproducible method and has been optimized by many groups to fabricate atomically sharp STM tips [145, 146, 147, 148, 149, 150].

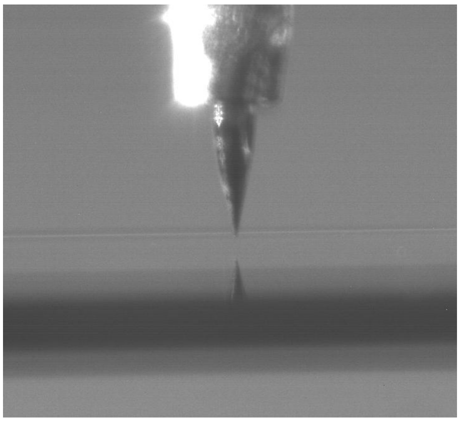

Figure 6.1: A tungsten STM tip is seen during coarse approach onto the Si(111)7x7 sample surface. The reflection of the tip on the sample surface can be recognized.

Most of the STM tips used in these measurements were acquired from commercial providers[2]. But the prospect of home made STM tips was explored

---

[2] Omicron NanoTechnology GmbH - www.omicron.de

to save time and costs. We used a home-built tip sharpener to chemically etch some of the tungsten tips [151]. Manually cut platinum-iridium tips were also adopted. This crude technique to prepare tips involves physical strength. One end of the platinum-iridium wire is clamped and the other end is held with a sharp cutter. As the two ends are slowly torn apart, the wire forms into a needle-like shape. After the procedure, the tip can be mounted onto a holder and is then ready to be inserted into UHV.

Cantilevers

Platinum tip coated and bare silicon cantilevers are attached with a conductive glue[3] onto an slanted tip holder (see section 3.3.3). Once the cantilevers are prepared, they get introduced into vacuum and heated above 100° for an hour to remove residual water molecules. The silicon tips are covered with a native silicon oxide layer that could be removed by sputtering or electron beam treatment in UHV [152]. Another method is the HF-etching prior to UHV insertion [153]. More interestingly, it has been shown that the quality factor improves by more than one order of magnitude by high temperature annealing [108].

6.3 Imaging HOPG

6.3.1 Initial STM Noise Evaluation

Ambient Conditions

Figure 6.2 shows a 10nm x 10nm STM topography image of HOPG acquired in the constant current mode and under ambient conditions. The bias voltage was set to 200mV and the tunnel current setpoint of 0.2nA was used. Honeycomb structures are observed. The lattice unit cell consists of two equidistant triangular which are intertwined in each other. Each triangular has three carbon atoms and are labeled with Q and T (figure 6.2(b)).
Under ideal conditions, HOPG images reveal a lattice with six carbon atoms arranged in a symmetric hexagonal pattern. However, the contrast in most SPM reported HOPG images show three carbon atoms per unit cell with a distance of 2.46Å between any two visualized atoms. Figure 6.2(a) shows actual topographic and tunneling current images of a HOPG surface, whereas figure 6.2(b) illustrates the symmetric arrangement of the lattice.

---

[3] Epoxy Technology, Inc. - www.epotek.com

Since the value of interatomic spacing is known from theory and previous STM experiments, the HOPG surface can be used to calibrate the scanner in the XY directions [127]. The calibration procedure involves counting the number of atoms and multiplying this by 2.46Å (see figure 6.2). With the consideration of the HV-amplifier gains, this value is divided by the voltage applied to the Piezo. The piezo constant at room temperature is in our case 31.2nm/V (see section 3.4.3). This procedure is done for the lateral XY-directions. The calibration in the Z-direction is commonly done with a step height. It should be noted that the calibration is temperature dependent, and must be repeated at 77K and 4K.
In addition to the topography images, analysis have shown that the error signal of the tunnel current images is relatively large. It implies that "true" tunneling may be not the case and that "physical" contact of the tunneling tip with the surface may be responsible for the atomic periodicity [12, 154].

Figure 6.3 shows a sequence of nine topographic images in the constant current mode, which are used to examine measurement reliability and qualitative performance. These images were acquired without drift correction. All STM topographic images in this sequence display atomic periodicity, indicating that the control system is capable of repeatable and stable imaging over long measurement periods (45 minutes). However, the images also reveal irregular atomic contrast, which suggests that frequent tip changes occured. But, this indicates that regular tip changes can happen without detrimental tip crashes. All in all, this sequence of topographic images demonstrates the minimum flexibility in the feedback configuration and the control electronics.

Figure 6.4(a) and 6.4(b) show the topographic image and the line profile recorded in the constant current mode. The depicted profile of the surface across seven atoms shows a corrugation of 40pm. The topographic peak-peak noise sitting on top of the line profile is measured and gives a value of 10pm.

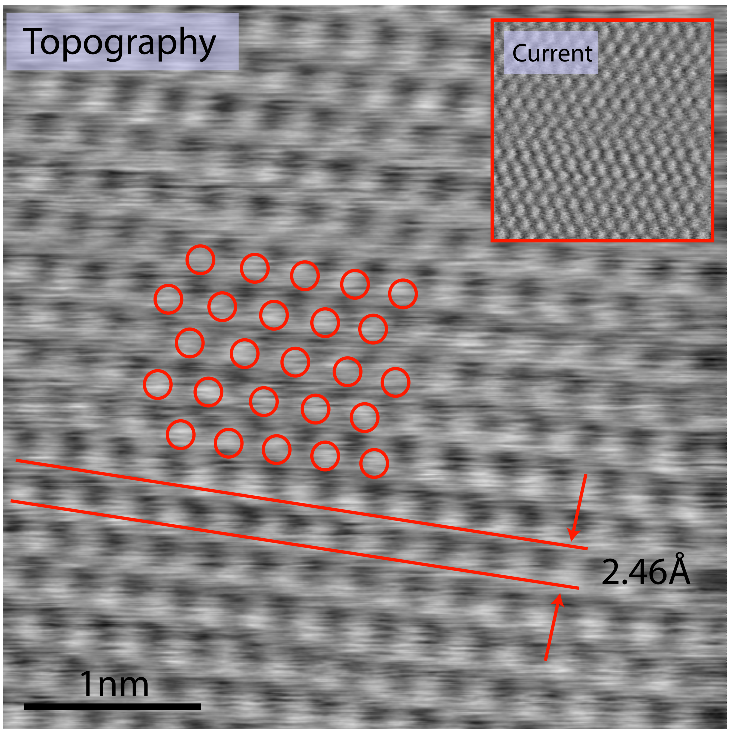

(a) Topography image

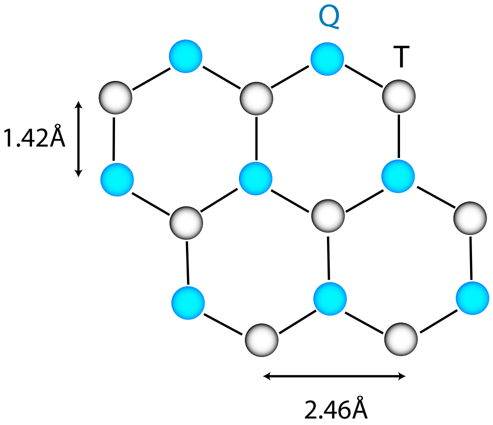

(b) Honeycomb structure

Figure 6.2: (a) This topography image of HOPG reveals the commonly observed threefold symmetry pattern. The red rings indicate one set of visualized atoms which are separated by 2.46Åfrom each other. Inset: tunneling current image. (b) This illustration shows the idealized honeycomb pattern divided in two sets of atoms labeled as Q and T. Under usual SPM imaging conditions, either set of atoms are visualized.

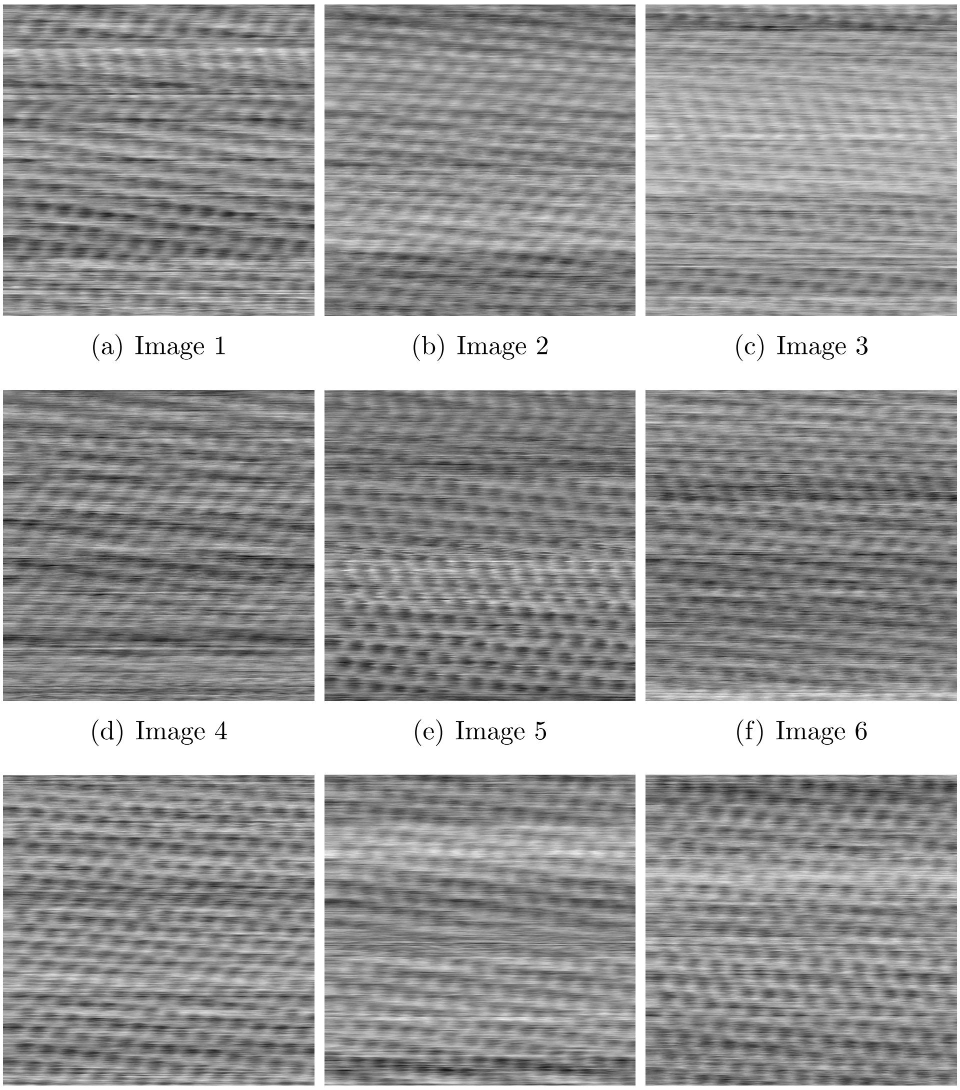
(a) Image 1 (b) Image 2 (c) Image 3

(d) Image 4 (e) Image 5 (f) Image 6

(g) Image 7 (h) Image 8 (i) Image 9

Figure 6.3: Without drift correction a sequence of nine HOPG raw 4x4nm topographic images under ambient conditions was taken during a period of 45 minutes. Parameters (I_t=429pA, U_{bias}=+107mV).

Similarly, a line profile was taken from the tunneling current image in the figure 6.4(c) shown in figure 6.4(d). The numerous tip changes can be explained by considering the acoustical noise during imaging under ambient conditions. In addition, the measurements were performed at room temperature where drift affected the results. Finally, because the eddy current dampers were designed for operation at 4K, the vibration isolation system were not fully optimized.

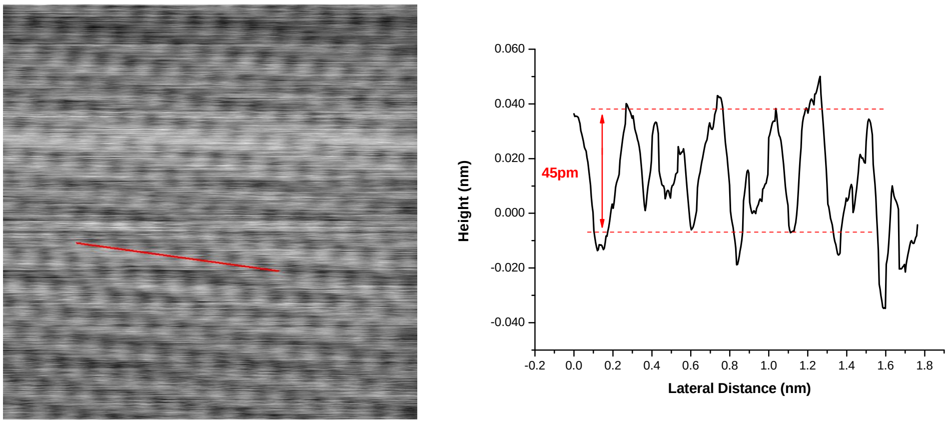

(a) Topography image

(b) Topography line profile

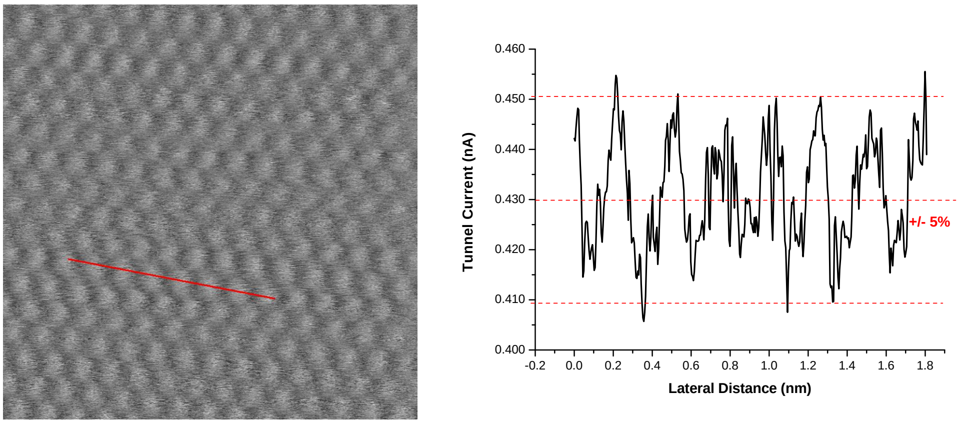

(c) Tunnel current image

(d) Tunnel current line profile

Figure 6.4: HOPG lineprofile under ambient conditions. Parameters (I_t=429pA, U_{bias}=+107mV). (b) The topographic line profile reveals a corrugation of 45pm peak-peak. (d) The tunnel current line profile shows a tunnel current variation of $\approx \pm 5\%$, which corresponds to ±20pA peak-peak.

UHV Conditions

The quantitative performance tests were repeated in UHV. The 5x5 nm image shown in figure 6.5 was taken in the constant current mode with a tunnel current setpoint of 70pA and a bias of 100mV.

In UHV, acoustical noise should be eliminated and the vibration isolation system operated under aligned conditions. Line profiles of topography and tunnel current images were taken as to confirm the expected improvement of the measurement quality.

To achieve stable operation conditions in UHV and at low temperature, the spring suspension, the eddy current damping system and the concentric LN2/ LHe cryo shields must be well aligned to avoid any physical contact between each of them. Even though, the imaging quality and the line profiles affirm that the relative topographic noise is reduced in UHV, a certain blurriness or interlacement still persists and can be noticed under ambient as well as UHV scanning conditions.

Interlacement Issue

A closer look at the topographic and the tunnel current images reveal what appeared to be a mismatch of consecutive lines during the scanning. Figures 6.6(a) and 6.6(b) show typical constant current images acquired under ambient conditions. Figures 6.6(c) and 6.6(d) are enlarged sections of the topographic and tunnel current images. Interestingly, the interlacement occur only in the horizontal forward-backward directions and is visible in both STM imaging channels. This "feature" persists in the same horizontal direction even when the scanning is rotated by 90°. This suggests instabilities of the tip-sample gap. In order to evaluate the mechanical rigidity, a spectrum analyzer was used to measure the tunnel current output as a function of the frequency of an excitation signal applied to the piezo scanner in the Z-direction. Ideally, a flat spectrum with a resonance of the piezo scanner in the Z-direction is expected. The spectra depicted in figure 6.7 shows two distinct peaks (480Hz and 710Hz) below the resonance frequency of the piezo scanner (1.9kHz). After removal of the instrument from UHV an optical deflection measurement system was used to measure the response of the sample holder receiver for oscillatory signal applied to the X and Z-direction of the piezo scanner. Interestingly, two pronounced peaks appeared when the X-direction only was excited (see figure 6.7(a)). This showed that the mechanical stability of the constructed XY-sample positioner (see section 3.3.2) is not sufficient.

Our solution strategy is as follows. First, the XY-sample positioner was re-

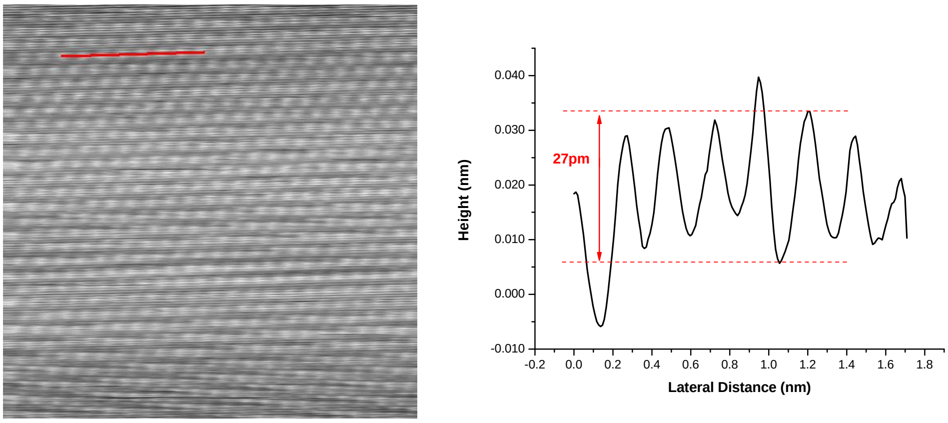

(a) Topography image

(b) Topography line profile

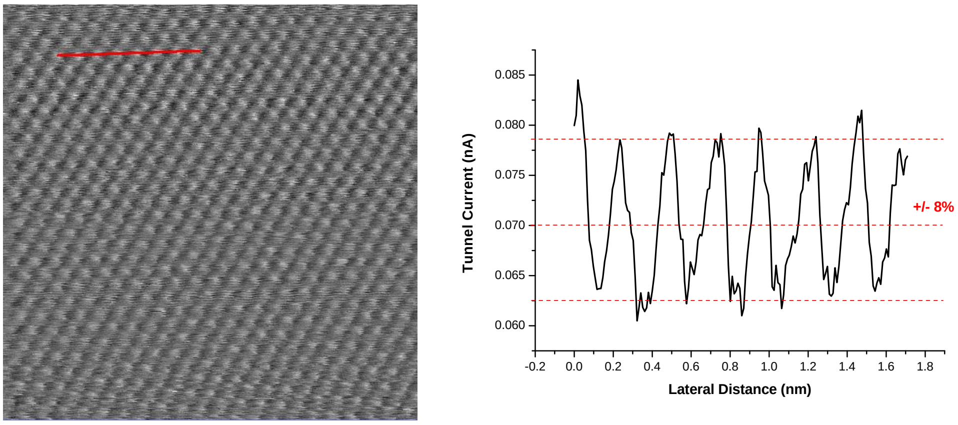

(c) Tunnel current image

(d) Tunnel current line profile

Figure 6.5: HOPG images and lineprofiles of RT, UHV. (b) The topographic line profile shows a corrugation of 27pm peak-peak. (d) reveals a tunnel current variation of ≈ ±8%, which corresponds to ±8pA peak-peak. Parameters (I_t=70pA, U_{bias}=+100mV).

moved to allow a continuation of ongoing experiments. Second, the design and assembly of a new type of XY-sample positioner was started, but could not be completed during the time this thesis was drafted.

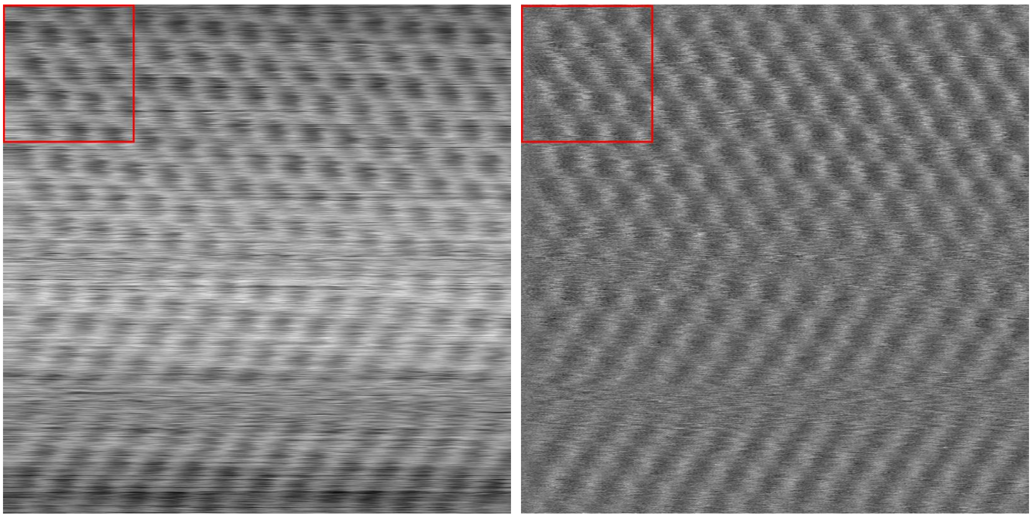

(a) Topography image (b) Tunnel current image

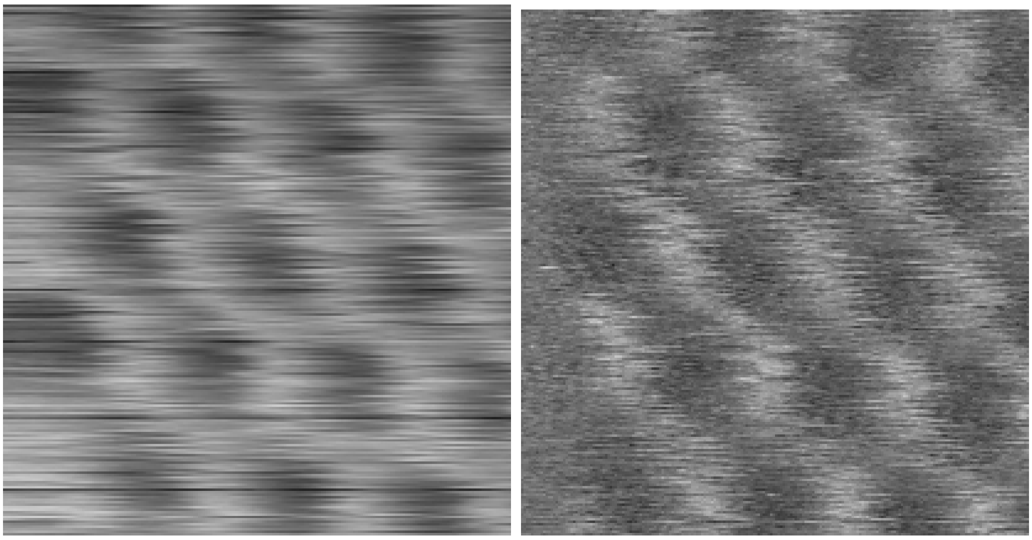

(c) Enlarged section of (a) (d) Enlarged section of (b)

Figure 6.6: HOPG interlacement at ambient conditions. (c) and (d) are the enlarged sections in the topographic and tunnel current images, which show the mismatch of consecutive scan lines. Parameters (I_t=429pA, U_{bias}=+107mV).

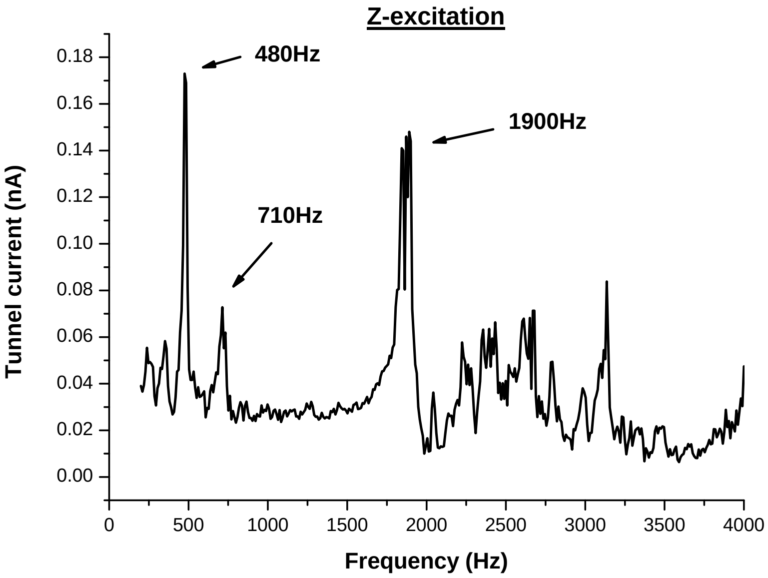

(a) Tunnel current spectrum

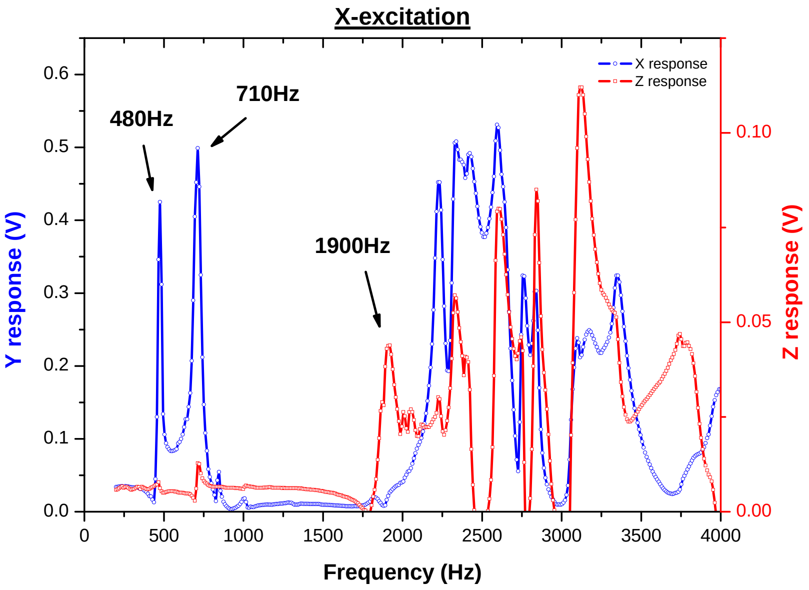

(b) Noise spectrum of X-excitation

Figure 6.7: The noise - and the tunnel current spectra show two low frequency peaks at 480Hz and 710Hz, which may be the origin of the lateral instability as observed in figure 6.6.

6.3.2 STM Noise Evaluation without XY Positioner

STM at Liquid Nitrogen Temperature (77K)

After the modification, brief tests under ambient conditions were performed. The system was cooled to nitrogen temperatures, where the data show that the modification improved the imaging quality (Figure 6.8).

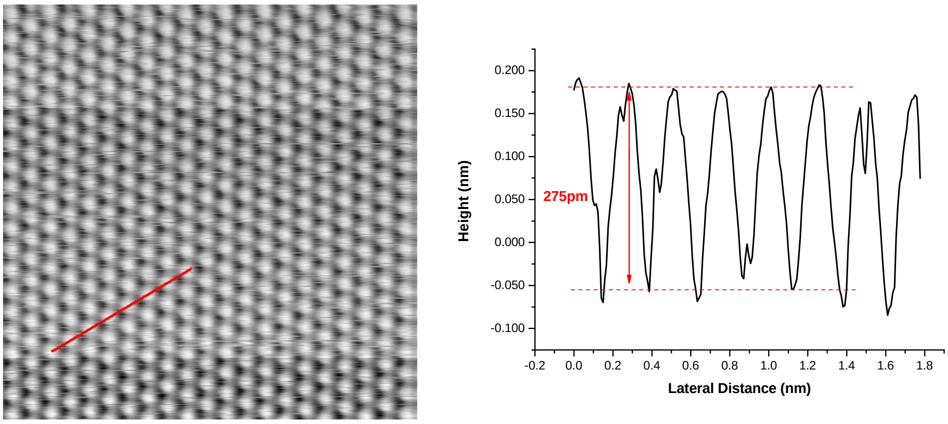

(a) Topography image (b) Topography line profile

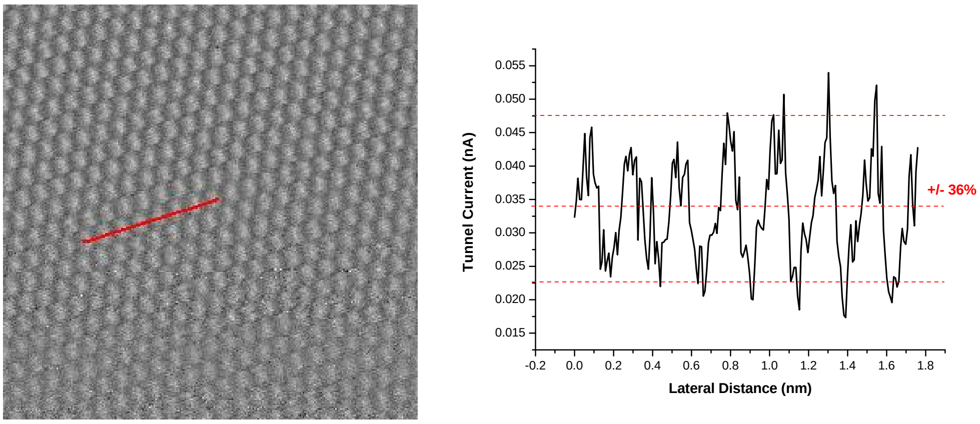

(c) Tunnel current image (d) Tunnel current line profile

Figure 6.8: Lineprofile of HOPG at 77K. (b) The topographic line profile shows a corrugation of 275pm peak-peak. (d) reveals a tunnel current variation of $\approx \pm 36\%$, which corresponds to $\pm$13pA peak-peak with parameters (I_t=30pA, U_{bias}=+20mV).

A series of three sequential images at constant height were recorded to demonstrate the tip-sample gap stability of the instrument. Figure 6.9 shows the tunnel current images, where they were acquired during 52 minutes.

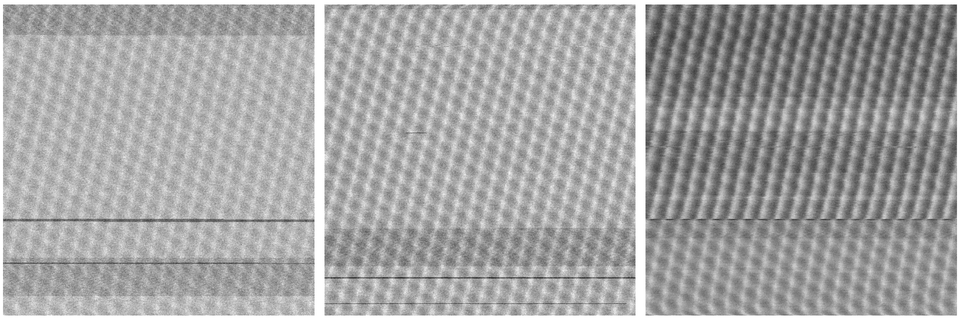

(a) 1st image, I=13pA (b) 2nd image, I=24pA (c) 3rd image, I=45pA

Figure 6.9: Constant height 10x10nm images at 77K (U_{bias}=+2mV).

Scanning Tunneling Spectroscopy

Scanning tunneling spectroscopy (STS) probes the electronic states of surfaces at the atomic scale [7]. STS enables the study of the local electronic structure of thin insulators, semiconductors and metals. The bias voltage dependent spectroscopy I(V) graph in figure 6.10 represents 50 averaged curves over a period of 60 seconds. The linear behavior of the curve indicates metallic surface states [155].

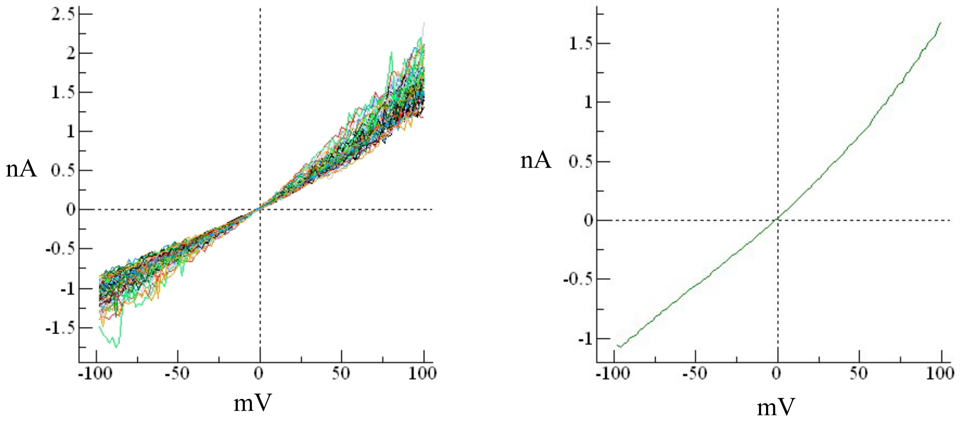

(a) Individual I(V) curves (b) Averaged I(V) curve

Figure 6.10: Averaged I(V) graph of 50 curves (bias sweep from ± 100mV).

6.4 Imaging Si(111)7x7

6.4.1 STM at 293K and 77K

Since the invention of the STM the Si(111)7x7 surface is commonly used as a standard sample for scanning probe microscopy [34].

In this thesis, the Si(111)7x7 surface is also used for test and calibration purposes of STM and AFM imaging. Figure 6.11 shows an empty state topography image along with the tunneling current image. The assessments of the correct bias voltage, the determination of the drift rate and the piezo scanner calibration were performed (see section 3.4.3).

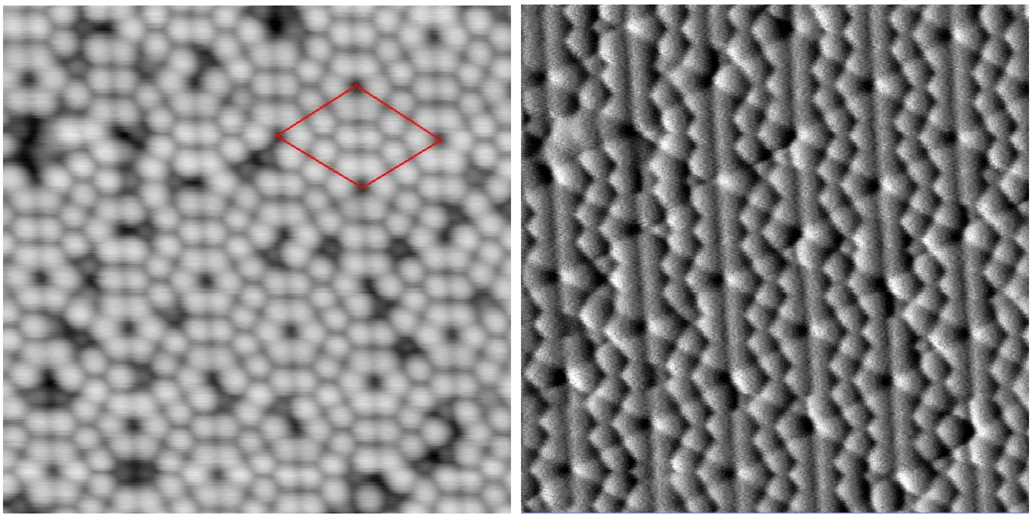

(a) Topography image (b) Tunneling Current image

Figure 6.11: STM topography and tunnel current image of Si(111)7x7 at room temperature. The red rhomboid in the topographic image represents the size of a unit cell. Parameters (I_t=20pA, U_{bias}=+2.0V).

Images of larger scan ranges in figure 6.12 show stabile imaging conditions and indicate that sample preparation could still be improved. The crack along the slow scan direction implies a slight overheating during the sample preparation. The result may explain the bright spots, which are phosphor dopants in the silicon bulk driven to the surface.

Figure 6.13 presents STM images of the Si(111)7x7 reconstruction with positive and negative bias taken at 77K. As suggested by the DAS model, each half unit cell contains six protrusions at the sites of the adatoms [98, 156]. There are distinct differences between the two images, which suggest that the bias dependence reveal additional information in the filled states topo-

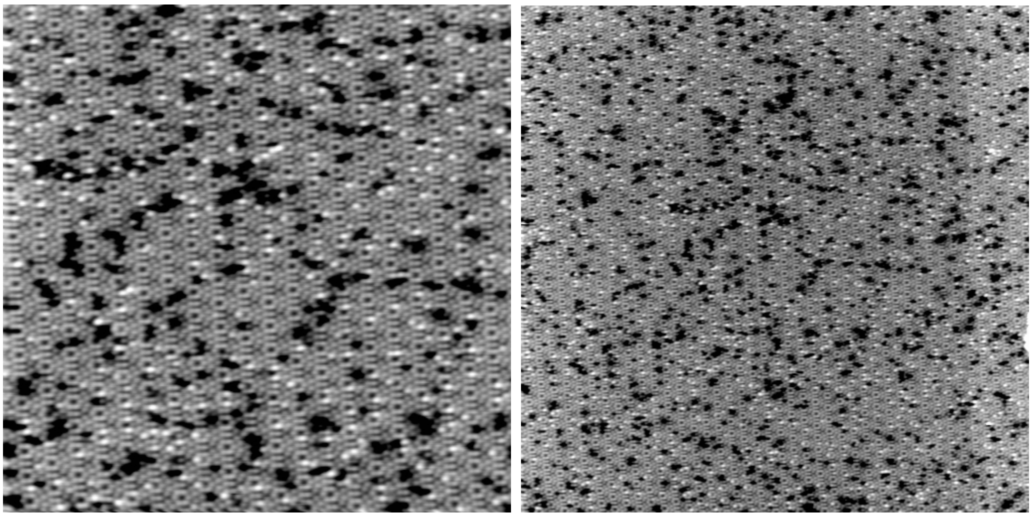

(a) 50nm

(b) 100nm

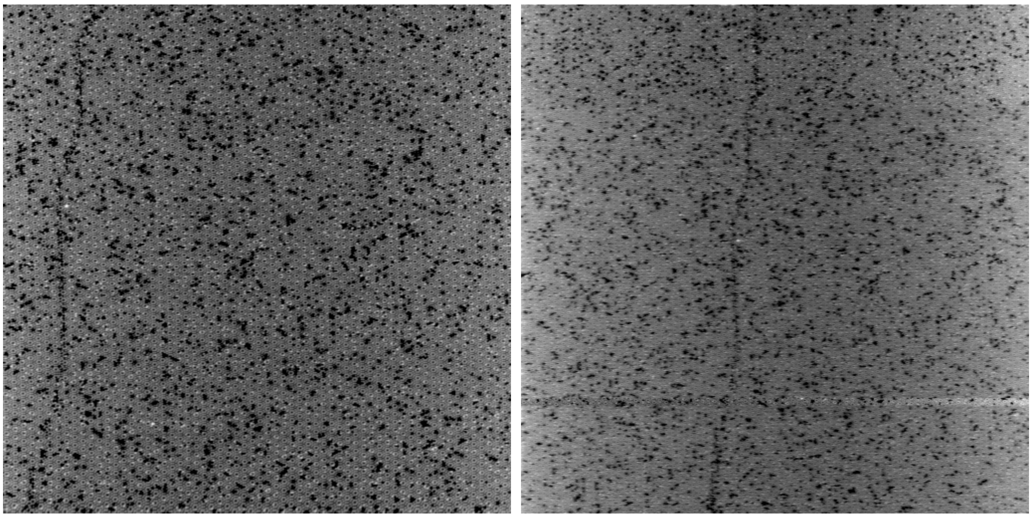

(c) 150nm

(d) 200nm

Figure 6.12: Different large area scans of Si(111)7x7 at 77K with relatively low tunnel current. Scanning parameters (I_t=13pA, U_{bias}=+1V). Corner holes can be clearly recognized in the images (a)(b)(c). But they are barely visible in the last topographic image (d). The crack and bright spots may be due to the overheating during sample preparation.

graphic image (bright spots). The empty state image shows a six-fold symmetry, while a three-fold symmetry with faulted and unfaulted stacking are observed in the filled state image.
Another interesting feature is the elastic surface deformation in STM studies,

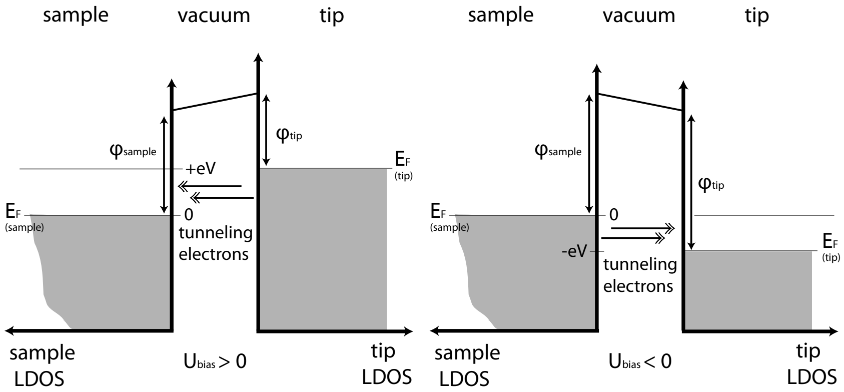

(a) Empty states topography image (b) Filled states topography image

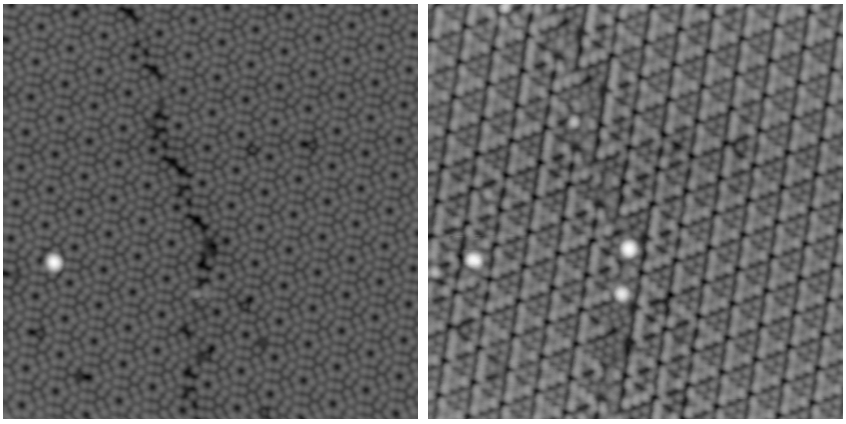

Figure 6.13: Top left: electrons tunnel from the tip into the empty states of the sample when a positive sample bias is applied. Top right: when a negative sample bias is applied, electrons tunnel from the filled states of the sample into the tip. - 10x10nm STM images of Si(111)7x7 surface: (bottom left) tunneling into empty states of the sample with I_t=50pA, $U_{bias} = 2.0V$ and (bottom right) tunneling from the filled states of the sample I_t=-50pA, U_{bias}=-2.0V. The crack is visible in both images, whereas some bright spots are only visualized in the filled states topographic image.

which reveal the concept of interatomic induced forces. Giant corrugations indicate the existence of interatomic forces between the tip apex and the atoms on the sample surface [12]. The AFM maps these forces as the cantilever tip scans over the surface sample. The next section demonstrates the nc-AFM performance of the LT-SPM system on the reconstructed Si(111)7x7 at liquid Helium temperature.

6.4.2 nc-AFM at 4.5K

In addition to the STM operation at 77K, imaging Si(111)7x7 in nc-AFM at liquid Helium temperature (4.5K) demonstrates the system's versatility. This shows that tip and sample transfers work accordingly. The consumption rate of LHe, cool down rate, drift rate and the scanner calibration were determined. Uncoated commercial silicon cantilevers (Nanosensors, SSS-NCH, 40N/m) were used. The following experiments were taken before the discussed problems with the XY-sample positioner were identified and are hence of relative poor quality. Nevertheless, the images shown in figure 6.14 demonstrate that atomic resolution could be obtained with PLL and self excitation modes using the fundamental and second flexural oscillation mode of the cantilever [26, 157].

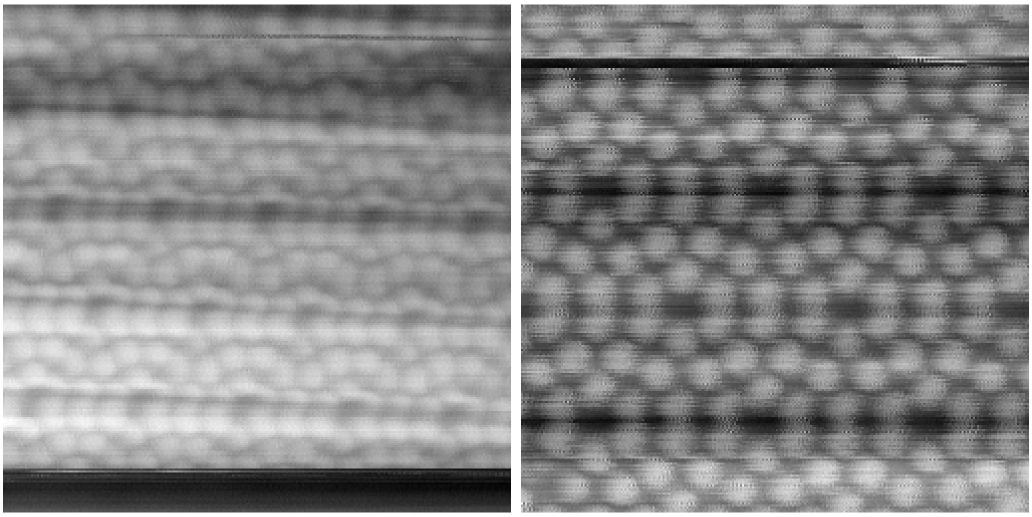

(a) First mode PLL (b) 2nd mode PLL

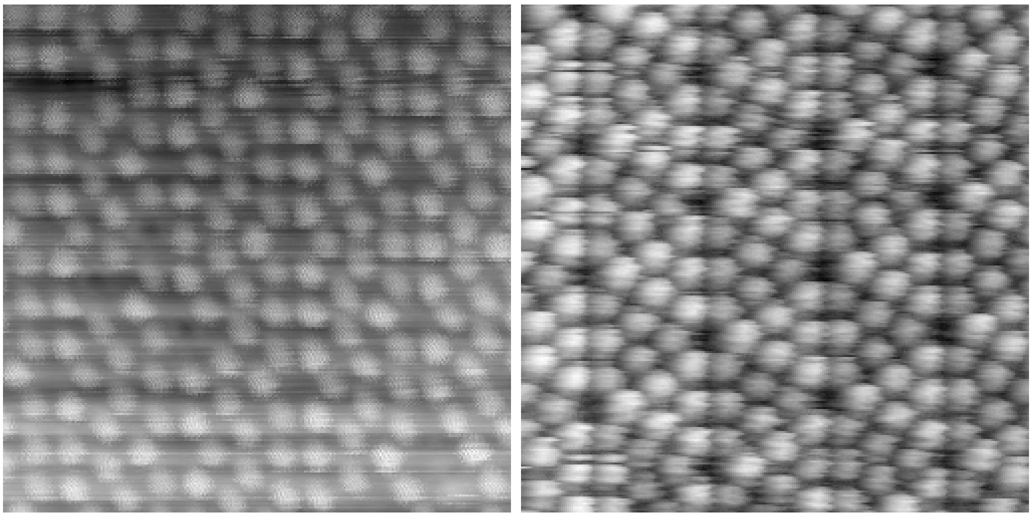

(c) First mode SE (d) 2nd mode SE

Figure 6.14: Plane corrected nc-AFM raw data acquired at 4.5K using the fundamental and second mode of the cantilever oscillation. Parameters (f_0=936858Hz, f_1=1.65MHz, A=7-11Å) and cantilever from Nanosensors (SSS-NCH, 40N/m).

Force Curves

Two separate force spectroscopy measurements over a corner hole (f_1=1.65MHz, A=7Å) and adatom site (f_1=1.62MHz, A=11Å) were performed from a nc-AFM image taken on the second flexural cantilever oscillation mode with a PLL feedback detection similar to figure 6.15. A commercial cantilever (40N/m) was used with f_0=936858Hz and Δf=-52Hz.

Both force curves were converted from the measured frequency shift curves by using Sader's formula (see section 2.2.5). The first force spectroscopy measurement (figure 6.16(a)) of a corner hole exhibits a high force sensitivity (<5pN) with an effective second mode stiffness of ≈1600N/m. The value estimated based on equivalent point mass model [88]. Moreover, it affirms a weak tip-sample interaction (large tip-sample separation) during imaging.

The second force spectroscopy measurement (figure 6.16(b)) shows the repulsive regime in the force curve. The kink in the curve may be due to tip-induced instabilities. But strong evidence suggests that rather tip-sample gap fluctuations may be the origin of the blurred images in figure 6.14.

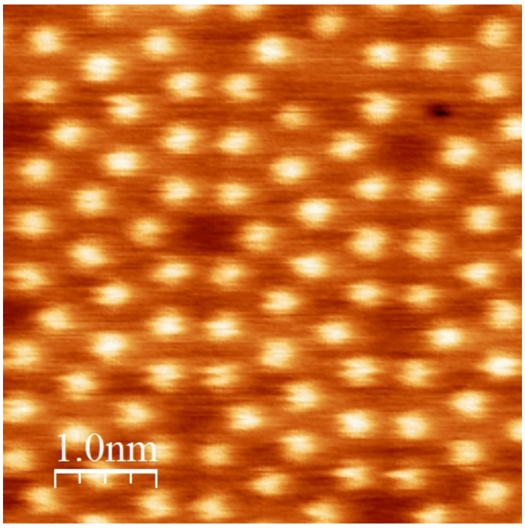

Figure 6.15: Constant Δf topographic 5x5nm image of Si(111)7x7 obtained with the second cantilever oscillation mode at 4.5K. Parameters (f_0=936858Hz, f_1=1.65MHz, A=7-11Å) and cantilever from Nanosensors (SSS-NCH, 40N/m).

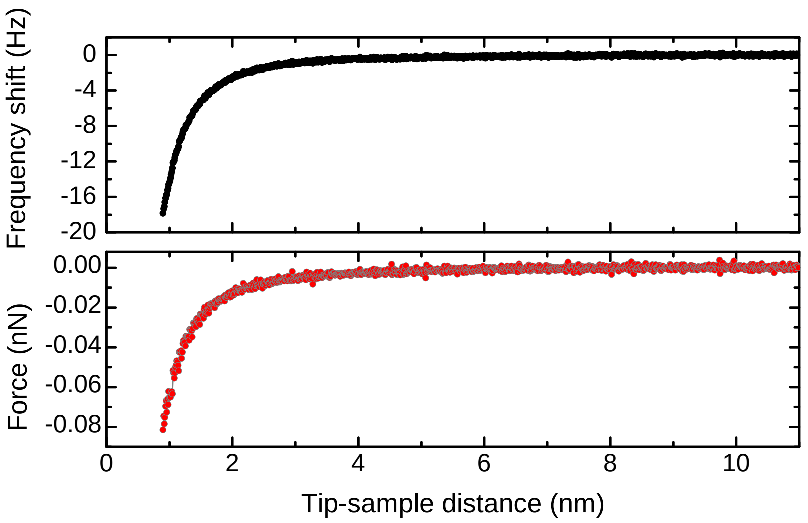

(a) Over a corner hole

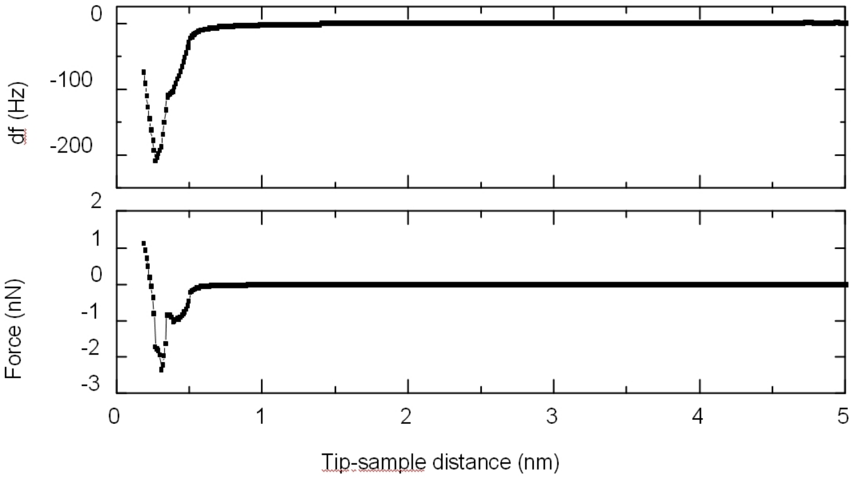

(b) Over an adatom

Figure 6.16: Force spectroscopy curves: (a) over a corner hole and (b) adatom. Force curves were converted from the Δf curves with the Sader's formula (see section 2.2.5).

6.5 STM Imaging Au(111)

The Au(111) reconstruction is the result of the interatomic separation contraction of the surface atoms along the [110] direction, which varies between 2.89Å(bulk value) and 2.75Å(average value) [158]. The reason for this is that 23 top layer gold atoms are arranged over 22 bulk lattice atoms in this direction, resulting in a $23\text{x}\sqrt{3}$ superstructure known as the "herringbone" pattern [126].

While the LT-SPM system is being modified, the MD-SPM system was recently put in operation. Proposed modifications to fix the XY-motors were adapted in both systems. Preliminary results performed with the MD-SPM on Au(111) and Si(111)7x7 are presented here. Figure 6.17 shows the topographic and tunnel current images of the herringbone superstructure. Line profiles in the fast and slow scan directions were taken. The average corrugation height of 6.8pm exhibits a 0.4pm topographic noise on top of it (left line profile, fast scan horizontal direction). The line profile in the slow scan direction indicates a topographic noise value of 1.8pm.

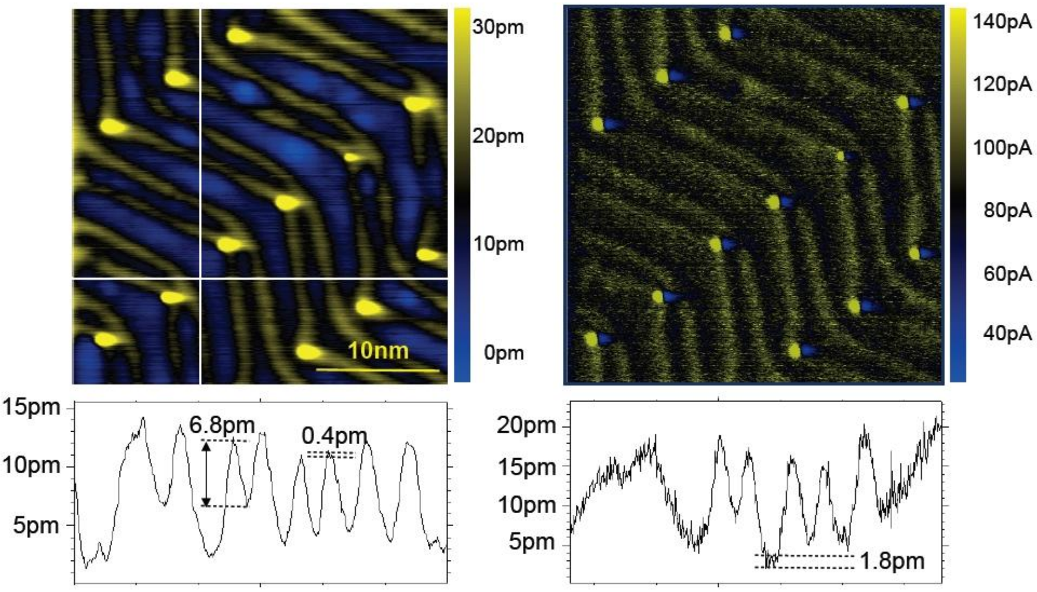

Figure 6.17: 50x50nm STM image on the reconstructed Au(111) at 6.3K. Top left: topographic image. Top right: tunnel current image. Bottom left: horizontal line profile. Bottom right: vertical line profile. Parameters (I_t=150pA, U_{bias}=+82mV).

6.5.1 Tunneling Cantilever

First attempt to perform STM at 77K on the LT-SPM system with a conductive cantilever[4] resulted in the 20x20nm image shown in figure 6.18. A unit cell of the reconstructed Si(111)7x7 is visible in the topographic and tunnel current channel. Although, this atomic resolution image is blurred and of poor quality, the result demonstrates that the basic requirements for simultaneous nc-AFM/STM are provided. Unfortunately, the cantilever frequency shift could not be measured due to software and hardware issues and restricted further STM measurements with the conductive cantilever.

New attempts to repeat the same measurement on the MD-SPM system at 6.3K demonstrated the improved stability of the instrument. The 50x50nm image in figure 6.19 was recorded with a tunnel current setpoint I_t=40pA, +2V bias and shows disordered Si(111)7x7, which may also due to overheating during sample preparation (see section 6.4.1). A short line profile across seven atoms reveals an average corrugation height of 13pm (see figure 6.19(b)). The 25nm long line profile across a corner hole and numerous defect sites (or missing atoms), implies a total average corrugation height of 135pm.

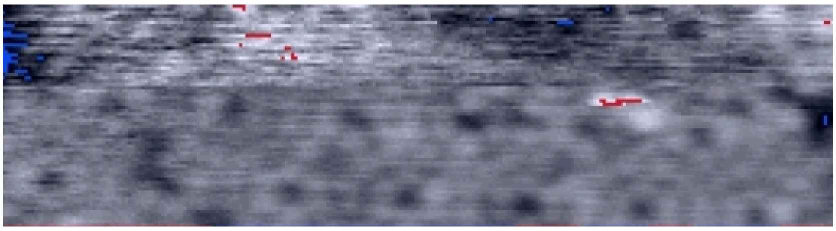

(a) Topographic image

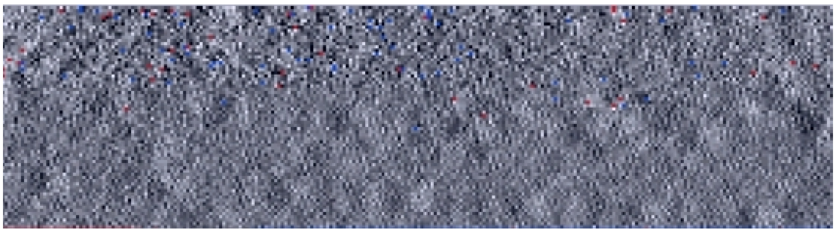

(b) Tunnel current image

Figure 6.18: Tunneling with cantilever (LT-SPM) at 77K. Parameters (I_t=10pA, U_{bias}=+2V). (a) Topographic image and (b) tunnel current image.

---

[4] Cantilevers (PPP-NCHPt) with Pt/Ir coated tip from Nanosensors - www.nanosensors.com

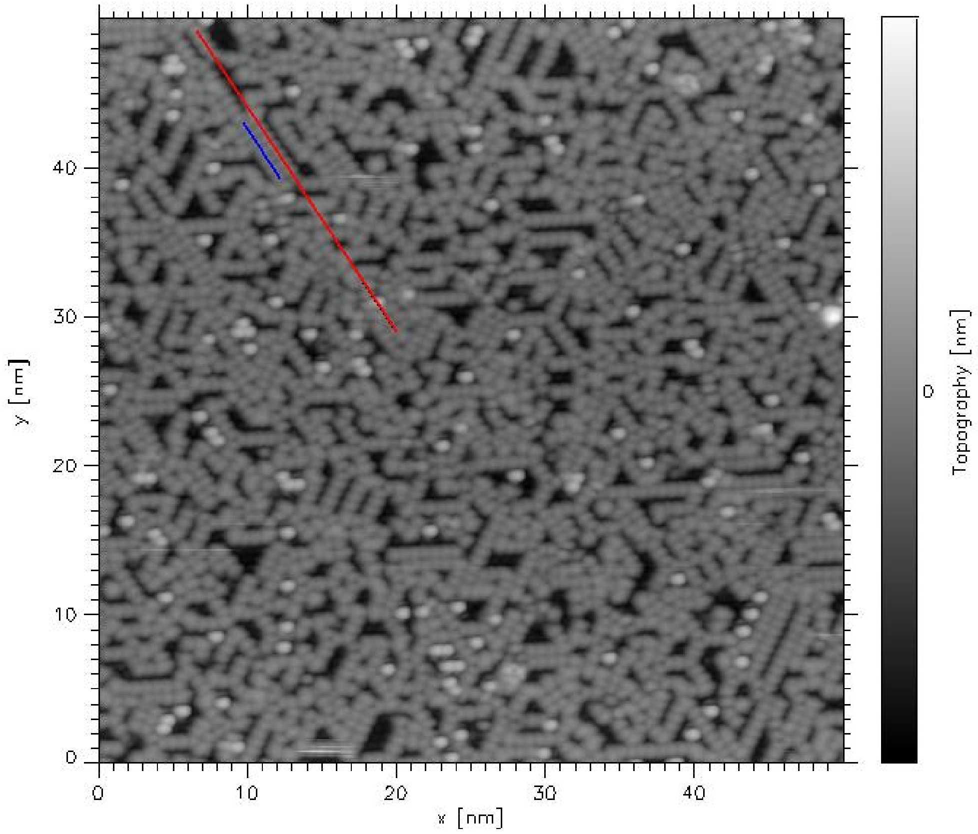

(a) Topographic image

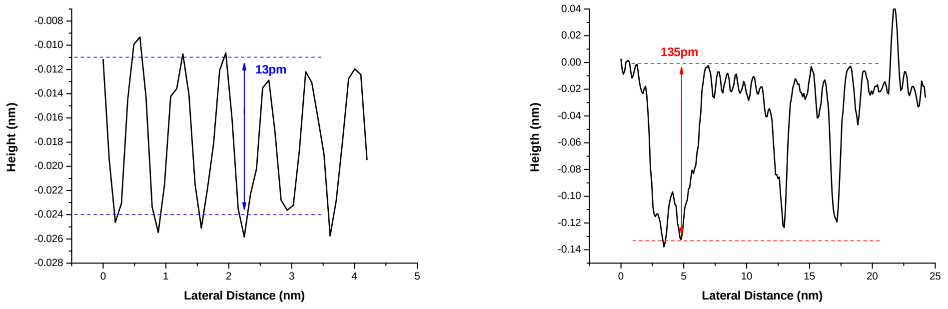

(b) Blue Line Profile

(c) Red Line Profile

Figure 6.19: Tunneling with cantilever (MD-SPM) at 6.3K. (a) Topographic image of disordered Si(111)7x7. (b) The line profile of the blue line. (c) The line profile of the red line. Tunneling parameters (I_t=40pA, U_{bias}=+550mV).

6.6 Chapter Summary

STM measurements on the semimetal HOPG were conducted to test, calibrate and characterize the LT-SPM system under different conditions. Noise measurements were performed to identify possible sources.

STM imaging on Si(111)7x7 offered the verification of the correct sample preparation procedure and the opportunity to test the instrument with a semiconductor.
nc-AFM was performed at 4.5K on Si(111)7x7. Two excitation schemes were tested, as commercial available cantilevers (40N/m) were excited at their fundamental and second oscillation modes. Measurements with a hard cantilever (500N/m) could also be performed. Higher cantilever oscillation modes and operations with hard cantilevers are alternatives to obtain stable amplitudes varying between 7Åand 11Å. In addition, all four sets of results imply a mechanical instability in the instrument. Force spectroscopy data support this presumption, which is rather due to tip-sample fluctuations and not tip changes.

While the LT-SPM system is being upgraded, first tests were conducted with the MD-SPM system and revealed stable imaging conditions on Au(111) at 6.3K. Preliminary images recorded with a tunneling cantilever demonstrated the stability of the instrument, where an average corrugation height of 13pm could be determined.

Various instrumental problems have delayed the study of samples with atomic resolution. The two main problems were the electronic control system and the XY-sample positioner of the microscope that had to be redesigned within this work. Nonetheless, the LT-SPM could be improved to a status in which atomic resolution is routinely possible, both in STM and AFM mode at room temperature, 77K and 4.5K.

Part IV

Cantilever Cooling

Chapter 7

Laser-induced Effects on Cantilevers

7.1 Introduction

Atom cooling[1] is known as the techniques of cooling gas atoms with several laser light sources to subkelvin temperatures. The idea is to reduce the kinetic energy of individual atoms and hence the overall Brownian motion. Energy is effectively taken out of a system by photon momentum transfer and therefore, the object of investigation can be actually cooled. The exact techniques employed and further details can be drawn from the works of Chu, Cohen-Tannoudji, Phillips, Cornell, Metcalf and many others [159, 160, 161, 162, 163, 164, 165].

7.2 Atom Cooling

An electromagnetic wave carries a momentum with it. Therefore, if an object is exposed to light, a particular kind of force is exerted on its surface, which is known as radiation pressure. The force behind atom cooling is also caused by radiation, especially by light at or near the resonance frequencies of atomic transitions. Besides the linear momentum $p = \hbar k$ and angular momentum $\pm\hbar$, each photon also carries energy $\mathrm{E} = \hbar\omega$. When it absorbs light, an atom stores the energy by becoming excited. Re-emission induces a change in the atom's velocity (spontaneous or stimulated) due to the relation between momentum and energy $p = \mathrm{E}/c$. Even though, each velocity change is very small compared to the thermal velocity (Brownian motion), multiple

---

[1] or often referred to *laser cooling*

absorptions can sum up to a total velocity change. Thus, a radiative force is used to adequately control this velocity change to decelerate and therefore cooling free atoms.
Now the question arises whether this technique can be applied to molecules and larger objects? And is it possible to cool a macroscopic object such as a cantilever in AFM?

7.3 Cantilever Cooling

In analogy to atom cooling, Dorsel et al first observed damping effects on the high finesse cavity mirrors in gravitational wave detectors [166]. Thermoelastic damping, radiation pressure, photothermal effects and thermodynamical fluctuations of coated mirrors in gravitational wave detection have been thoroughly investigated by Braginsky et al [116, 167, 114, 117, 168, 169] and many others [170, 171, 172, 173]. Cohadon et al described an experiment, where they used an electronic feedback mechanism to either cool or heat a mirror of a large mechanical resonator by radiation pressure [174]. Based on similar findings on the micrometer scale, cantilever cooling[2] has been observed since the early days of nc-AFM, when optical interferometers were introduced to detect the cantilever's position. The influence of the laser on the cantilever's motion has been studied in the work of Moser et al [109]. Damping and amplifying effects on the cantilever's dynamics were observed, investigated and employed to control the Q factor of the cantilever [175, 176]. Even though many articles related to the cooling of micro-mechanical resonators have been published recently [177, 178, 179], the dynamical behavior behind its process is still not completely understood.
But, what is cantilever cooling? To grasp the essence of cantilever cooling, comprehension of the forces behind it is eminent.

7.3.1 Photon-induced Forces

The cantilever is exposed to photon-induced forces that are dependent on the Fabry-Perot cavity length and the force on the cantilever deflection z. The overall photon-induced force which bends the cantilever $F_z = \Sigma_n F_n(z)$ is proportional to the laser intensity stored in the cavity. F_z includes two forces, which can affect the dynamical and noise spectrum behavior of the cantilever. One is the above mentioned radiation or photon pressure. The other one arises from the photothermal effects. Two characteristics of those

---

[2] In various publications, cantilever cooling is also called *cavity cooling*, *cold damping* or *mode cooling*.

forces must be considered. First, the corresponding characteristic response time compared to the oscillation period determines whether the resonance frequency or the cantilever quality factor Q are mainly affected. Experiments and numerical estimations show that the overall photon-induced effects are significant, especially if the cavity finesse is high. Second, the absolute values of these forces are interesting to know, but difficult to obtain, although their relative contributions can be estimated. Their slopes versus cavity detuning compared to the cantilever spring constant may cause the observed asymmetry of the interference pattern. However, due to preliminary inconsistent results, no conclusive estimates could be drawn and presented at this time.

Characteristic Response Times

Radiation pressure is one type of force relevant to cantilever cooling. In general, its influence is independent of the cantilever's base temperature. The forces related to radiation pressure act almost instantaneously on the cantilever, leading to a very short characteristic response time[3] τ_{rp}. However, when the reflectivity of the cavity approaches unity, the response to radiation pressure is appreciably reflected so that its contribution to the overall photon-induced damping increases. The prolonged response time then can be estimated from the following equation:

$$\tau_{rp} = \frac{L}{c(1-\sqrt{R_1 R_2})}, \tag{7.3.1}$$

where L is the cavity length, c is the speed of light in vacuum. R_1 and R_2 represent the reflectivity of the mirrors in the cavity [180]. In our case, numerical estimation gives a value of $\tau_{rp} \approx 26\text{ps}$. This is extremely short, particularly when compared to the period of the cantilever oscillation.

The other kind of force arises from the *photothermal effect*, and appears to be temperature dependent. These forces become dominant when the cantilever partially absorbs the incident light, which results through differential thermal expansion between the gold coating and the silicon cantilever. As in a bimetal sensor, the gold coated cantilever deflects proportionally to the absorbed energy. As a consequence, the cantilever senses a photon-induced force which opposes or enhance its own mechanical restoring force. This

---

[3] In gravitational wave detection this is also known as the *cavity storage time* while in atom cooling the *radiative lifetime* of the excited states is relevant.

leads to a response time τ_{ph}, which is delayed or sustained oscillations with respect to abrupt changes in the position of the cantilever. To estimate τ_{ph}, the heat capacitance, thermal conductance and thicknesses of the silicon and the partial gold coating with the copper intermediate layer must be taken into account. The simple equation below expresses to the case when only the end of the cantilever is heated and the lever is coated along its whole length. Equation 7.3.1 still remains adequate in our case because the main contribution comes from the much thicker silicon.

$$\tau_{ph} = \frac{l^2 \sum c_i t_i}{2 \sum K_i t_i} \tag{7.3.2}$$

Here, l is defined as the length of the cantilever, c_i is the heat capacity, K_i is the thermal conductivity and t_i is the thickness of each material [181, 182]. With these additional parameters in mind, the photo-thermal force gives rise to much longer characteristic response times. The numerical estimates for τ_{ph} at three different temperatures are given in table 7.1.

Temperatures (K)	τ_{ph} (s)
293	330×10^{-6}
77	10×10^{-6}
4	$> 8 \times 10^{-9}$

Table 7.1: The photothermal characteristic response time τ_{ph} is temperature dependent and becomes shorter the lower the base temperature gets.

At 4K its value is still nearly three orders of magnitude larger than τ_{rp}=26ps. In our system and similar ones, retardation (damping or amplification) is due to the photothermal effect and appear to be much larger than for radiation pressure, independent of the operating temperature [183, 176, 179]. But the expected value of τ_{ph} at 4K is probably much higher, because the thermal conductivities are then reduced by scattering at film boundaries and defects [184].

7.3.2 Noise-Driven Fundamental Resonance of a Hard Cantilever

As previously mentioned in section 5.2.3, during calibration one operation point on either side of an interference dip can be selected. Figure 7.1 shows the two possible operation points OP1 and OP2. Due to the peak asymmetry, the operation point on the steep side is commonly picked because of the higher sensitivity. Furthermore, enhanced damping is expected on the left side of the interference dip. In fact we found that feedback regulation at the setpoint, OP2 behaves in a stable manner. The effect of the photon-induced forces on the fundamental resonance peak of a cantilever (k=26.6N/m, f_0=285kHz) is readily apparent in figure 7.2. Noise spectra recorded at both operation points are depicted on each graph. With increasing laser power, the resonance peak at OP2 gets smaller and broader, demonstrating that damping or cooling (blue curve) gets stronger. On the contrary, the resonance peak at OP1 gets higher and narrower, indicating that noise-driven oscillation gets amplified or heated (red curve). This am-

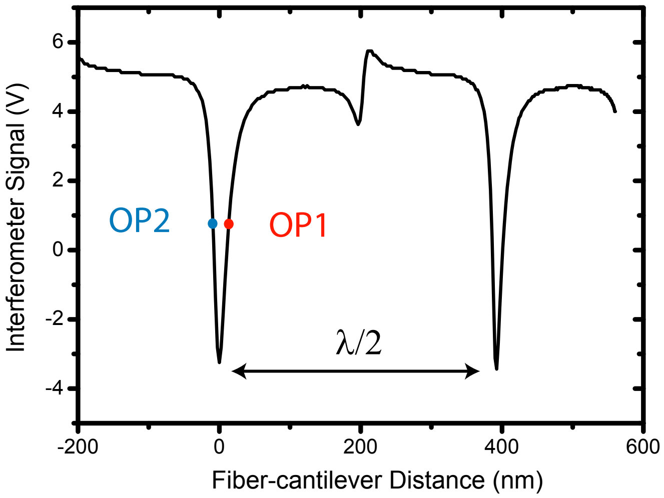

Figure 7.1: The operation points OP1 and OP2 indicate the steepest slope on either side of the interference dip. The inverse of the slope gives the sensitivity in nm/V.

plification can be driven above a particular threshold, where the cantilever's motion enters into an unstable, nonlinear regime where the oscillation amplitude first grows, then settles to a large value of the order of $\lambda/4$. This prevents control of the amplitude, which is in fact desirable in measurements of tip-induced energy dissipation [185]. These data demonstrate that interferometric deflecting detectors used in low temperature setups considerably affect the motion of hard, high Q cantilevers, typically used for non-contact measurements with atomic resolution in UHV, as confirmed by Hölscher et al [186].

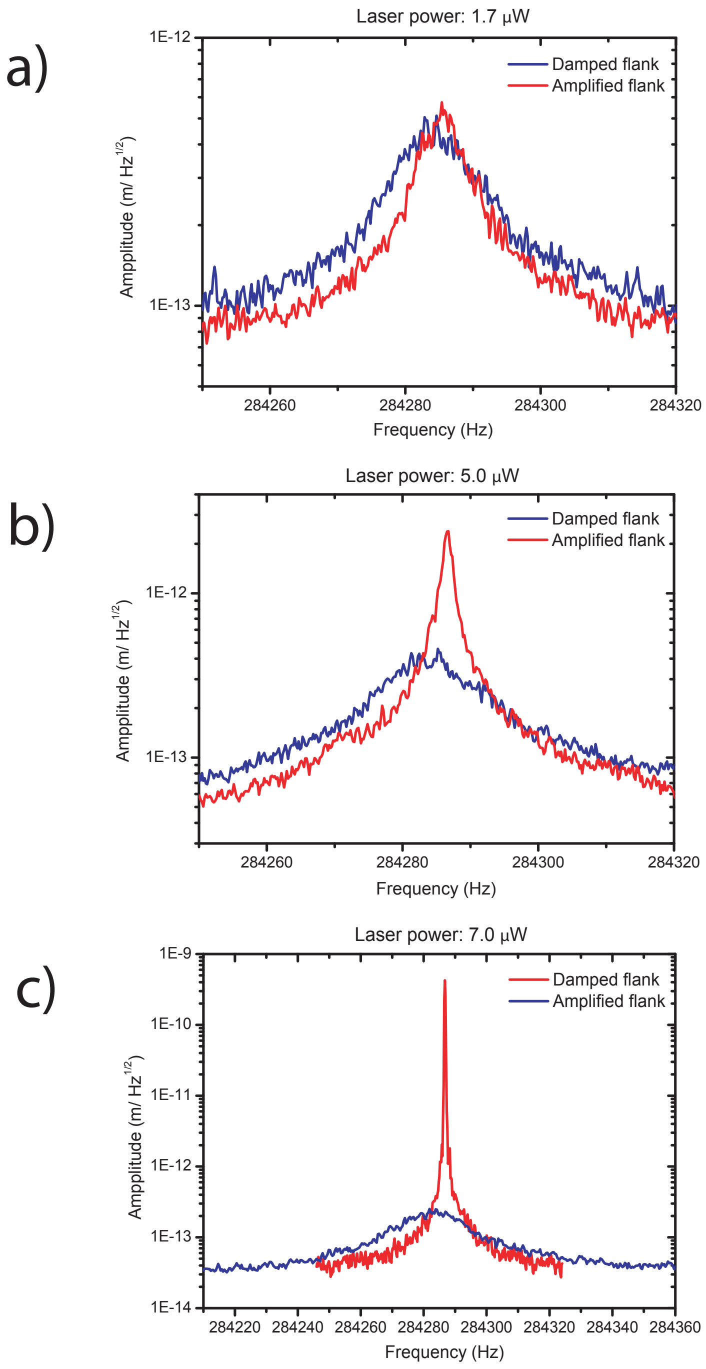

Figure 7.2: Measured noise spectra in the vicinity of the fundamental resonance of a hard cantilever (k=26.6N/m, f_0=285kHz) at 4.5K. a) At low laser power, the peak amplitude at both operation points are nearly equal. b) At 5μW a notable difference can be observed, the red curve is sharper and narrower whereas the blue curve is depressed and broader. c) At a higher laser power, the contrast between the two curves is very clear.

7.3.3 Effective Mode Temperature

The amplitude and width of the resonance peak are strongly dependent on the laser power. The strength of this effect can be related to the mean kinetic energy stored in the resonance mode, which is proportional to the area under the corresponding power spectral density (PSD) peak (the square of the root mean square amplitude of the noise-driven cantilever which is displayed in figure 7.3). In true thermal equilibrium (laser off), this means kinetic energy $1/2kz_{rms}^2$ is equal to $1/2k_BT$, where T being the actual temperature. According to the equipartition theorem (laser on), the kinetic energy of a particular mode derives from equipartition, but is commonly known as the effective mode temperature T_{eff}. Furthermore, according to Parseval's spectral theorem,

$$z_{rms}^2 = \int z^2(f)df \tag{7.3.3}$$

The mode kinetic energy is proportional to the area under the resonance curve in the noise power spectrum, as depicted in figure 7.3, and the mode temperature is calculated from,

$$k \int z^2(f)df = k_BT_{eff} \tag{7.3.4}$$

The definition makes sense if each mode is treated as a single damped harmonic oscillator, that is for small amplitude oscillations and non-overlapping (high Q) modes. Then, temperatures shown by Hohberger et al [187],

$$\frac{T_{eff}}{T} \approx \frac{\Gamma}{\Gamma_{eff}} = \frac{Q_{eff}}{Q} \tag{7.3.5}$$

only when $f_0 \approx f_{eff}$ being the optically modified resonance frequency, f_0 is the eigenfrequency, Γ the intrinsic damping rate of the mode and Γ_{eff} accounts for the optically modified damping rate. Note that the laser-induced effects are more pronounced for the fundamental bending mode because its stiffness is equal to the static stiffness k within a few percent, whereas it is much larger for the higher modes [50].

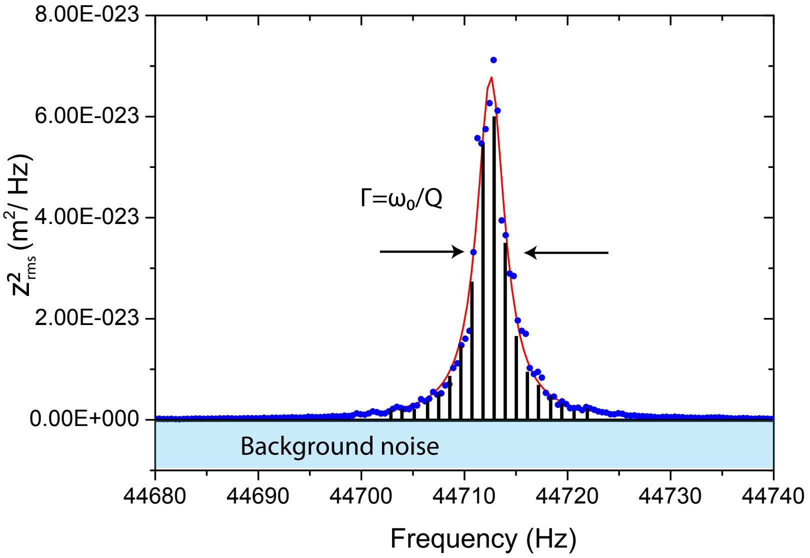

Figure 7.3: The integrated area under the filtered Lorentzian resonance curve minus the background noise reveals the stored kinetic energy, which together with the mode stiffness defines the effective temperature of the cantilever oscillation in a particular mode.

7.3.4 Passive Cooling

Previously, the cooling of a cantilever fundamental mode was explained. Damping control has been achieved earlier with an active feedback loop. This so-called force feedback regulation or ”Q-control” was described by Mertz et al [176]. Optimized control of cantilevers was outlined by Garbini et al [188]. They also compared soft and ultrasoft cantilevers to demonstrate optimal control of the force response [189]. Others have used similar feedback control to cool cantilevers to a few mK [179, 190]. In 2004 Höhberger and Karrai demonstrated passive cooling of the fundamental mode of a soft cantilever from room temperature to 18K. This passive cooling was achieved without feedback control using optical backaction effects only [187]. Similarly, Naik et al cooled the mode of a nanomechanical resonator from 550mK to 300mK [191]. Since then, several groups have published works on the possibility of enhanced force detection sensitivity [183]. However, this is based on the assumption that a high quality factor can still be obtained. Can macroscopic objects such as a cantilever be actually cooled? If yes, could they be cooled to the quantum limit, where $kz^2_{rms}=\hbar\omega_0$?

7.4 Experimental Results

To further quantify light-induced effects in our setup, we present results of measurements performed at three different bath temperatures on the damped side of the interference dip. A commercial MFM cantilever with a spring constant of $k = 0.59$N/m (f_0=45kHz) was used. The backside of the Silicon cantilever is coated with a 20nm gold layer, 1/3 towards its free end.

7.4.1 Noise Spectra

Starting with 1μW, the laser power was slowly increased up to 770μW. The laser power was measured with an integrating sphere (power meter) at the fiber interlink before entering the vacuum side. The actual power behind the lenses measured in the absence of the cantilever is 1/10 of P_{in}, where P_{in} is defined as the laser power before it enters the optical fiber of the LT-SPM. The cooling achieved with the first two bath temperatures is quantified in terms of T_{eff} for each P_{in} value.

Room Temperature

At the smallest laser power of 1μW, the resonance peak is minutely affected. As the laser power increases, the resonance peak gets increasingly suppressed and broadens. At the maximum laser power of 770μW, the damping effect on the cantilever is the strongest, and the resonance peak is affected the most (green curve). See figure 7.4(a).

Liquid Nitrogen Temperature

The measurement was repeated at a bath temperature of 77K. Similar trends are observed here. With increasing laser power, a 5Hz negative shift of the cantilever's resonance frequency was found. See figure 7.4(b)

Liquid Helium Temperature

At this lowest temperature the cooling effect was so strong that the mode temperature peak could not be determined. No useful results could be recorded, because the resonance peak was suppressed below the noise level.

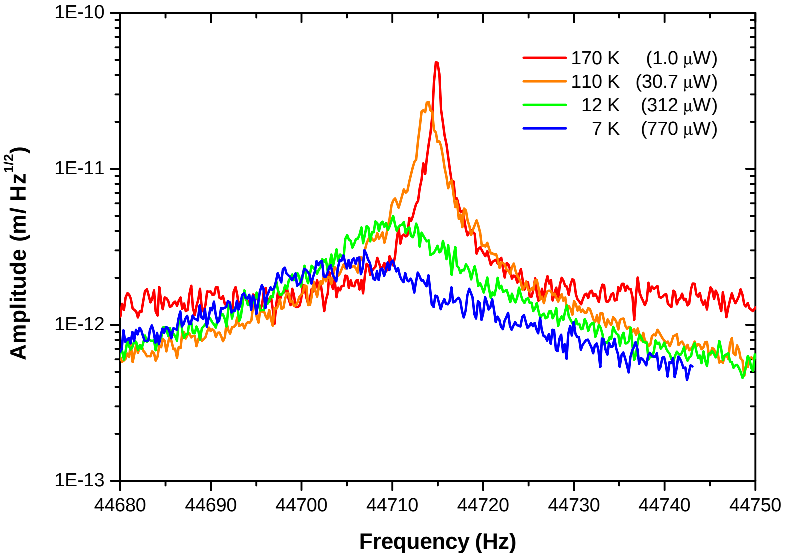

(a) Room temperature measurement

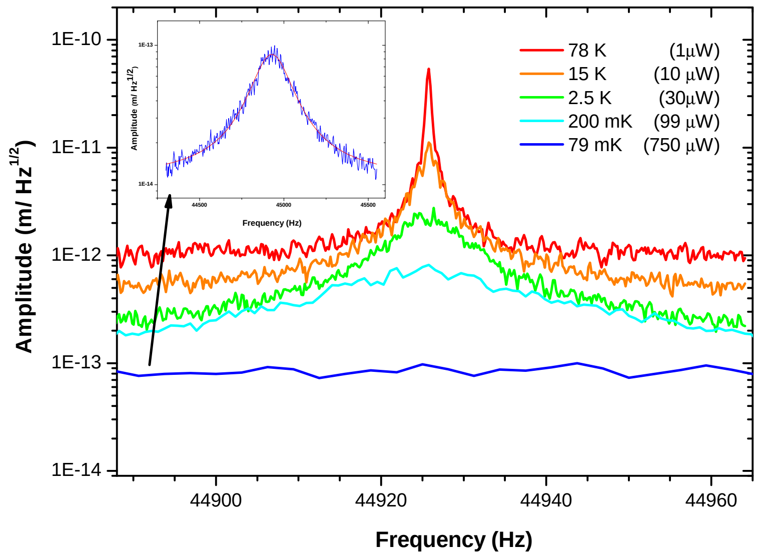

(b) Liquid nitrogen temperature measurement

Figure 7.4: RMS amplitude noise spectra around the fundamental cantilever resonance frequency. Inset: the purple resonance curve is shown on a different scale. The mode temperatures achieved are indicated for each laser power.

Observation of Frequency Shift

A small negative shift of the resonance frequency by ≈10Hz with increasing laser power can be observed in figure 7.4(a). The extracted equation 7.4.1 from the work of Hoehberger et al [187] shows that all light modified spring constants (k_{rp} and k_{ph}) contribute to the shift of the cantilever resonance frequency. ω_{eff} signifies the optically altered resonance frequency, ω_0 is the eigenfrequency - ,and k is the intrinsic spring constant of the cantilever.

$$\omega_{eff}^2 = \omega_0^2\Big(\frac{(k_{rp}/k)}{(\omega_0\tau_{rp})^2+1} + \frac{(k_{ph}/k)}{(\omega_0\tau_{ph})^2+1} + 1\Big) \tag{7.4.1}$$

The radiation pressure contribution is governed by the first term and the second term represents the photothermal effect. Since τ_{rp} is not affected by the base temperature, the first term remains constant. Furthermore, it is negligible because $k_{rp} \ll k$ and $\omega_0\tau_{rp} \gg 1$. In contrast, τ_{ph} varies with the base temperature but is also small if $\omega_0\tau_{ph} \gg 1$, which is in the case at room and liquid nitrogen temperature. Estimates of the $(\omega_0\tau_{ph}+1)^2$ term in the denominator for different base temperatures are shown in table 7.2. Measurements taken at room temperature show that the denominator $(\omega_0\tau_{ph}+1)^2 \approx 8650$, which reduces the photothermal contribution to practically zero. Data collected at 77K reveal $(\omega_0\tau_{ph}+1)^2 \approx 9$ and indicate that the second term of equation 7.4.1 should not be fully neglected because $(\omega_0\tau_{ph}+1)^2$ is not much greater than 1.

Temperatures (K)	τ_{ph} (s)	$(\omega_0\tau_{ph})^2+1$
293	330×10^{-6}	8650
77	10×10^{-6}	9
4	8×10^{-9}	1

Table 7.2: The table shows the numerical results of $(\omega_0\tau_{ph}+1)^2$ estimated for three different base temperatures.

7.4.2 Effective Mode Temperature and Q-factor

Recently, some groups have suggested that mode cooling could improve the force detection sensitivity of SFM [192, 187, 178]. This will only be true, if the quality factor remained constant. In the present LT-SFM the dominant cooling force is based on the photothermal effect and the contribution of radiation pressure is negligible. From the equation for the minimal detectable force gradient [175],

$$\frac{\partial F}{\partial z} = \frac{1}{A}\sqrt{\frac{4k_B T k BW}{\omega_0 Q}} \tag{7.4.2}$$

the force sensitivity can only be improved if the mode temperature T_{eff} decreases stronger than the modified Q-factor Q_{eff}. Figure 7.5 shows that with increasing laser power P_0, $1/T_{eff}$ grows linearly. From the full width half maximum (FWHM) Γ of the noise power spectra (see section 7.4.1), the modified mode quality factor Q_{eff} was independently obtained from,

$$Q = \frac{\omega_0}{\Gamma} \tag{7.4.3}$$

Starting from room temperature, the cantilever already experiences a strong cooling effect at the lowest laser power (1μW). This explains why the effective temperature starts with 170K. A final mode temperature of 6.7K could be reached, which demonstrates a cooling factor of 47. In a similar way, the mode Q-factor decreases from 57'400 to 2'530.
For comparison, the measurement was repeated at liquid nitrogen temperature. Corresponding results are also depicted in figure 7.5. Starting at 78K, a final mode temperature of 79mK could be obtained. A cooling factor of 975 and a reduction of the Q-factor Q_{eff} from 120'000 to 270 were determined. Finally, the relation between effective temperatures T_{eff} and quality factor Q_{eff} can be checked. We find

$$\frac{T_{eff}}{T} \cong \frac{Q_{eff}}{Q} \tag{7.4.4}$$

In this case Q_{eff} and T_{eff} represent the mode Q-factor, respectively the mode temperature. Q is the intrinsic Q-factor and T the bath temperature of the object of investigation. Therefore, from equation 7.4.4, the conclusion can be drawn that mode cooling cannot improve the force detection sensitivity, because Q_{eff} decreases proportionally with T_{eff}.

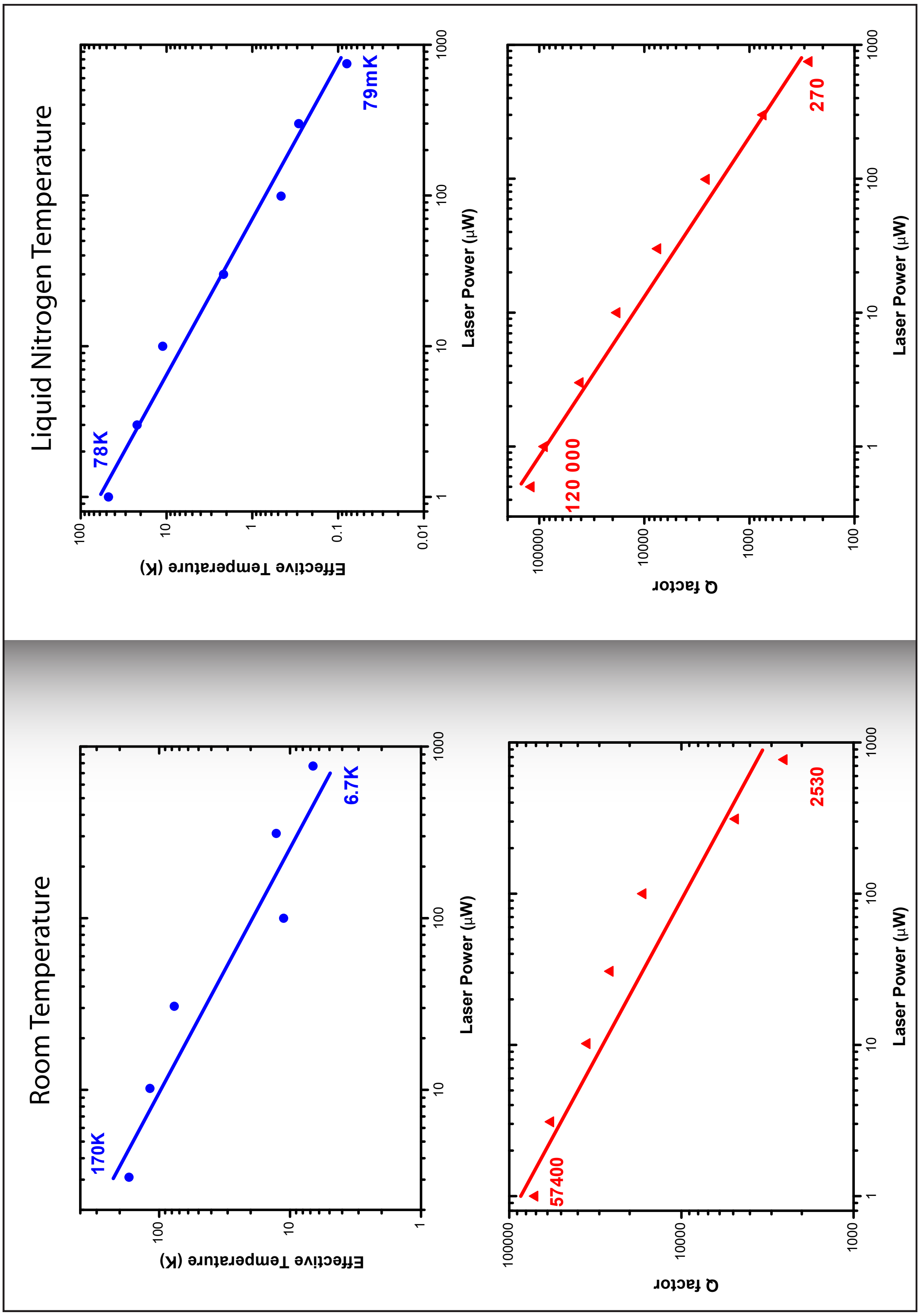

Figure 7.5: Correlation between effective mode temperature and Q-factor: (a) at room temperature. (b) at liquid nitrogen temperature.

7.4.3 Summary of Cooling Experiments

With a commercial gold coated cantilever (0.59N/m, fo=45kHz), the mode cooling effect was investigated. The outcome of the cantilever cooling experiments shows that:

- The degree of mechanical mode cooling of the cantilever strongly depends on the laser power.
- Cantilever cooling started with the initial temperature of T_i=300K. With a cooling factor of 47, a final mode temperature of T_f=6.7K could be reached.
- Cantilever cooling measurement was performed at liquid nitrogen temperature with T_i=77K. As the final mode temperature of the cantilever of T_f=79mK could be obtained and a cooling factor of 975 was estimated.
- Measurements at liquid helium temperature T_i=4.3K were attempted. However, no T_f could be determined because the resonance peak was suppressed below the noise level, indicating the presence of a very strong cooling effect.
- Furthermore, the cooling mechanism in this low temperature system is dominated by the photothermal effects. The mode cooling of the cantilever should result to no enhancement of the force detection sensitivity for a given base temperature. This is described through the correlation between the mode temperature and the mode Q-factor as:

  $$\frac{T_{eff}}{T} \cong \frac{Q_{eff}}{Q}$$

- A shift in the cantilever resonance frequency at room temperature and at 77K was observed.

7.5 Laser-induced Effects on Calibration

The previously discussed photon-induced effects on the cantilever properties also complicate the calibration of the interferometer. This is because the photon-induced forces lead to a time-dependent cantilever deflection that affects the interferometer's response differently during calibration and measurement.

7.5.1 Asymmetry Issue

As implied in section 5.2.3, the response of the interferometer to a cantilever deflection could be calibrated. This is done by recording the interferometer's response to an oscillatory change of the cavity length. The slope of the response curve of the selected operation point (OP) is then equal to the inverse of the sensitivity, provided that the cantilever did not deflect at any point in time during the acquisition of the calibration data (see figure 7.1). The assumption is however not valid in most cases, because photothermal forces lead to a time-dependent cantilever deflection. Thus depending on the cavity length, the photothermal forces will move the cantilever to or away from the optics such that the response signal as a function of the cavity length will be distorted. More specifically, the left and right slope of the interference dips will have different values. The measured slopes at selected OP however correctly represent the inverse of the sensitivity of the OP, but only for low frequency deflection signals.

7.5.2 Average Sensitivity Technique

For higher frequency deflection signals, the cantilever deflection in a specific light field will not fully equilibrate and therefore become smaller. Then, a calibration performed at low frequency (5-10Hz) does not hold for the cantilever oscillation on its resonance. Unfortunately, the limited resonance frequency of the W-piezo restricts the oscillation of the cavity length beyond 4kHz, which is required a calibration at higher frequencies. To overcome this issue and to perform a calibration at higher frequencies, we excited the cantilever with an oscillatory electric field applied between the tip and the sample, at frequencies ranging from 10 Hz to 100kHz (see figure 7.6).
The measured resonance of the interferometer (maxima of blue curves) then correspond to the slope of the interference peak (black curves), as shown in figure 7.6. As expected the slopes measured at OP1 and OP2 become equal at sufficiently high frequencies, as plotted in figure 7.7). We further

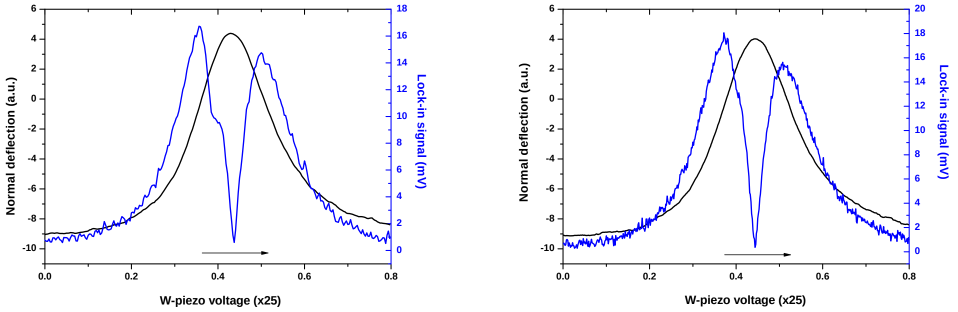

(a) 10Hz

(b) 10kHz

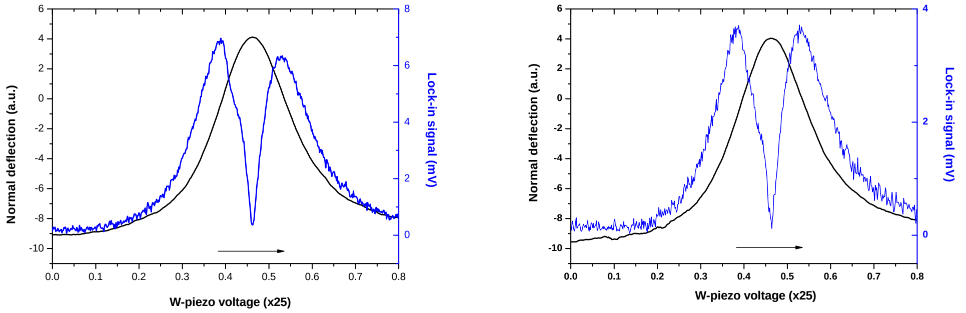

(c) 80kHz

(d) 100kHz

Figure 7.6: Lock-in detection of cantilever electrostatic dithering. The black curves represent the interference peak and the maxima of the blue curves correspond to the slopes. As the dithering frequency increases from 10Hz to 10kHz, 80kHz and 100kHz, the slopes become equal to each other. Parameters (P=80μW, slow sweep 200s).

conclude that the average of the two slopes remain roughly constant at the value representing the high frequency calibration. The average between the two slopes thus could be used as a high frequency calibration value valid at the cantilever's resonance frerquency.

Here, the slopes of OP1 and OP2 are in units of V/m. Because the sensitivity (m/V) is the inverse of the slope value, the following equation is used to compute the average sensitivity.

$$S_{average} = \frac{1}{2}\Big(\frac{1}{OP1} + \frac{1}{OP2}\Big) \tag{7.5.1}$$

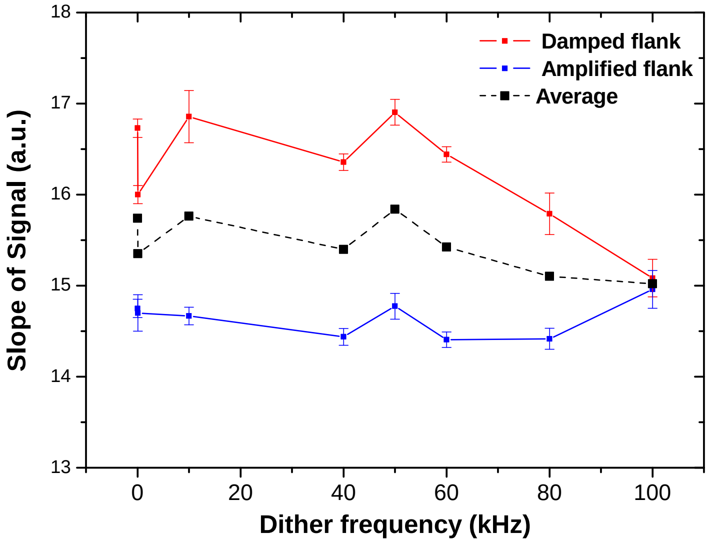

Figure 7.7: Cantilever dithering experiment: laser power versus frequency plot shows that the slopes of OP1 and OP2 steadily converge at a dither frequency of 100kHz.

7.6 Chapter Summary

In this chapter, the analogy between to atom cooling cantilever cooling is introduced and the basic concepts of cantilever cooling are presented. Cavity cooling experiments confirmed the presence of photon-induced effects on the cantilever, which may affect the interferometer calibration. Two types of photon-induced forces are introduced in section 7.3.1. From the characteristic response times τ_{rp} and τ_{ph}, the relative contribution of radiation pressure was estimated. In our case, the radiation pressure is base temperature independent and its force contribution is negligible. In comparison, the forces from the photothermal effects are base temperature dependent and become dominant when the cantilever absorbs parts of the incident laser light. This leads to differential thermal expansion between the gold coating and the silicon cantilever. Table 7.1 gives an overview of the τ_{rp} values at different base temperatures.

Experimental data show the mode cooling of an MFM soft cantilever (0.59N/m, f_0=45kHz) at three different base temperatures. A detection sensitivity improvement is not likely, because Q_{eff} decreases proportional to the decreasing mode temperature T_{eff}.

Laser-induced effects have a strong impact on the calibration of the interferometer, as observed by the asymmetry of the interference dips. Measurements were done to verify the frequency dependence of the fFPi calibration. The consequence of the distorted interference dips affects the sensitivities at the working points OP1 and OP2, which leads to an incorrect amplitude reading in the detection electronics. Electrostatic actuation of the cantilever up to 100kHz has shown that both slopes of the interference dip converge to an average value near the cantilever resonance frequency. This finding was proposed as the solution to include the effects of the photon-induced forces for the low frequency (DC) calibration is by taking the average value of the sensitivities at OP1 and OP2.

Part V

Epilogue

Chapter 8

Summary and Outlook

A new type of LT-SPM system in UHV operating at three different temperatures was developed and constructed.
Low temperature operation presents advantages for reactive sample surfaces which remain clean over several days, permitting stable operation conditions for long time experiments. Low drift and creep rates are further conveniences. Moreover, site specific positioning of the probing tip is an absolute requirement in STS. For example in STM, Spin flip [193] and molecular vibrational states processes [10] can only performed at low temperature.
Also at low temperature the intrinsic noise of the cantilever is minimized, resulting in a smaller minimum measurable force. The minimum detectable force gradients improve with larger oscillation amplitude. But this does not necessarily lead to a better signal to noise ratio, because the cantilever tip does not remain in the force field of the sample if the oscillation amplitude is larger than the decay length of the force. This is around 2-3Å for a minimal vertical noise [24]. To obtain a higher force sensitivity, ultrasmall cantilevers with small oscillating amplitudes should be employed. From the thermodynamical limits, the sensitivities of the noise can only be reduced if all noise sources such as that of the deflection sensor, tip-sample gap and control system are sufficiently small. For the deflection sensor, this implies that the noise in a typical measurement bandwidth of $B = 1000Hz$ should be smaller than 10fm/$\sqrt{Hz}$ (see chapter 1). To achieve the required detection sensitivity, the implementation of the fPFi in the LT-SPM system was done. Chapter 5 shows the performance tests, calibration, and characterization of the interferometer at room temperature, liquid nitrogen and liquid Helium environment.

Chapter 4 presents further development and improvements of the NanoScan hr-MFM control system to accommodate new operation conditions in the LT-SPM system. These requirements are stable measurement conditions in STM, dynamic AFM measurement modes with small oscillation amplitudes, which provide the basis for simultaneous nc-AFM/STM operations. From the noise analysis, the electronic control system contributes a vertical displacement of 2.2pm peak-peak at 4.5K.

Chapter 6: data on HOPG and Si(111)7x7 acquired with the prototype LT-SPM system strongly indicated a tip-sample gap instability. Noise and tunnel current spectra show low frequency peaks at 480Hz and 710Hz, which enabled the identification of the noise source. Improvement and modification of the sample positioning unit were accomplished. Subsequent tests concluded an improved and consistent topographic line profile recorded with STM at 77K. Additional STM data enabled the characterization of the LT-SPM system. Fail-safe tests such as constant height and large area scans were conducted.
With a hard cantilever (40N/m) on the fundamental and first oscillation mode, nc-AFM results were acquired at 4.5K. Two cantilever excitation schemes were successfully tested. STM measurements show results on Si(111)7x7 with a platinum tip coated cantilever. Further measurements with the MD-SPM system recorded data with a tunneling cantilever. A consistent average corrugation height of 13pm was determined.

In chapter 7, cavity cooling experiments confirmed the presence of photon-induced effects on the cantilever, which may affect the interferometer calibration. Two types of photon-induced forces are introduced in chapter 7. From the characteristic response times, the relative contribution of radiation pressure and the forces arising from the photothermal effects was estimated. In our setup, the contribution of the radiation pressure is negligible. In contrast, the forces from the photothermal effects are base temperature dependent and become dominant when the cantilever absorbs parts of the incident light. This leads to differential thermal expansion between the gold coating and the silicon cantilever. Continuing works will include absolute estimates of these forces.
Experimental data show that the mode cooling of an MFM soft cantilever (0.59N/m, f_0=45kHz) at three different base temperatures is possible. In addition, the detection sensitivity does not improve because Q_{eff} decreases in proportion to the decreasing mode temperature T_{eff}.
Laser-induced effects have a striking impact on the calibration of the interferometer. A direct observation of the influence through the photon-induced effects can be demonstrated by the asymmetry of the interference dips. Measurements were done to verify the frequency dependence of the fFPi

calibration. The consequence of the distorted interference dips affects the sensitivities at the working points OP1 and OP2, which results to an incorrect amplitude interpretation in the control electronics. One proposed solution to include the effects of the photon-induced forces for the low frequency (DC) calibration is by taking the average value of the measured sensitivity.

Future upgrades of the LT-SPM system include (1) a new type of bath cryostat, which will reduce the LN2 consumption rate[1]. (2) The new optical lens system with corrected chromatic abberation allows interferometric detection and cantilever photothermal actuation. (3) The last major upgrade involves a newly designed and improved sample positioning unit with lateral XY piezo motors, which will eventually eliminate the tip-sample gap instability.
Following the system upgrades, the next key experiments will be nc-AFM imaging with both detection schemes to review their performance in the cantilever's fundamental and second mode with various cantilever oscillating amplitudes ranging from 5nm to 0.01nm. Furthermore, simultaneous detection of the flexural and torsional modes are possible with this type of interferometer, which provides direct access to vertical and lateral forces.
Accurate analysis of atomic and molecular scale manipulation, diffusion and bond formation studies require a more complete picture of the nature of the interatomic forces. Because simultaneous nc-AFM/STM measurements can provide an increased number of channels per scanned image, tunnel current as well as force information will be made available to better understand the origin of these forces.

---

[1] Already installed in the MD-SPM system. See under www.createc.de

Acronyms

Microscopy

AFM:	Atomic Force Microscopy
AM-AFM:	Amplitude Modulation Atomic Force Microscopy
FM-AFM:	Frequency Modulation Atomic Force Microscopy
nc-AFM:	non-contact Atomic Force Microscopy
CITS:	Current Imaging Tunneling Spectroscopy
FIM:	Field Ion Microscopy
LDOS:	Local Density Of States
LEED:	Low Energy Electron Diffraction
MFM:	Magnetic Force Microscopy
hrMFM:	high-resolution Magnetic Force Microscopy
SFM:	Scanning Force Microscopy
SPM:	Scanning Probe Microscopy
LT-SPM:	Low Temperature Scanning Probe Microscope
MD-SPM:	Multi Dimensional Scanning Probe Microscope
SEM:	Scanning Electron Microscopy
STM:	Scanning Tunneling Microscopy
STS:	Scanning Tunneling Spectroscopy
TEM:	Transmission Electron Microscopy
UHV:	Ultra High Vacuum

Control Electronics

AC:	Alternating Current
ALI:	Analog Lock-In
ADC:	Analog Digital Converter
BOB:	Break Out Box
BOC:	Break Out Card
DAC:	Digital Analog Converter
DC:	Direct Current

DCO: Digitally Controlled Oscillator
DIO: Digital Input Output
FPGA: Field Programmable Gate Array
FPi: Fabry-Perot interferometer
fFPi: focusing Fabry-Perot interferometer
HVA: High Voltage Amplifier
PCI: Peripheral Component Interconnect
PLL: Phase Locked Loop
PMC: Piezo Motor Controller
PXI: PCI eXtensions for Instrumentation
rms: root mean square
RTC: Real-Time Controller
SE: Self-Excitation
VCO: Voltage Controlled Oscillator

Materials

Au: Gold
Cu: Copper
DNA: Deoxyribo Nucleic Acid
HOPG: Highly Oriented Pyrolytic Graphite
Ir: Iridium
Mo: Molybdenum
Ni: Nickel
OFHC: Oxygen Free High thermal Conductivity
Pt: Platinum
Si: Silicon
Ta: Tantalum
Ti: Titan
W: Tungsten

Bibliography

[1] Kölle. *Tesla's verschollene Erfindungen.* VAP-Verlag, 3rd edition, 2003.

[2] R. A. Serway and R. J. Beichner. *Physics.* Saunders College Publishing, 5th edition, 2000.

[3] D. C. Giancoli. *Physik.* Prentice Hall, Inc., 3rd edition, 2006.

[4] L. E. C. van de Leemput and H. van Kempen. *Reports on Progress in Physics*, 55:1165, 1992.

[5] J. A. Kubby and J. J. Boland. Scanning tunneling microscopy of semiconductor surfaces. *Surface Science Reports*, 26:61, 1996.

[6] F. Besenbacher. Scanning tunneling microscopy studies of metal surfaces. *Reports on Progress in Physics*, 59:1737, 1996.

[7] R. S. Becker, J. A. Golovchenko, and B. S. Swartzentruber. Electron interferometry at crystal surfaces. *Phys. Rev. Lett.*, 55(9):987–990, Aug 1985.

[8] G. Binnig, K. H. Frank, H. Fuchs, N. Garcia, B. Reihl, H. Rohrer, F. Salvan, and A. R. Williams. Tunneling spectroscopy and inverse photoemission: Image and field states. *Phys. Rev. Lett.*, 55(9):991–994, Aug 1985.

[9] R. M. Feenstra, J. A. Stroscio, and A. P. Fein. Tunneling spectroscopy of the si(111)2x1 surface. *Surface Science*, 181:295, 1987.

[10] B. C. Stipe, M. A. Rezaei, and W. Ho. Single-molecule vibrational spectroscopy and microscopy. *Science*, 280:1732, 1998.

[11] M. F. Crommie, C. P. Lutz, and D. M. Eigler. Imaging standing waves in a two-dimensional electron gas. *Nature*, 363:524, 1993.

[12] J. M. Soler, A. M. Baro, N. Garcia, and H. Rohrer. Interatomic forces in scanning tunneling microscopy: Giant corrugations of the graphite surface. *Physical Review Letters*, 57:444, 1986.

[13] D. M. Eigler and E. K. Schweizer. Positioning single atoms with a scanning tunneling microscope. *Nature*, 344:524, 1989.

[14] G. Binnig and C. F. Quate. Atomic force microscope. *PRL*, 56:730, 1986.

[15] E. Meyer, R. Overney, D. Brodeck, L. Howald, J. Lüthi, R. Frommer, and H. J. Güntherodt. Friction and wear of langmuir-blodgett films observed by friction force microscopy. *Physical Review Letters*, 69:1777, 1992.

[16] F. F. Abraham, I. P. Batra, and S. Ciraci. Effect of tip profile on atomic-force microscope images: A model study. *Physical Review Letters*, 60:1314, 1988.

[17] E. Heinzelmann, H. Meyer, D. Brodeck, G. Overney, and H. J. Güntherodt. *Zeitschrift für Physik B*, 88:321, 1992.

[18] F. J. Giessibl and G. Binnig. *Ultramicroscopy*, 42-44:281, 1992.

[19] F. Ohnesorge and G. Binnig. True atomic resolution by atomic force microscopy through repulsive and attractive forces. *Science*, 260:1451, 1993.

[20] S. Kitamura and M. Iwatsuki. Observation of 7x7 reconstructed structure on the silicon (111) surface using ultrahigh vacuum noncontact atomic force microscopy. *Jpn. J. Appl. Phys.*, 34:L145, 1995.

[21] F. J. Giessibl. Atomic resolution of the silicon (111)-(7x7) surface by atomic force microscopy. *Science*, 267:68, 1995.

[22] M. A. Lantz, H. J. Hug, R. Hoffmann, P. J. van Schendel, P. Kappenberger, S. Martin, A. Baratoff, and H. J. Güntherodt. Quantitative measurement of short-range chemical bonding forces. *Science*, 291:2580, 2001.

[23] M. A. Lantz, H. J. Hug, R. Hoffmann, S. Martin, A. Baratoff, and H. J. Güntherodt. Short-range electrostatic interactions in atomic-resolution scanning force microscopy on the si(111)7x7 surface. *Physical Review B*, 68:035324, 2003.

[24] F. J. Giessibl. Advances in atomic force microscopy. *Review of Modern Physics*, 75:949, 2003.

[25] E. Meyer, H. J. Hug, and R. Bennewitz. *Scanning Probe Microscopy.* Springer, Heidelberg, 2004.

[26] S. Kawai, S. Kitamura, D. Kobayashi, S. Meguro, and H. Kawakatsu. An ultrasmall amplitude operation of dynamic force microscopy with second flexural mode. *Applied Physics Letters*, 86:193107, 2005.

[27] A. Oral, R. A. Grimble, H. Ö. Özer, and J. B. Pethica. High-sensitivity noncontact atomic force microscope/ scanning tunneling microscope (nc afm/stm) operating at subangstrom oscillation amplitudes for atomic resolution imaging and force spectroscopy. *Review of Scientific Instruments*, 74:3656, 2003.

[28] D. Rugar, B. C. Stipe, H. J. Mamin, C. S. Yannoni, T. D. Stowe, K. Y. Yasumura, and T. W. Kenny. Adventures in attonewton force detection. *Applied Physics A*, 72:S3, 2001.

[29] D. Rugar, R. Budakian, H. J. Mamin, and B. W. Chui. Single spin detection by magnetic resonance force microscopy. *Nature*, 430:329, 2004.

[30] F. J. Giessibl, S. Hembacher, Ch. Herz, M. Schiller, and J. Mannhart. Stability considerations and implementation of cantilevers allowing dynamic force microscopy with optimal resolution: the qplus sensor. *Nanotechnology*, 15:S79, 2004.

[31] T. and Fukuma. Wideband low-noise optical beam deflection sensor with photothermal excitation for liquid-environment atomic force microscopy. *Review of Scientific Instruments*, 80:023707, 2009.

[32] T. Fukuma. True atomic resolution in liquid by frequency-modulation atomic force microscopy. *Applied Physics Letters*, 87:034101, 2005.

[33] N. Umeda, S. Ishizaki, and H. Uwai. Scanning attractive force microscope using photothermal vibration. *Journal of Vacuum Science and Technology B*, 9:1318, 1991.

[34] G. Binnig, H. Rohrer, Ch. Gerber, and E. Weibel. Tunneling through a controllable vacuum gap. *APL*, 40:178, 1982.

[35] E. W. Mueller. Das feldionenmikroskop. *Zeitschrift für Physik*, 131:136, 1951.

[36] E. W. Mueller. Field ion microscopy. *Science*, 149:591, 1965.

[37] J. A. Panitz. Field-ion microscopy - a review of basic principles and selected appplications. *Journal of Physics E: Scientific Instruments*, 15:1281, 1982.

[38] V. V. Mitin, D. I. Sementsov, and N. Z. Vagidov. *Quantum Mechanics for Nanostructures*. Cambridge University Press, 1st edition, 2010.

[39] P. W. Atkins. *Molecular Quantum Mechanics*. Oxford University Press, 2nd edition, 1983.

[40] F. J. Blatt. *Modern Physics*. McGraw-Hill, Inc., 1st edition, 1992.

[41] D. J. Griffith. *Introduction to Quantum Mechanics*. Prentice Hall, Inc., 1995.

[42] C. J. Chen. *Introduction to Scanning Tunneling Microscopy*. Oxford University Press, 1993.

[43] J. Bardeen. Tunneling from a many-partile point of view. *PRL*, 6:57, 1961.

[44] J. Tersoff and D. R. Hamann. Theory and application for the scanning tunneling microscope. *Phys. Rev. Lett.*, 50(25):1998–2001, Jun 1983.

[45] D. Sarid. *Scanning Force Microscopy*. Oxford University Press, Inc., New York, 1994.

[46] J. P. Cleveland and S. Manne. A nondestructive method for determining the spring constant of cantilevers for scanning force microscopy. *Review of Scientific Intruments*, 64:403, 1993.

[47] J. E. Sader, J. W. M. Chon, and P. Mulvaney. Calibration of rectangular atomic force microscope cantilevers. *RSI*, 70:3967, 1999.

[48] A. Torii, M. Sasaki, K. Hane, and S. Okuma. A method for determining the spring constant of cantilevers for atomic force microscopy. *Meas. Sci. Technol.*, 7:179, 1996.

[49] J. L. Hutter and J. Bechhoefer. Calibration of atomic-force microscope tips. *RSI*, 64:1868, 1993.

[50] U. Rabe, K. Janser, and W. Arnold. Vibrations of free and surface-coupled atomic force microscope cantilevers:theory and experiment. *RSI*, 67:3281, 1996.

[51] S. Timoshenko. *Vibration Problems In Engineering.* D. Van Nostrand Company, Inc., 2nd edition, 1937.

[52] O. Pfeiffer. *Quantitative dynamische Kraft- und Dissipationsmikroskopie auf molekularer Skala.* inaugural, University of Basel, 2004.

[53] M. Guggisberg, M. Bammerlin, C. Loppacher, O. Pfeiffer, A. Abdurixit, V. Barwich, R. Bennewitz, A. Baratoff, E. Meyer, and H. J. Güntherodt. Separation of interactions by noncontact force microscopy. *Physical Review B*, 61:11151, 2000.

[54] N. A Burnham, R. J. Colton, and H. M. Pollock. Work-function anisotropies as an origin of long-range surface forces. *Phys. Rev. Lett.*, 69:144, 1992.

[55] S. Sadewasser and M. Ch. Lux-Steiner. Correct height measurement in noncontact atomic force microscopy. *Phys. Rev. Lett.*, 91:266101, 2003.

[56] D. D. Ebbing and S. D. Gammon. *General Chemistry.* Houghton Mifflin Company, 6th edition, 1999.

[57] J. Israelachvili. *Intermolecular and Surface Forces.* Acamdemic Press, 2nd edition, 2006.

[58] H. C. Hamaker. *Physica*, 4:1058, 1937.

[59] R. Eisberg and R. Resnick. *Quantum Physics.* John Wiley & Sons, 2nd edition, 1985.

[60] R. Perez, M. C. Payne, I. Stich, and K. Terakura. Role of covalent tip-surface interactions in noncontact atomic force microscopy on reactive surfaces. *Physical Review Letters*, 78:678, 1997.

[61] M. Gauthier and M. Tsukada. Theory of noncontact dissipation force microscopy. *Physical Review B*, 60:11716, 1999.

[62] L. Kantorovich and C. Hobbs. Probing the si(111) surface with a si tip: An ab initio study. *Physical Review B*, 73:245420, 2006.

[63] W. Denk and D. W. Pohl. Local electrical dissipation imaged by scanning force microscopy. *Applied Physics Letters*, 59:2171, 1991.

[64] N. Sasaki and M. Tsukada. The relation between resonance curves and tip-surface interaction potential in noncontact atomic-force microscopy. *Japanese Journal of Applied Physics*, 37:L533, 1998.

[65] C. Loppacher, R. Bennewitz, O. Pfeiffer, M. Guggisberg, M. Bammerlin, S. Schär, V. Barwich, A. Baratoff, and E. Meyer. Experimental aspects of dissipation force microscopy. *Physical Review B*, 62:13674, 2000.

[66] S. Morita, R. Wiesendanger, and E. Meyer. *Noncontact Atomic Force Microscopy.* Springer, Heidelberg, 2002.

[67] J. E. Sader and S. P. Jarvis. Accurate formulas for interaction force and energy in frequency modulation force spectroscopy. *APL*, 84:1801, 2004.

[68] M. Guggisberg. *Lokale Messung von atomaren Kräften.* PhD thesis, University of Basel, 2000.

[69] J. N. Glosli. Friction at the atomic scale. *Fundamentals of Friction: Macroscopic and Microscopic Processes*, 220:427, 1992.

[70] N. Blanc, J. Brugger, N. F. de Rooij, and U. DÃ$\frac{1}{4}$rig. Scanning force microscopy in the dynamic mode using microfabricated capacitive sensors. *J. Vac. Sci. Technol. B*, 14:901, 1996.

[71] F. J. Giessibl and B. M. Trafas. Piezoresistive cantilevers utilized for scanning tunneling and scanning force microscopy in ultrahigh vacuum. *Review of Scientific Instruments*, 65:1923, 1994.

[72] S. C. Minne, S. R. Manalis, and C. F. Quate. Parallel atomic force microscopy using cantilevers with integrated piezoresistive sensors and integrated piezoelectric actuators. *Applied Physics Letters*, 67:3918, 1995.

[73] S. R. Manalis, S. C. Minne, and C. F. Quate. Atomic force microscopy for high speed imaging using cantilevers with and integrated actuator and sensor. *Applied Physics Letters*, 68:871, 1996.

[74] P. Güthner, U. Fischer, and K. Dransfeld. Scanning near-field acoustic microscopy. *Applied Physics B*, 48:89, 1989.

[75] B. J. Albers, M. Liebmann, T. C. Schwendemann, M. Z. Baykara, M. Heyde, M. Salmeron, E. I. Altman, and U. D. Schwarz. Combined low-temperature scanning tunneling/atomic force microscope for atomic resolution imaging and site-specific force spectroscopy. *Review of Scientific Intruments*, 79:033704, 2008.

[76] J. Rychen, T. Ihn, P. Studerus, A. Herrmann, and K. Ensslin. A low-temperature dynamic mode scanning force microscope operating in high magnetic fields. *RSI*, 70(6):2765, 1999.

[77] Y. Seo and W. Jhe. Atomic force microscopy and spectroscopy. *Reports on Progress in Physics*, 71:016101, 2008.

[78] Y. Martin, C. C. Williams, and H. K. Wickramasinghe. Atomic force microscope-force mapping and profiling on a sub 100-a scale. *Journal of Applied Physics*, 61:4723, 1987.

[79] G. Meyer and N. M. Amer. Novel optical approach to atomic force microscopy. *Applied Physics Letters*, 53:1045, 1988.

[80] O. Marti, J. Colchero, and J. Mlynek. Combined scanning force and friction microscopy of mica. *Nanotechnology*, 1:141, 1990.

[81] G. M. McClelland, R. Erlandsson, and S. Chiang. Atomic force microspcopy: general principles and a new implementation. *Review of Progress in Quantitative Nondestructive Evaluation*, page 1307, 1987.

[82] R Garcia and R. Perez. Dynamic atomic force microscopy methods. *Surface Science Reports*, 47:197, 2002.

[83] R. Perez, I. Stich, M. C. Payne, and K. Terakura. Surface-tip interactions in noncontact atomic-force microscopy on reactive surfaces: Si(111). *Physical Review B*, 58:10835, 1998.

[84] F. J. Giessibl, H. Bielefeldt, S. Hembacher, and J. Mannhart. Calculation of the optimal imaging parameters for frequency modulation atomic force microscopy. *Applied Surface Science*, 140:352, 1999.

[85] F. J. Giessibl, S. Hembacher, and J. Bielefeldt, H. Mannhart. Subatomic features on the silicon(111)-(7x7) surface observed by atomic force microscopy. *Science*, 289:422, 2000.

[86] L. Kantorovich and T. Trevethan. General theory of microscopic dynamical response in surface probe microscopy: From imaging to dissipation. *Physical Review Letters*, 93:236102, 2004.

[87] Y. Sugimoto, S. Innami, M. Abe, O. Custance, and S. Morita. Dynamic force spectroscopy using cantilever higher flexural modes. *Applied Physics Letters*, 91:093120, 2007.

[88] J. Melcher, S. Hu, and A. Raman. Equivalent point-mass models of continuous atomic force microscope probes. *Applied Physics Letters*, 91:053101, 2007.

[89] H. J. Hug, B. Stiefel, P. J. van Schendel, A. Moser, S. Martin, and H. J. Güntherodt. A low temperature ultrahigh vacuum scanning force microscope. *RSI*, 70(9):3625, 1999.

[90] H. J. Hug, A. Moser, Th. Jung, O. Fritz, A. Wadas, I. Parashikov, and H. J. Güntherodt. Low temperature magnetic force microscopy. *Review of Scientific Instruments*, 54:2920, 1993.

[91] R. Wiesendanger. *Scanning Probe Microscopy and Spectroscopy: Methods and Applications.* Cambridge University Press, 1994.

[92] M. A. Lantz, H. J. Hug, P. J. van Schendel, R. Hoffmann, S. Martin, A. Baratoff, A. Abdurixit, H. J. Güntherodt, and C. Gerber. Low temperature scanning force microscopy of the si(111) 7x7 surface. *Physical Review Letters*, 84:2642, 2000.

[93] M. Okano, K. Kajimura, S. Wakiyama, F. Sakai, W. Mizutani, and M. Ono. Vibration isolation for scannning tunneling microscopy. *Journal of Vacuum Science and Technology A*, 5:3313, 1987.

[94] J. A. Stroscio and W. J. Kaiser, editors. *Scanning Tunneling Microscopy.* Acamdemic Press, Inc., 1993.

[95] F. Pobell. *Matter and Methods at Low Temperatures.* Springer-Verlag, Berlin, 3rd edition, 2007.

[96] G. Binnig, H. Rohrer, Ch. Gerber, and E. Weibel. 7x7 reconstruction on si(111) resolved in real space. *Phys. Rev. Lett.*, 50(2):120–123, Jan 1983.

[97] D. J. Chadi. New adatom model for si(111)7x7 and si(111)-ge 5x5 reconstructed surfaces. *Physical Review B*, 30:4470, 1984.

[98] K. Takayanagi, Y. Tanishiro, M. Takagi, and S. Takahashi. Structural analysis of si(111)-7x7 by uhv-transmission electron diffraction and microscopy. *Journal of Vacuum Science and Technology A*, 3:1502, 1985.

[99] R. S. Becker, J. A. Golovchenko, E. G. McRae, and B. S. Swartzentruber. Tunneling images of atomic steps on the si(111)7x7 surface. *Physical Review Letters*, 55:2028, 1985.

[100] C. J. Chen. Electromechanical deflections of piezoelectric tubes with quartered electrodes. *Applied Physics Letters*, 60:132, 1991.

[101] G. Nunes and D. Williams. Thermal contraction of ultrahigh vacuum materials for scanning probe microscopy from 300 to 4 k. *Journal of Vacuum Science and Technology B*, 13:1063, 1995.

[102] W. Allers, A. Schwarz, U. D. Schwarz, and R. Wiesendanger. A scanning force microscope with atomic resolution in ultrahigh vacuum and at low temperatures. *Review of Scientific Instruments*, 69:221, 1998.

[103] P. Horowitz and W. Hill. *The art of electronics.* Cambridge University Press, 2nd edition, 1989.

[104] U. Tietze, C. Schenk, and E. Gamm. *Electonic Circuits.* Springer, 2nd edition, 2008.

[105] F. J. Giessibl and M. Tortonese. Self-oscillating mode for frequency modulation noncontact atomic force microscopy. *Applied Physics Letters*, 70:2529, 1997.

[106] D. Rugar, H. J. Mamin, R. Erlandsson, J. E. Stern, and B. D. Terris. Force microscope using a fiber-optic displacement sensor. *Review of Scientific Instruments*, 59:2337, 1988.

[107] D. Rugar, H. J. Mamin, and P. Guethner. Improved fiber-optic interferometer for atomic force microscopy. *Applied Physics Letters*, 55:2588, 1989.

[108] J. L. Yang, M. Despont, U. Drechsler, B. W. Hoogenboom, P. L. T. M. Frederix, S. Martin, A. Engel, P. Vettiger, and H. J. Hug. Miniaturized single-crystal silicon cantilevers for scannning force microscopy. *Applied Physics Letters*, 86:134101, 2005.

[109] A. Moser, H. J. Hug, T. Jung, U. D. Schwarz, and H-J. Guntherodt. A miniature fibre optic force microscope scan head. *Nature*, 4:769, 1993.

[110] B. W. Hoogenboom, P. L. T. M. Frederix, S. Martin, Y. Pellmont, M. Steinacher, S. Zäch, E. Langenbach, H. J. Heimbeck, A. Engel, and H. J. Hug. A fabry-perot interferometer for micrometer-sized cantilevers. *APL*, 86:074101, 2005.

[111] P. Bado, S. B. Wilson, and K. R. Wilson. Multiple modulation for optical pump-probe spectroscopy. *Review of Scientific Instruments*, 53:706, 1982.

[112] J. Baumann and G. Calzaferri. Development of picosecond time-resolved techniques by coninuous-wave laser amplitude modulation. *Journal of Photochemistry*, 23:387, 1983.

[113] R. Euler, U. Memmert, and U. Hartmann. Fiber interferometer-base variable temperature scanning force microscope. *Review of Scientific Instruments*, 68:1776, 1997.

[114] V. B. Braginsky, M. L. Gorodetsky, and S. P. Vyatchanin. Thermodynamical fluctuations and photo-thermal shot noise in gravitaional wave antennae. *Physics Letters A*, 264:1, 1999.

[115] H. J. Kimble, B. L. Lev, and J. Ye. Optical interferometers with reduced sensitivity to thermal noise. *Physical Review Letters*, 101:260602, 2008.

[116] V. B. Braginsky and A. B. Manukin. *Measurements of Weak Forces in Physics Experiments*. The University of Chicago Press, 1977.

[117] V. B. Braginsky, S. E. Strigin, and S. P. Vyatchanin. Parametric oscillatory instability in fabry-perot interferometer. *Physics Letters A*, 287:331, 2001.

[118] R. Hoffmann, M. A. Lantz, H. J. Hug, P. J. A. van Schendel, P. Kappenberger, S. Martin, A. Baratoff, and H. J. GÃ¼ntherodt. Atomic resolution imaging and frequency versus distance meas on nio(001) using low-temperature scanning force microscopy. *Physical Review B*, 67:085402, 2003.

[119] C. H. Metzger, M. Ludwig, C. Neuenhahn, A. Ortlieb, K. Favero, I. Karrai, and F. Marquardt. Self-induced oscillations in an optomechanical system driven by bolometric backaction. *Physical Review Letters*, 101:133903, 2008.

[120] S. Aphale, A. J. Fleming, and S. O. R. Moheimani. High speed nanoscale positioning using a piezoelectric tube actuator with active shunt control. *Micro & Nano Letters*, 2:9, 2007.

[121] S. W. Stahl, E. M. Puchner, and H. E. Gaub. Photothermal cantilever actuation for fast single-molecule force spectroscopy. *Review of Scientific Instruments*, 80:073702, 2009.

[122] L. Bartels, G. Meyer, and K. H. Rieder. Lateral manipulation of single cu atoms on flat and stepped copper surfaces. *Journal of Vacuum Science and Technology A*, 16:1047, 1998.

[123] J. W. M. Frenken. Diffusion in a surface: the atomic slide puzzle. *Applied Physics A*, 75:11, 2002.

[124] A. Norris. *Manipulating atoms using Scanning Probe Microscopy.* PhD thesis, Trinity College, University of Dublin, 2010.

[125] G. Binnig, H. Fuchs, C. Gerber, H. Rohrer, E. Stoll, and E. Tosatti. Energy-dependent state-density corrugation of a graphite surface as seen by scanning tunneling microscopy. *Europhysics Letters*, 1:31, 1986.

[126] J. V. Barth, H. Brune, G. Ertl, and R. J. Behm. Scanning tunneling microscopy observations on the reconstructed au(111) surface: Atomic structure, long-range superstructure, rotational domains, and surface defects. *Physical Review B*, 42:9307, 1990.

[127] L. Pauling. *Die Natur der chemischen Bindung.* Weinheim: Verlag Chemie, 1973.

[128] J. Viernow, J.-L. Lin, D. Y. Petrovykh, F. M. Leibsle, F. K. Men, and F. J. Himpsel. Regular step arrays on silicon. *APL*, 72:948, 1998.

[129] B. S. Swartzentruber, Y.-W. Mo, M. B. Webb, and M. G. Lagally. Scanning tunneling microscopy studies of structural disorder and steps on si surfaces. *Journal of Vacuum Science and Technology A*, 7:2901, 1989.

[130] J.-L. Lin, D. Y. Petrovykh, J. Viernow, F. K. Men, D. J. Seo, and F. J. Himpsel. Formation of regular step arrays on si(111)7x7. *Journal of Applied Physics*, 84:255, 1998.

[131] S. Yang and W. Huang. Three-dimensional displacements of a piezoelectric tube scanner. *Review of Scientific Instruments*, 69:226, 1998.

[132] G. W. Stupian and M. S. Leung. A scanning tunnling microscope based on a motorized micrometer. *Review of Scientific Instruments*, 60:181, 1989.

[133] P. K. Hansma and J. Tersoff. Scanning tunnling microscopy. *Journal of Applied Physics*, 61:R1, 1987.

[134] G. Binnig, H. Rohrer, Ch. Gerber, and E. Weibel. Surface studies by scanning tunneling microscopy. *Phys. Rev. Lett.*, 49(1):57–61, Jul 1982.

[135] J. A. Stroscio, R. M. Feenstra, and A. P. Fein. Local state densitiy and long-range screening of adsorbed oxygen atoms on the gaas(110) surface. *Physical Review Letters*, 58:1668, 1987.

[136] D. K. Biegelsen, F. A. Ponce, J. C. Tramontana, and S. M. Koch. Ion milled tips for scanning tunnling microscopy. *Applied Physics Letters*, 50:696, 1987.

[137] D. K. Biegelsen, F. A. Ponce, and J. C. Tramontana. Simple ion milling preparation of (111) tungsten tips. *Applied Physics Letters*, 54:1223, 1989.

[138] P. J. Bryant, H. S. Kim, Y. C. Zheng, and R. Yang. Technique for shaping scanning tunnling microscope tips. *Review of Scientific Instruments*, 58:1115, 1987.

[139] L. A. Nagahara, T. Thundat, and S. M. Lindsay. Preparation and characterization of stm tips for electrochemical studies. *Review of Scientific Instruments*, 69:3128, 1989.

[140] E. Stoll. Resolution of the scanning tunnel microscope. *Surface Science*, 143:L411, 1984.

[141] J. Tersoff and D. R. Hamann. Theory of the scanning tunneling microscope. *PRB*, 31:805, 1985.

[142] Y. Kuk and P. J. Silverman. Role of tip structure in scanning tunnling microscopy. *Applied Physics Letters*, 48:1597, 1986.

[143] Y. Kuk and P. J. Silverman. Sudy of metal surfaces by scanning tunneling microscopy with field ion microscopy. *Journal of Vacuum Science and Technology A*, 6:524, 1988.

[144] V. T. Binh and J. Marien. Characterization of microtips for scanning tunneling microscopy. *Surface Science*, 202:L539, 1988.

[145] J. P. Ibe, P. P. Bey, S. L. Brandow, R. A. Brizzolara, N. A Burnham, D. P. DiLella, K. P. Lee, C. R. K. Marrian, and R. J. Colton. On the electrochemical etching of tips for scanning tunnling microscopy. *Jounal of Vacuum Science and Technology A*, 8:3570, 1990.

[146] J. P. Song. A development in the preparation of sharp scanning tunnling microscopy tips. *Review of Scientific Instruments*, 64:900, 1993.

[147] H. Bourque and Leblanc R. M. Electrochemical fabrication of scanning tunnling microscopy tips without an electronic shut-off control. *Review of Scientific Instruments*, 66:2695, 1995.

[148] L. Anwei, H. Xiaotang, L. Wenhui, and J. Guijun. An improved control technique for the electrochemical fabrication of scanning tunnling microscopy microtips. *Review of Scientific Instruments*, 68:3811, 1997.

[149] Y. Nakamura, Y. Mera, and K. Maenda. A reproducible method to fabricate atomically sharp tips for scanning tunneling microscopy. *Review of Scientific Instruments*, 70:3373, 1999.

[150] O. L. Guise, J. W. Ahner, M. C. Jung, P. C. Goughnour, and J. T. Yates. Reproducible electrochemical etching of tungsten probe tips. *Nano Letters*, 2:191, 2002.

[151] R. Fasel and M. Parschau. *Fasel-Parschau STM tip sharpener.*

[152] T. Eguchi and Y. Hasegawa. High resolution atomic force microscopic imaging of the si(111)-7x7 surface: Contribution of short-range force to the images. *Physical Review Letters*, 89:266105, 2002.

[153] M. Tomitori and T. Arai. Tip cleaning and sharpening processes for non-contact atomic force microscopy in ultrahigh vacuum. *Applied Surface Science*, 140:432, 1999.

[154] J. B. Pethica. Comment on "interaction forces in scanning tunneling microscopy: Giant corrugations of the graphite surface". *Physical Review Letters*, 57:3235, 1987.

[155] A. Selloni, P. Carnevali, E. Tosatti, and C. D. Chen. Voltage-dependent scanning-tunneling microscopy of a crystal surface: Graphite. *Phys. Rev. B*, 31(4):2602–2605, Feb 1985.

[156] K. Takayanagi, Y. Tanishiro, S. Takahashi, and M. Takahashi. Structure analysis of si(111)7x7 resconstructed surface by transmission electron diffration. *Surface Science*, 164:367, 1985.

[157] S. Kawai and H. Kawakatsu. Atomically resolved dynamic force microscopy operating at 4.7mhz. *Applied Physics Letters*, 88:133103, 2006.

[158] D. D. Chambliss, R. J. Wilson, and S. Chiang. Ordered nucleation of ni and au islands on au(111) studied by scanning tunneling microscopy. *Journal of Vacuum Science and Technology B*, 9:933, 1991.

[159] W. D. Phillips, J. V. Prodan, and H. J. Metcalf. Neutral atomic beam cooling experiments at nbs. *Prog. Quant. Electr.*, 8:119, 1984.

[160] J. V. Prodan and W. D. Phillips. Chirping the light - fantastic? recent nbs atom cooling experiments. *Prog. Quant. Electr.*, 8:231, 1984.

[161] S. Chu, L. Hollberg, J. E. Bjorkholm, A. Cable, and A. Ashkin. Three-dimensional viscous confinement and cooling of atoms by resonance radiation pressure. *PRL*, 55(1):48, 1985.

[162] S. Chu, J. E. Bjorkholm, A. Ashkin, and A. Cable. Experimental observation of optically trapped atoms. *PRL*, 57(3):314, 1986.

[163] C. Cohen-Tannoudji. Laser cooling and trapping of neutral atoms: theory. *Physics Reports*, 219(3-6):153, 1992.

[164] L. S. Goldener, R. J. C. Spreeuw, C. Gerz, W. D. Phillips, M. W. Reynolds, S. L. Rolston, I. F. Silvera, and C. I. Westbrook. Demonstration of a microwave trap for cesium atoms. *Phys. B*, 194:893, 1994.

[165] W. D. Phillips. Quantum motion of atoms confined in an optical lattice. *Material Science and Engineering*, B48:13, 1997.

[166] A. Dorsel, J. D. McCullen, P. Meystre, E. Vignes, and H. Walther. Optical bistability and mirror confinement induced by radiation pressure. *PRL*, 51(17):1550, 1983.

[167] V. B. Braginsky, M. L. Gorodetsky, V. S. Ilchenko, and S. P. Vyatchanin. On the ultimate sensitivity in coordinate measurements. *Physics Letters A*, 179:244, 1993.

[168] V. B. Braginsky and S. P. Vyatchanin. Low quantum noise tranquilizer for fabry-perot interferometer. *Physics Letters A*, 293:228, 2001.

[169] V. B. Braginsky and A. A. Samoilenko. Measurements of the optical mirror coating properties. *Physics Letters A*, 315:175, 2003.

[170] T. Corbitt, D. Ottaway, E. Innerhofer, J. Pelc, and N. Mavalvala. Measurement of radiation-pressure-induced optomechanical dynamics in a suspended fabry-perot cavity. *Physical Review A*, 74:021802, 2006.

[171] B. S. Sheard, M. B. Gray, C. M. Mow-Lowry, and D. E. McClelland. Observation and characterization of an optical spring. *Physical Review A*, 69:051801, 2004.

[172] T. J. Kippenberger and K. J. Vahala. Cavity opto-mechanics. *Optics Express*, 15:17172, 2007.

[173] Y. Hadjar, P. F. Cohadon, C. G. Aminoff, M. Pinard, and A. Heidmann. High-sensitivity optical measurement of mechanical brownian motion. *Europhysics Letters*, 47:545, 1999.

[174] P. F. Cohadon, A. Heidmann, and M. Pinard. Cooling of a mirror by radiation pressure. *PRL*, 83:3174, 1999.

[175] T. R. Albrecht, P. GrÃ¼tter, D. Horne, and D. Rugar. Frequency modulation detection using high-q cantilevers for enhanced force microscope sensitivity. *JAP*, 69:668, 1991.

[176] J. Mertz, O. Marti, and J. Mlynek. Regulation of a microlever response by force feedback. *APL*, 62:2344, 1993.

[177] O. Arcizet, P. F. Cohadon, T. Briant, M. Pinard, A. Heidmann, J. M. Mackowski, C. Michel, O. FranÃ§ais, and L. Rousseau. High-sensitivity optical monitoring of a micromechanical resonator with a quantum-limited optomechanical sensor. *PRL*, 97:133601, 2006.

[178] A. Schliesser, P. Del'Haye, N. Nooshi, K. J. Vahala, and T. J. Kippenberger. Radiation pressure cooling of a micromechanical oscillator using dynamical backaction. *PRL*, 97:243905, 2006.

[179] D. Kleckner and D. Bouwmeester. Sub-kelvin optical cooling of a micromechanical resonator. *Nature*, 444:75, 2006.

[180] H. Rohde, J. Eschner, F. Schmidt-Kaler, and R. Blatt. Optical decay from a fabry-perot cavity faster than the decay time. *J. Opt. Soc. Am. B*, 19:1425, 2002.

[181] J. R. Barnes, R. J. Stephenson, C. N. Woodburn, S. J. O'Shea, M. E. Welland, T. Rayment, J. K. Gimzewski, and Ch. Gerber. A femtojoule calorimeter using micromechanical sensors. *RSI*, 65:3793, 1994.

[182] J. K. Gimzewski, Ch. Gerber, E. Meyer, and R. R. Schlittler. Observation of a chemical reaction using a micromechanical sensor. *Chem. Phys. Lett.*, 217:589, 1994.

[183] M. Vogel, C. Mooser, and K. Karrai. Optically tunable mechanics of microlevers. *APL*, 83:1337, 2003.

[184] M. Asheghi, Y. K. Leung, S. S. Wong, and K. E. Goodson. Phonon-boundary scattering in thin silicon layers. *Applied Physics Letters*, 71:1798, 1997.

[185] R. Hoffmann, A. Baratoff, H. J. Hug, H. R. Hidber, H. v. Löhneysen, and H. J. Güntherodt. Mechanical manifestation of rare atomic jumps in dynamic force microscopy. *Nanotechnology*, 18:395503, 2007.

[186] H. Hölscher, B. Gotsmann, W. Allers, U. D. Schwarz, H. Fuchs, and R. Wiesendanger. Measurement of conservative and dissipative tip-sample interaction forces with a dynamic force microscope using the frequency modulation technique. *Physical Review B*, 64:075402, 2001.

[187] C. Hoehberger Metzger and K. Karrai. Cavity cooling of a microlever. *Nature*, 432:1002, 2004.

[188] J. L. Garbini, K. J. Bruland, and W. M. Dougherty. Optimal control of force microscopy cantilevers. i. controller design. *JAP*, 80:1951, 1996.

[189] K. J. Bruland, J. L. Garbini, and W. M. Dougherty. Optimal control of ultrasoft cantilevers for force microscopy. *JAP*, 83:3972, 1998.

[190] M. Poggio, C. L. Degen, H. J. Mamin, and D. Rugar. Feedback cooling of a cantilever's fundamental mode below 5mk. *PRL*, 99:017201, 2007.

[191] A. Naik, O. Buu, M. D. LaHaye, A. D. Armour, A. A. Clerk, M. P. Blencowe, and K. C. Schwab. Cooling a nanomechanical resonator with quantum back-action. *Nature*, 443:193, 2006.

[192] K. J. Vahala. Optical microcavities. *Nature*, 424:839, 2003.

[193] A. J. Heinrich, J. A. Gupta, C. P. Lutz, and D. M. Eigler. Single-atom spin-flip spectroscopy. *Science*, 306:466, 2004.

Acknowledgements

Commonly, the span of a PhD is set by the financial resources, which is in average about 4 years. The expectancy of my PhD life has been stretched far beyond the norm. That gave me the grand opportunity to explore more uncharted territories than initially planned. The experience of my doctoral work is not only restricted to scientific findings but also offered me the chance to extend my social skills and mature in rhetoric. This was only possible because of the people I have come to know.

> ”What we are today is because of the people we met in the past.”

I believe there are no words that can truly reflect my gratitude to the people I have encountered, who contributed so profoundly to this work in one way or another. Here is my attempt to show my highest tribute to all of them.

- First of all, my greatest appreciation goes to my ”Doktorvater” *Hans Josef Hug* who inspired me in many and invaluable ways. I thank him for the brainstorming sessions, pragmatic approaches to challenging problems and discussions. From him I learned to tap into the source of critical, structured and scientific thinking.

- I would like to express my profound gratitude to the three post-docs who contributed their expertise to the LT-SPM project:
  \- *Raphaëlle Dianoux, Shigeki Kawai and Andrew Norris.*

  There is a German expression that says:

  > ”All good things come in three’s.”

  The outcome of your works has been summarized as cornerstones in this thesis. Thank you for your patience and insights that have enlightened my path through the tunnel.

- Special thanks go to *Sasa Vranjkovic* and everyone from the mechanical workshop. Your work and effort are an essential contribution to the success of this project.

- Heartfelt appreciations go to delightful *Beatrice Spörri* who offered her administrative and moral support in a cheerful way at any stage of my time at Empa.

- I am very grateful to *Alexis Baratoff* who provided his theoretical knowledged and thank him for his omniscient insights. His thoughtful comments always made me think out of the box and light things from different point of views.

- I wish to thank the colleagues from the University of Basel, who provided us with reliable assistance and steady guidance through uncountable technical obstacles:
  \- *Yves Pellmont, Timothy Ashworth, Sevil Özer, Niraj Joshi, Michael Steinacher.*

- Past and present fellow PhD students are an inexhaustible source of motivation, creativity and inspiration. Thank you for your morale support and sincere encouragement in many life's aspects:
  \- *Aude Pelisson, Christian Roth, Tobias Bauert, Dominik Jäger, Pablo Stickar, Chrysanthi Karageorgaki, Dandan Kong, Quirin Stoeckl, Nguyen Manh Thuong, Pham Minh Son, Claudia Müller.*

- I would like to thank my co-workers and friends at Empa, who enabled a relaxed working environment. Thank you for the enjoyable coffee break conversations and the many "Gipfeli" and cakes.

  \- *Manfred Parschau, Günther Hobi, Ulrich Müller, Roland Hauert, Jörg Partscheider, Beat Keller, Karl-Heinz Ernst, Rowena Crockett, Claudiu Falub, Lorenzo Castaldi, Magdalena Parlinska, Miguel Marioni, Sara Romer, Iñaki Maiztegui, Mirko Milas, Peggy Rossbach.*

- In my world there is no ranking for friends. There are no best friends, worst friends, part-time friends, reliable friends, coffee break friends, casual friends et cetera. A Japanese phrase says:

  > "No road is long with a friend on your side."

I wish to thank those who are still there, even when I have not seen them in ages. There is no order of importance:
\- *Marianna & Patrick Camina, Martina De Sergio & Peter Kappenberger, Jana & Herve Dietsch, Anatol Zingg, Dominik Thomann, Stefan Kuster, Pele & Muriel Muhika, Aimee McCreedy & James Shawn-Stewart, Stephanie Morlock & Victor Callegari, Hadjar Benmansour, Maria Marouli, Begõnia Vivas, Dimitris Kitou, Imran Rehman, Julie Warriner, Michael Benjamin, Lydia Nemirovsky, Kenzie Godfrey, Vilma Briones, Laetitia Bernard & Nicolas Pilet, Stéphanie Furer & Andrey Shkabko, Doris & Omar Steiger-Gassama.*

- Very special thanks go to so many people who paved the path leading to the person I am today. Here are a few of them. Thank you for being part of my life:
  \- *Oscar Meyer, Kuno Müller, Markus Meier, Judith Arnold & Walter Huber, Kurt & Evelyn Arnold, Leslie Arnold, Edwin Steiner, Dominique Woecke, Markus & Mirjam Von Weissenfluh-Bastian, Daniel Wieland, Anna-Grete Wieland & Paul Schmid.*

- Friendship is made, but family is given. My highest respect and deepest gratitude go to my parents, my siblings and their partners who were there when I needed them and were there when I did not need them:
  \- *Nguyen Thi Chua & Thai Ngoc Buu, Tongsiporn Amita & Thai Thanh Du, Thai Thanh Hien & Kälin Andreas.*

- *Nathalie Wieland*, you are the sunshine in the house. I thank you straight from my heart for your lovely being, your uplifting spirit and your love. Thank you for your wonderful aptitude to encounter each day as a new adventure.

Curriculum Vitae

Personalia

Family name: THAI
Middle name: Thanh
First name: Quang
Date of birth: 26th of December 1972
Place of birth: Rach Gia, Vietnam
Citizen of: Littau/ LU, Switzerland

Education

2005 - 2010: Experimental Physics, Doctor of Philosophy (PhD)
University of Basel, CH

2003 - 2004: Medical Physics, Master of Science (MSc)
University of Surrey, Guildford, UK

1998 - 2002: Physics, Bachelor of Art (BA)
Hunter College, City University of New York, USA

Professional Experience

2005 - 2011: PhD work, Empa
Laboratory for Nanoscale Materials Science, Dübendorf (ZH), CH

2002 - 2003: Network Administrator, ETH
Laboratory for Biomechanics, Zürich, CH

2000 - 2002: Optical Laboratory Technician
Hunter College, City University of New York, USA

1997 - 1998: Electronic Technician, R&D division
Swissray Medical AG, Hochdorf (LU), CH

1994 - 1996: Repair Technician, Gloor Electronics AG
Unterägeri (ZG), CH

Summer 1994: Medical Repair Technician
Swiss Military Recruitment School, Moudon (VD), CH

1990 - 1994: Apprenticeship as Radio/TV Technician
Audio Video Enz AG, Luzern (LU), CH

Communications

Talks

- **PhD Symposium 2008:** Empa St. Gallen, Switzerland
- **ICNT 2008:** Keystone Colorado, USA
- **SPS 2008:** Geneva, Switzerland (invited)
- **ICNT 2007:** Stockholm, Sweden
- **PhD Symposium 2006:** Empa St. Gallen, Switzerland

Posters

- **PhD Symposium 2007:** Empa Dübendorf, Switzerland
- **NC-AFM 2007:** Antalya, Turkey
- **SPS 2007:** Zürich, Switzerland
- **ICNT 2006:** Basel, Switzerland
- **PhD Symposium 2005:** Empa Dübendorf, Switzerland